Centre Eau Terre Environnement

Hybrid Flow Modelling of Culvert Spoiler Baffles Designed to Create Shelters During Upstream Fish Passage

Par

Sophie Larrivée-Larouche

Mémoire présenté pour l'obtention du grade de

Maître ès Sciences (M.Sc.)

en sciences de l'eau

Jury d'évaluation

Président du jury et examinateur interne	Jacob Stolle, ph. D. Institut national de la recherche scientifique
Examinateur externe	Pascale Biron, ph. D. Géographie, aménagement et environnement Université Concordia
Directeur de recherche	Normand E. Bergeron, ph. D. Institut national de la recherche scientifique

ACKNOWLEDGMENTS

Un grand merci à mon directeur de thèse, Normand Bergeron, pour son soutien et sa confiance tout au long de cette recherche. Je tiens également à remercier Alexandre Pirolley, dont les idées et les discussions ont été précieuses pour mener à bien ce travail. Enfin, une reconnaissance spéciale à Jean-Guillaume Dion dont le soutien inconditionnel est ce qui m'a initialement permis d'entreprendre ce projet.

Ce mémoire est une contribution au Projet Miranor (2018-2023) financé par le Fonds pour dommage à l'environnement du Ministère Environnement et Changement Climatique Canada.

RÉSUMÉ

Un déclin des populations de poissons a été observé ces dernières années, en partie dû à la présence de barrières hydrauliques le long des voies migratoires - tels que des barrages, des ponceaux et des ponts de route - qui fragmentent l'habitat disponible. Cette recherche utilise la dynamique des fluides computationnelle (CFD) afin de soutenir la conception de saillies profilées. Ces saillies, installées dans des ponceaux, génèrent des zones de vitesse réduite (RVZ) et permettent aux poissons de se reposer lors de leurs tentatives de franchissement des barrières hydrauliques, tout en minimisant les pertes de charge dans l'infrastructure. Plus précisément, le modèle de Smagorinsky a été utilisé pour modéliser les champs de vitesses 3D autour de saillies de différentes formes et tailles, et ce pour deux conditions hydrauliques. Les modélisations ont été validées à l'aide de vitesses mesurées avec un vélocimètre acoustique à effet Doppler et de vidéos de la forme et taille des RVZ générées par les saillies. Les résultats indiquent que les conditions hydrauliques impactent la largeur de la RVZ, mais pas sa hauteur ni sa longueur. La condition la plus turbulente est généralement associée à une RVZ plus large pour une même hauteur de saillie. Cette augmentation de la largeur pourrait potentiellement être causée par l'utilisation d'une grille computationnelle légèrement plus grossière pour cette seconde condition hydraulique. La hauteur de la RVZ est directement liée à la hauteur de la saillie, et la longueur de la RVZ est prédite à la fois par le niveau de submersion des saillies et par le rapport de la largeur de la saillie sur sa hauteur. Le modèle de Smagorinsky fournit des résultats conservateurs : les vitesses dans la RVZ tendent à être légèrement sous-estimées, alors qu'elles sont surestimées dans la couche de cisaillement et dans la région de libre circulation. Comparé à une modélisation 1D ou 2D, le modèle Smagorinsky permet une reproduction apparemment réaliste des tourbillons générés en aval des saillies, bien qu'à un coût en temps de calculs élevé. Les résultats confirment la pertinence d'utiliser le modèle Smagorinsky pour soutenir la conception de systèmes visant à faciliter le passage des poissons vers l'amont d'une structure hydraulique.

Mots-clés : Modélisation hybride ; migration et déplacement ; poisson ; sillage ; dynamique des fluides computationnelle ; Smagorinsky

ABSTRACT

A significant decline in fish populations has been observed in recent years, partly attributable to the presence of hydraulic barriers along migration paths – such as dams, culverts and road bridges – which fragment the habitat available to fish. This research uses computational fluid dynamics (CFD) to support the design of streamlined spoiler baffles. These spoiler baffles, installed in culverts, generate reduced velocity zones (RVZ) which allow fish to rest during their attempts to cross hydraulic barriers, while minimizing head loss within the infrastructure. More precisely, the Smagorinsky model was used to model the 3D velocity fields around spoiler baffles of different shapes and sizes, under two hydraulic conditions. The models were validated using velocities measured with a velocimeter and videos of the shape and size of the RVZs generated by the spoiler baffles. The results indicate that hydraulic conditions have an impact on the width of the RVZ, but not on its height or length. The most turbulent condition was generally associated with a larger RVZ for spoiler baffles of a given height, which might be attributable to the use of a slightly coarser computational mesh for this hydraulic condition. The height of the RVZ was directly linked to the height of the spoiler baffle, and the length of the RVZ is predicted by both the submersion level of the spoiler baffle and the ratio of the width of the spoiler baffle to its height. The Smagorinsky model provides conservative results; Velocities within the RVZ tend to be slightly underestimated, while they are overestimated in the shear layer and in the free-flow region. Compared to 1D or 2D modeling, the Smagorinsky model allows an apparently realistic reproduction of the vortices generated downstream of the spoiler baffles, although at a high computational cost. The results confirm the relevance of using the Smagorinsky model to support the design of systems aimed at facilitating the passage of fish upstream hydraulic structures.

Keywords : Hybrid modelling; Fish Migration; Wake; Computational Fluid Dynamic; Smagorinsky

SOMMAIRE RÉCAPITULATIF

Un déclin des populations de poissons de divers espèces a été observé ces dernières années, en partie dû à la présence de barrières hydrauliques le long des rivières, poussant une partie de la recherche vers la conception de systèmes visant à faciliter le passage des poissons à travers ces barrières. Cependant, la conception de ces systèmes est coûteuse et des problèmes peuvent survenir en raison des limites technologiques et physiques rencontrés, et des lacunes dans les données découlant de ces limites.

L'objectif principal de ce projet de recherche est de soutenir la conception de saillies par l'utilisation de la dynamique des fluides computationnelle (CFD). Ces saillies visent la création d'abris hydrauliques pour les poissons lors de leur passage vers l'amont de ponceaux en leur fournissant des zones de vitesses réduites (RVZ) pour se reposer. La CFD est utilisée pour modéliser les RVZ générées en aval des saillies, et ainsi diversifier l'éventail des données disponibles pour la conception de ces saillies à un moindre coût. Les objectifs spécifiques de cette recherche sont :

1. D'identifier la meilleure approche de modélisation CFD pour reproduire la séparation du courant autour des saillies, ainsi que les structures de turbulence générées ;
2. De valider cette approche par l'utilisation des mesures de vitesses d'écoulement 3D enregistrées autour des saillies de différentes formes et tailles lors d'une expérimentation physique en laboratoire ; et
3. D'analyser les impacts des caractéristiques physiques des saillies et d'un changement aux conditions hydrauliques sur les RVZ, ainsi que sur les structures turbulentes générées en aval des saillies.

Les travaux s'appuient sur les hypothèses suivantes :

i. Le modèle de Smagorinsky peut modéliser avec précision les schémas de turbulence complexes associés à la séparation de l''écoulement résultant d'un objet s'opposant au courant.
ii. Les caractéristiques des RVZ varieront selon :
    - La forme des saillies ;
    - Le niveau de submersion des saillies ; et
    - Les conditions hydrauliques environnantes.

Dans le cadre de l'expérimentation physique, 18 saillies de formes et tailles différentes ont été testées sous deux conditions hydrauliques dont les vitesses moyennes de courant étaient de 0,27 m/s et 0,36 m/s respectivement. Les saillies ont été positionnées au centre d'un canal de 0,31 mètres de largeur, 0,30 mètres de hauteur et 6,3 mètres de longueur. Les données disponibles pour la validation des modèles CFD incluent : (1) les vitesses aux alentours des saillies et dans leur sillage, captées à l'aide d'un vélocimètre acoustique à effet Doppler ; (2) les hauteurs d'eau dans le canal, mesurées manuellement à tous les 68 centimètres ; et (3) des vidéos des tourbillons dans le sillage de l'objet capturée par une injection de colorant dans la RVZ.

Les travaux de modélisation CFD ont été effectués dans le logiciel libre OpenFOAM. Le modèle Smagorinsky, couplé de la fonction d'amortissement de Van Driest, a été utilisé pour reproduire les conditions testées en laboratoire. Le modèle Smagorinsky est un modèle de simulations des grandes structures turbulentes (« Large Eddy Simulation » en anglais). Il a été possible de confirmer que ce modèle est simple d'utilisation et qu'il permet une bonne reproduction des tourbillons générés lors de la séparation d'un courant menant à l'apparition de pressions négatives en aval d'un objet. L'algorithme *PimpleFoam*, sous sa forme *piso*, un solveur monophasé, a été utilisé pour résoudre les systèmes d'équations du modèle.

Les résultats obtenus sont conformes à la littérature. Ils montrent que le modèle Smagorinsky tend à sous-estimer les vitesses dans le sillage de la saillie, et ce malgré l'utilisation de la fonction d'amortissement de Van Driest. Une surestimation générale des vitesses en dehors de la RVZ a également été observée. Considérant que le modèle serait utilisé pour la conception de systèmes visant à faciliter le mouvement et la migration des poissons au travers de barrières hydrauliques, la pertinence d'utiliser le modèle Smagorinsky est confirmée. En effet, dans un tel contexte, la surestimation des vitesses d'écoulement libre et la sous-estimation des vitesses dans la RVZ constituent des résultats conservateurs. Si les vitesses modélisées sont sous le seuil supporté par les poissons, alors les poissons devraient pouvoir transiter dans le système réel.

L'analyse des données des simulations montre que les conditions hydrauliques environnantes n'exercent un effet significatif que sur le rapport entre la largeur de la RVZ et la largeur de la saillie. En effet, la condition hydraulique la plus turbulente est associée à une RVZ plus large pour une même saillie. Cette augmentation de la largeur en fonction de la turbulence pourrait également être due à l'utilisation d'un maillage légèrement plus grossier pour la deuxième condition hydraulique. Dans tous les cas, la forme générale de la RVZ est un miroir de la forme de la saillie et les caractéristiques des RVZ varient en fonction de la forme des saillies et de leur

niveau de submersion. Le rapport de la largeur de la saillie sur sa hauteur (SB.W/SB.H) et son niveau de submersion (W.D/SB.H) se sont révélés être de bons prédicteurs de la longueur de la RVZ créée par une saillie précise, suivant le modèle subséquent, dans lequel RVZ.L/SB.H est le ratio de la longueur de la RVZ sur la hauteur de la saillie :

$$\frac{RVZ.L}{SB.H} = 0.6574\frac{SB.W}{SB.H} + 0.1410\frac{W.D}{SB.H} + 0.4596 \qquad \begin{bmatrix} \frac{SB.W}{SB.H} \in [0.5, 2.0] \\ \frac{W.D}{SB.H} \in [3.7, 7.6] \end{bmatrix}$$

Valider la longueur de la RVZ modélisée s'est avéré difficile. La RVZ modélisée semble être plus longue que la RVZ physique générée par les saillies lors des expérimentations en laboratoire. Une limite substantielle aux travaux actuels réside dans l'impossibilité de mesurer précisément la longueur de la RVZ physique. Il est recommandé qu'une règle soit installée sous le canal lors d'expérimentations physiques futures pour mesurer la longueur approximative des RVZ physiques et ainsi offrir plus de données pour la validation des modèles CFD.

Une autre limite se situe dans la lourdeur des résultats de chaque simulation. La taille d'un sillage primaire est fortement dépendante du temps. Par conséquent, la longueur de la RVZ devrait être calculée comme une longueur moyenne sur des résultats enregistrés à un pas de temps suffisamment petit pour visualiser les oscillations du sillage primaire. L'enregistrement des résultats CFD nécessite cependant une quantité extrême de mémoire d'ordinateur et étant donné la grande quantité de scénarios modélisés dans le cadre des présents travaux, il n'a pas été possible d'analyser l'évolution de la RVZ dans le temps.

Dans un contexte d'utilisation des RVZ par les poissons, les saillies modélisées ont conduit à des longueurs de RVZ jugées comparables. C'est-à-dire qu'il existe un chevauchement important dans la longueur du corps des poissons qui pourraient potentiellement utiliser les saillies comme abris sans être confus (longueur ~ 3 à 4,5 centimètres). Une saillie beaucoup plus petite serait nécessaire pour permettre le passage de poissons d'une longueur inférieure à 3 centimètres sans créer de confusion.

Outre la longueur de la RVZ, les principales caractéristiques à considérer pour la conception finale concernent plutôt la stabilité de la RVZ générée, à savoir son niveau de fragmentation et le type d'arrangement des tourbillons observés. Ces caractéristiques auront vraisemblablement un impact significatif sur les poissons et sur leur capacité à utiliser la RVZ générée. Trois types d'arrangements des tourbillons ont été observés, soit :

Type A. (6%) Une petite chaîne de tourbillons est identifiée le long de la paroi aval de la saillie, sur toute son aire. Cette chaîne évolue en tourbillons-anneaux toroïdaux observés dans la partie inférieure de la RVZ. Dans un des cas, les tourbillons-anneaux semblent être constitués d'une paire d'anneaux mères et filles; l'anneau-mère forme l'anneau-fille qui est rejetée périodiquement en aval de la saillie. Dans d'autres cas, un ou deux anneaux sont observés qui donnent lieu à une chaîne de tourbillons transitant le long du volume de la RVZ et évoluant de manière aléatoire sur tous les plans. La RVZ est fermée par des tourbillons hélicoïdaux, généralement deux, mais parfois plus.

Type B. (33%) Une petite chaîne de tourbillons est identifiée le long de la face aval de la saillie. Au lieu de tourbillons-anneaux toroïdaux, la RVZ est dominée par des tourbillons en forme d'arc. Dans un des cas (H20W30 sous la condition hydraulique #2), deux tourbillons-arc contrarotatifs sont reliés et forment un seul grand tourbillon-arc, indiquant une certaine stabilité. La RVZ est fermée par des tourbillons hélicoïdaux.

Type C. (61%) Cet arrangement montre une RVZ plutôt désorganisée, sans anneaux toroïdaux, ni tourbillons-arc. Une chaîne de tourbillons évoluant aléatoirement sur tous les plans est observée, depuis la face aval de la saillie jusqu'à l'extrémité de la RVZ, qui est fermée par des tourbillons hélicoïdaux. La caractéristique principale de ce type est la présence d'un vortex principal, apparemment stable et tournant dans le plan YZ.

Malgré son apparence désorganisée, la présence d'un vortex principal, apparemment stable et tournant dans le plan YZ, indique que le type C pourrait en fait être le plus stable de tous les arrangements observés et le plus facilement utilisable par les poissons. Dans le cadre des présents travaux, il est cependant impossible de lier le comportement des poissons aux tourbillons modélisés.

Cette maîtrise a été utile pour définir le niveau de précision du modèle Smagorinsky et certaines mises en garde lors de son utilisation pour la conception de système de saillies profilées visant à supporter les poissons dans leurs franchissements de barrières hydrauliques. Une prochaine étape pertinente serait de modéliser le système de deux saillies qui a été physiquement testé en laboratoire avec des poissons pour mieux comprendre si et comment les tourbillons dans la RVZ impactent le comportement des poissons autour des saillies, et même si les données modélisées correspondent aux comportements observés chez les poissons. Cet effort supplémentaire éclairerait une hypothèse soulevée lors des présents travaux, soit que la

génération de trains de vortex de Kármán de tailles variées serait préférable à la création de RVZ stables avec un sillage secondaire chaotique.

La principale lacune du modèle de Smagorinsky est son coût de calcul élevé. Un maillage très fin est nécessaire pour assurer la convergence du modèle, à savoir le maintien d'une valeur *y*+ de 10 selon la littérature consultée. Ce coût de calcul élevé est ce qui a conduit à l'utilisation du solveur *PimpleFoam* qui, par sa nature monophasée, ne permet pas de modéliser la surface libre du système, mais permet de réduire considérablement le temps de simulation par rapport au solveur biphasé *InterFoam*. Cette décision entraîne une certaine perte d'informations, car les tourbillons créés par l'interface air-eau ne sont pas modélisés. Il est également possible que cette décision contribue à la surestimation des vitesses d'écoulement libre et à la sous-estimation des vitesses dans le sillage de l'objet. De façon générale, les données indiquent que l'utilisation de *PimpleFoam* permet une reproduction de la forme de la RVZ et de la turbulence générée dans la région inférieure du canal et dans le sillage de la saillie où transitent les poissons. L'utilisation d'un modèle simplifié monophasé s'est donc révélée appropriée pour un système dominé par des tourbillons générés par la présence d'un objet opposant le courant.

Étant donné l'importance des temps de calculs liés à l'utilisation d'un modèle de type LES, une piste de solution à évaluer serait de modéliser à nouveau l'une des 18 saillies déjà modélisées en utilisant un modèle hybride RANS-LES, tel que le modèle de simulation de tourbillons détachée retardée améliorée (« Improved Delayed Detached Eddy Simulation » en anglais). Dans le cas où ce modèle hybride fournirait des résultats similaires à ceux du modèle de Smagorinsky, il pourrait s'avérer utile pour diminuer considérablement le coût des calcul, améliorant la pertinence de l'utilisation de la modélisation CFD pour soutenir l'effort de conception des saillies.

Ce mémoire de maîtrise est, à notre connaissance, le premier à analyser de façon aussi détaillée la pertinence d'utiliser le modèle de Smagorinsky dans un contexte de soutien à la conception de systèmes visant un support aux franchissements des barrières hydrauliques par les poissons. Bien qu'il reste encore beaucoup à faire pour confirmer davantage la pertinence de ce modèle, ce mémoire présente des informations utiles sur l'avenir de la modélisation hybride.

TABLE OF CONTENTS

LIST OF FIGURES

LIST OF TABLES

LIST OF EQUATIONS

LIST OF ABBREVIATIONS

ADV	Accoustic doppler velocimeter
CFD	Computational fluid dynamics
DES	Detached eddy simulations
DNS	Direct numerical simulations
IDDES	Improved Delayed Detached Eddy Simulations
LES	Large eddy simulation
OpenFOAM	Open-Source Field Operation and Manipulation
RANS	Reynold-averaged Navier-Stokes equations
RVZ	Reduced velocity zone
SGS	Subgrid-scale
URANS	Unsteady Reynold-average Navier-Stokes equations

1 INTRODUCTION

1.1 Context

Fish are a key part of the aquatic food web and while emphasis tends to be put on particular fish species relevant to human-economics and uses, specifically marine fishes, inland and migratory fish are equally important in preserving nutrient flux within ecological systems and conserving native biological diversity, as well as being a food source for billions of people worldwide (Lynch et al., 2016). A significant decline of migratory freshwater fish populations has been observed in recent years with anthropogenic disturbances identified as a primary vector of this deterioration (Scott-Gatty et al., 2020). Schlosser (1991) also contended that the focus of researches is too often limited to small spatial and short temporal scales, thus not capturing the problems faced by managers, which extend to larger spatial and longer temporal scales.

Fish movements within a system of rivers and streams play a significant role in the regulation of fish populations, as they are necessary to ensure various key elements and processes, such as habitat complementation and supplementation; colonization and recolonization; habitat connectivity; access to refugia; and migration (Fausch et al., 2002). Radinger and Wolter (2014) quantified the components of fish dispersal within freshwater fish communities and found that the median movement distance of the stationary component, linked to the concept of home range, was 36.4 meters; the mobile component, which is hypothesized as being responsible for the individuals exchange between populations, was calculated at 361.7 meters. The creation of anthropogenic barriers (physical, hydraulic, chemical, thermal) hinders the movements of fish across their habitats (Silva et al., 2017), fragmenting them, which leads to—among other effects—reduced population sizes and increased genetic drift (Torterotot et al., 2014).

Dams are often the first structure to come to mind when thinking about fish barriers, as they are responsible for significant fish habitat losses worldwide and pose a real threat to many freshwater fish species (Liermann et al., 2012). However, bridges and culverts are also challenging for fish migration and much more abundant. The sudden decrease in river width caused by these structures increases flow velocity and turbulence, often creating a hydraulic barrier for fish passage (Watson et al., 2018). The slope of the culverts itself can strongly impact fish migration, not only because of the increased velocity, but also because of the additional contribution of gravity force in dissipating the power of fish thrust (Wang and Chanson, 2018).

The bridges and culverts design guidelines of the “Ministère des Ressources naturelles” remind designers that preserving fish habitat continuum must be considered a priority (Cloutier et al., 1997); it provides design constraints which aim to ensure fish passage through newly built or modified water conveyance structures. As a result, many believe that fish passage is a solved problem, an established knowledge. However, an inventory of 126 culverts distributed on four major salmon rivers across the province of Quebec showed that only 35% of culverts were passable (Gagnon-Poiré, 2017). In southern Labrador, a similar study completed along the newly constructed Trans Labrador Highway showed that 53% of the 47 culverts and 4 bridges surveyed impeded fish passage; a finding attributed to poor design or poor installation of the infrastructure and likely resulting from an inadequate environmental oversight in the field (Gibson et al., 2011).

Models, such as FishXing, have been developed to support engineers and fish specialists in verifying that fish passage is successful when designing culverts by modeling organism capabilities against culvert hydraulics across a range of stream discharges (U.S. Department of Agriculture, 2006). Mahlum et al. (2014) showed that common barrier assessment models tend to be conservative, while Castro-Santos (2006) warns of their inaccuracy due to the inclusion of unrealistic assumptions, such as fish swimming voluntarily to physiological fatigue, a behavior rarely observed in the wild. The standardization of fish passage evaluation is, at present, lacking, and systems aiming to facilitate fish passage based on fish swimming speeds and mean water velocity alone are often inadequate (Silva et al., 2017).

Accurately predicting the movement of fish through culverts is a challenge because - amongst other limitations - of an incomplete knowledge of fish physiology and behaviour, as well as an incapacity to thoroughly reproduce hydraulic conditions found in nature within a laboratory setting that uses steady flow conditions (Castro-Santos, 2005, Liao, 2007, Mahlum et al., 2014). Castro-Santos (2006) proposed an improved empirical model, based on survivorship, which predicts the proportion of the population that successfully reaches a given distance, while considering the variability of swimming capabilities within a population of fish. This model improves the prediction of fish capacity to traverse hydraulic barriers, but places more burden on managers, as it requires explicit assumptions about the speed at which a fish can actually swim, a variable often unknown by designers (Castro-Santos, 2006). Wang and Chanson (2018) also pointed at the importance of quantifying the power and energy expended by a moving fish to accurately predict the success of fish passage, and to improve current knowledge on fish-turbulence interplay.

Generally, fish have been observed to prefer a path of least resistance when migrating upstream currents (Keefer et al., 2011, McElroy et al., 2012, Lindberg et al., 2016, Wang and Chanson, 2018), a behavior also observed during physical experimentations within culverts (Richmond et al., 2007, Constantin, 2017, Goerig et al., 2017). Goerig et al. (2017) found that fish passage success was higher in corrugated culverts than smooth culverts; small fish were observed to use the corrugations for sheltering from high flow velocities. Richmond et al. (2007) further noted that spiral corrugations induce secondary flows which cause asymmetries in both the velocity and turbulence distributions, leading to the appearance of reduced velocity zones (RVZ) along the wall that fish use to facilitate their upstream passage.

Various research projects have therefore attempted to facilitate fish passage within culverts by recommending various designs to reduce flow velocity and provide shelter for fish. However, the disconnect between fish specialists and designers too often results in those designed systems seldom being used in the field on account of the recommendations leading to impractical and hydraulically inefficient culvert structures, which have been observed to lose up to 50% of their discharge capacity (Duguay and Lacey, 2015, Leng and Chanson, 2020). In Nova Scotia, Fisheries and Oceans Canada (2015) published guidelines for the design of fish passage within culverts, seemingly transforming the culverts into fishways by recommending the installation of perpendicular notched baffles, which leads to major head loss and oversized culverts design. More recently, Cabonce et al. (2017) were able to reduce the head loss significantly by using flat triangular corner baffles; they observed a maximum increase in the water depth of 26% for the larger baffles, and of approximately 8% for the smaller baffles. However, the use of flat baffles generally result in debris clogging and increased culvert maintenance costs (Watson et al., 2018), as well as seemingly confusing smaller fish during their ascent (Cabonce et al., 2018).

1.2 Problem Statement

When designing systems which aim to facilitate fish passage through culverts, issues can arise from technological limitations and resulting data gaps. Fishes respond to complex hydraulic characteristics in a variety of manners, and systems designed for a specific fish specie might not work as well for another (Keefer et al., 2011). Physical experiments are costly and thus, it is impractical to evaluate the impacts of a designed system on flow resistance and fish passage over numerous hydraulic conditions and using various species of fish. This makes it difficult to thoroughly understand how and why fish would use the designed system, and to predict how the system will influence the overall discharge capacity of the culvert.

Recently, Computational Fluid Dynamics (CFD) modeling has shown promises in more accurately defining turbulence and rest zones available to fish within conveyance structures. It has been used as a complement to physical modelling (Leng and Chanson, 2020) to help (1) reduce operational costs by identifying potential issues and scenarios worth modeling physically; and (2) fill the data gap generated by technological constraints and limitations. It could therefore prove a useful tool in designing fish friendly systems aiming to facilitate fish passage through culverts without impeding flow.

CFD allows resolution of the Navier-Stokes equations, which mathematically express both the conservation of momentum and of mass in Newtonian fluids, while also accounting for fluid viscosity, making them a useful tool in modeling incompressible fluid flow. While the nonlinearity of these equations makes them difficult to solve, it enables the modeling of turbulence. In CFD, solving of the Navier-Stokes equations in 3D can be achieved one of three ways, specifically via the use of (1) Direct Numerical Simulation (DNS); (2) Reynolds-Averaged Navier-Stokes equations (RANS); or (3) Large Eddy simulation (LES). DNS require an enormous amount of computing power, rendering them inconvenient for complex geometries and larger systems; RANS and LES are more viable options, as they make use of turbulence closure models allowing for coarser computational grids resulting in a significant decrease in the required computational power (Fröhlich and Rodi, 2002).

As isotropic models, RANS have been shown to be inefficient when studying turbulent phenomena around obstacles; RANS completely neglect history effects, only allowing for the modelling of mean-velocity and pressures fields, averaging turbulent structures and underpredicting vortex shedding (Alfonsi, 2009). Unsteady RANS (URANS), while allowing the modelling of the oscillation of velocities in the wake region and the estimation of the turbulent kinetic energy, do not allow proper modelling of horseshoe vortices and are consistently less accurate than LES for the modelling of turbulent structures (Ducrocq et al., 2017). To enable the analysis of the turbulent structures generated by an object, LES models, which are computationally expensive, are selected.

Open-Source Field Operation and Manipulation (OpenFOAM) C++ libraries is a framework used to develop application executables that has been shown to provide as accurate results as proprietary software such as FLOW-3D (Duguay et al., 2017). OpenFOAM offers over 250 pre-built applications, including solvers and utilities which enable solving of complex fluid dynamics problems (OpenFOAM Foundation, 2020). Ten LES turbulence closure models are available for turbulence modeling in incompressible fluids. The Smagorinsky model used on a fine mesh has

been shown to provide accurate and realistic results when modeling flow turbulence (Chorda et al., 2019)). However, validation of the CFD model remains essential, as there is no guarantee that a model that worked for a specific scenario will perform as well under different conditions (Leng and Chanson, 2020). It is crucial that the turbulence closure model be properly calibrated using observations from physical experimentation.

1.3 Research Objectives

Building on past experiments, researchers at the *Institut national de la recherche scientifique* are currently working on developing a new system to improve the success of fish passage within culverts, particularly smooth culverts. It is hypothesized that the use of profiled spoiler baffles of relatively small sizes, as opposed to flat baffles, would create RVZs for fish to rest while offering little resistance to flow. Because the size, shape and spatial concentration of these spoiler baffles should be optimized according to the physiological characteristics of the target fish, it is important to first define what the characteristics of the RVZs generated by the spoiler baffles are. However, making measurements in an experimental channel to obtain this information would be long and costly. The main objective of this master's thesis is therefore to assist in the design of a profiled spoiler baffle by using CFD modelling. The specific objectives are:

1. To identify the best CFD approach to model the flow around a spoiler baffle;
2. To validate this CFD approach by using 3D flow velocities measured using an ADV velocimeter around spoiler baffles of various sizes and shapes as part of an experimental channel experiment;
3. To analyse the impacts of the physical characteristics of the spoiler baffle and of the hydraulic conditions on the average and turbulent structures generated by the presence of the spoiler baffle.

The current work is based on the following hypothesis:

i. The Smagorinsky model can accurately model complex turbulence patterns associated to the flow separation resulting from an object opposing the current.
ii. The characteristics of the RVZ will vary following:
    a. The shape and size of the spoiler baffles;
    b. The level of submergence of the spoiler baffles; and
    c. The level of turbulence, indicated by the Reynolds number.

2 LITERATURE REVIEW

2.1 What is Turbulence?

Turbulence refers to the chaotic changes in flow velocity and pressure observed within a moving fluid, leading to the creation of unsteady vortices, or eddies, of various dimensions (Childress, 2009). Eddies and vortices are similar, as they both describe the swirling motion of a fluid, but vortices are generally considered having a more stable nature. The often apparently random nature of turbulence has made it difficult to comprehend and while the developed models are useful, they do not always represent the complexities of nature (Fan and Tsuchiya, 1990).

Cotel and Webb (2015) classify the formation of turbulent structures within water in two general categories: (1) wave-dominated, in which deformations at the air-water interface create vertical velocities; and (2) eddy-dominated, in which eddies are created at shear zones within submerged areas. The turbulence generated by the presence of an obstacle opposing the current is part of this second category.

Most proposed designs to facilitate fish passage through culverts make use of obstacles opposing the current, leading to the generation of a wake i.e., a region of flow disturbances downstream of an obstacle. The wake has been historically divided into two main regions (Fan and Tsuchiya, 1990) :

(1) the near-wake, or primary wake;

(2) the far-wake, or secondary wake.

Both regions are outlined in Figure 2.1.

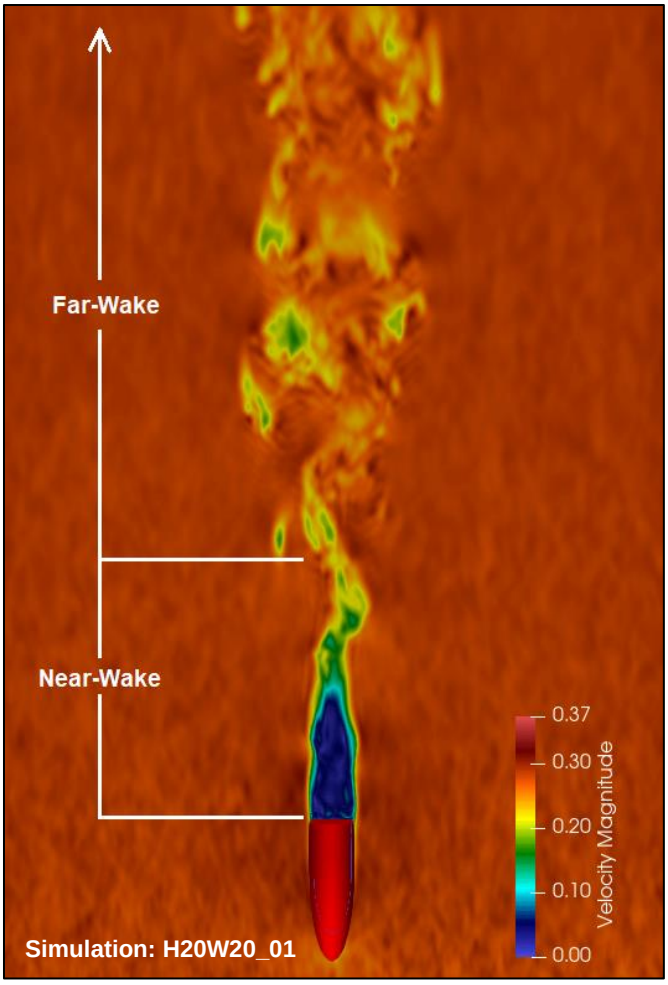

Figure 2.1 : Identification of the near-wake and far-wake regions

2.1.1 The Near-Wake

The near-wake, also called recirculation region, or formation region when there is evidence of vortex shedding, is located closest to the obstacle. It is characterized by high vorticity and associated with vortex formation and growth. Its size and flow patterns depend strongly on the shape of the body that creates it, the level of submergence and the surrounding hydraulic conditions, such as the Froude and Reynold numbers (Mignot and Riviere, 2010).

The recirculation wake region constitutes a RVZ for fish; it is characterized by a sudden decrease in flow velocity with higher turbulence (Sadeque et al., 2009). However, its shape and the complexities of the flow patterns within it vary significantly depending on the surrounding hydraulic conditions. Fan and Tsuchiya (1990) classified various wake configurations based on their level of turbulence; from a steady, laminar wake with a closed, well-defined and stable recirculation region to an unsteady, turbulent wake with an open and more chaotic formation region. In all cases, a vortical motion should exist.

Fan and Tsuchiya (1990) also states that experiences have shown that the near-wake could be further divided into two main regions, namely (1) a confined turbulent wake region, with a somewhat more stable nature and which boundary is marked by a cut-off stream crossing the central axis of the near-wake from one side of the free shear layer to the other; and (2) a shedding vortical wake region, responsible for the shedding of the vortices, with a size that varies over time, often following a sawtooth function (Figure 2.2).

Various studies have been conducted to better understand what factors impact the nature of flow within the RVZs. Darghani (1989) showed that the level of turbulence of the fluid impacted the number of vortices created within the recirculation wake region, with the number of vortices increasing with higher Reynold numbers. The shape and size of the obstacle also play a significant role in characterizing the near-wake region, its size and complexities of the flow patterns found within it (Darghani, 1989, Shamloo et al., 2001). Finally, the relative submergence of the obstacle was also found to impact the RVZ, with its size decreasing with water depth (Mirauda et al., 2007) until a critical point where it does not form (Sadeque et al., 2009).

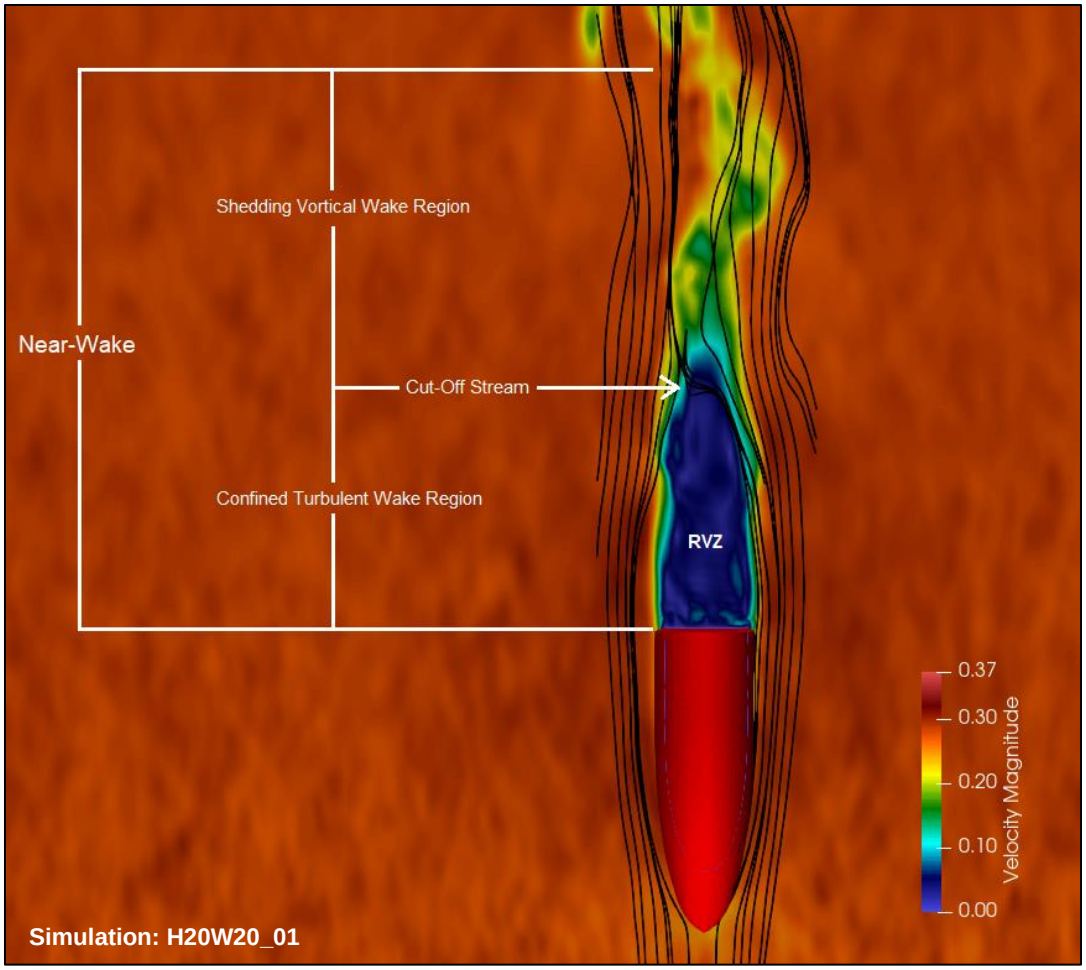

Figure 2.2 : Identification of the shedding vortical wake region and confined turbulent wake regions. Limits are established by cut-off stream lines (black). Velocities are in meters per second.

2.1.2 The Far-Wake

The far-wake includes the rest of the obstacle wake. It can be further divided into two regions : (1) the characteristics decay region depend on the geometry of the obstacle and it is where mixing effects cause turbulent diffusion; and (2) the asymptomatic decay region is where the flow tends to return to its undisturbed state, while still containing small scale turbulence (Sforza and Mons, 1969, Chen and Jirka, 1995). Only the asymptomatic decay region is visible on Figure 2.1.

In certain conditions, within turbulent flow, a Kármán vortex street can form, which is characterized by alternating low-pressure vortices that move downstream from an obstacle, as they are being shed periodically from the formation region. The timing of each release of vortices is approximately constant as long as the Reynold numbers remained unchanged; and the far-wake can be characterized as a sequence of distorted vortex loops arranged along a random yet symmetrical plane (Rosenhead, 1953).

2.1.3 Wake of Three-Dimensional Objects

For three-dimensional objects, the dual-wake concept is harder to apply, as the wake configurations observed vary significantly depending on the level of turbulence and nature of the object. Fan and Tsuchiya (1990) presents five categories of wake structure for three-dimensional objects, varying with the surrounding level of flow turbulence:

1. A steady wake with a negligible circulation region;
2. Steady wake with a well-developed circulation region followed by a laminar streamwise tail;
3. Unsteady wake with large-scale vortical structures consisting of a regular succession of vortex filaments, with the most plausible configuration being a non-axisymmetric vortex ring as a primary wake, followed by a series of the horseshoe vortex loops;
4. Unsteady wake with a high degree of turbulence, characterized by a progressive wave motion with a rotating flow separation region; and
5. A highly turbulent wake consisting of a pair of streamwise line vortices trailing from a horse-shoe shaped vortex ring fragment attached do the object.

The vortex structures observed within those categories vary considerably depending on the specific properties of the body opposing the current and the surrounding medium.

2.1.4 Quantifying Free Flow Turbulence

The flow regime provides insights as to how the air-water interface will vary when flow is impeded by an obstacle. The Froude number (*Fr*), defined in Equation 2.1, is a dimensionless value that quantifies gravity influence on fluid motion. In the current case, it is used to assess if the flow within the system is supercritical i.e., fast and rapid (*Fr>1*); subcritical i.e., slow and tranquil (*Fr<1*); or critical (*Fr=1*).

$$\mathrm{Fr} = \frac{V}{\sqrt{gH_d}}$$

Equation 2.1 : Froude

Where V is the mean water velocity within the system in m/s, H_d is the hydraulic depth in m and g is the gravitational constant in m/s^2. The Froude number can also be used for other applications by replacing H_d by a characteristic length variable and using local flow velocity. For example, to evaluate the drag or resistance of an object in water, the hydraulic depth would be replaced by the length of the object at the water line. In the current work, because of the level of submergence

of the spoiler baffles, the Froude evaluation was restrained to a characterization of the flow within the open canal.

The Reynolds number (*Re*), defined in Equation 2.2, is a dimensionless number which provides insights on the level of turbulence within a fluid. Depending on its value, the flow can be qualified as laminar, transitional or turbulent; the limits vary significantly depending on the location of the flow e.g., the limit of turbulence within a pipe is considerably higher that for an open-channel.

$$\mathrm{Re} = \frac{VL}{\nu}$$

Equation 2.2 : Reynold number

Where *L* is the chosen reference length in m and ν is the fluid kinematic viscosity in m^2/s. The Reynold number can be used to define the level of turbulence in multiple dimensions. If the hydraulic radius of the canal is used as the reference length, then the calculated Reynold number characterizes the overall level of turbulence of the flow within the canal. For low water depths, the influence of the bottom of the canal can be significant; using a reference length equal to the water depth can provide insights on the importance of vertical turbulence. If the spoiler baffle width is used, it will define the level of turbulence in the vicinity of the spoiler baffle. For CFD, the Reynold number has a direct impact on the computational grid, as the level of turbulence of a fluid impacts the formation of the near-wall boundary layer.

2.2 Impact of Turbulence on Fish

While flow turbulence is being heavily studied from a hydraulic perspective, much remains to be studied on the biological side, especially since there are contradictions between researchers studying the responses of fishes to turbulence and flow velocity, with fish behavioral variability between individuals and species having considerable impacts on results (Castro-Santos, 2005, Enders and Boisclair, 2016, Duguay et al., 2018).

In a physical experiment involving the use of flat triangular baffles to facilitate fish passage upstream a canal, Cabonce et al. (2018) observed that fish benefited from the presence of RVZs, but did not use them in the same manner depending on their size, with small fish seemingly disoriented by the presence of negative flow velocities downstream of the triangular baffles and preferring to rest upstream of them. On his end, Liao et al. (2003) observed that rainbow trout preferred holding station one to two body lengths downstream of a cylinder and away from the low-pressure suction regions, or RVZs. Turbulence has been shown to increase the cost of

locomotion for fish, but while highly chaotic turbulence seems to repel fish, steady and predictable turbulent structures can be exploited by certain swimming fish to aid in their upstream migration (Enders et al., 2003, Liao, 2007).

2.2.1 Eddy Size

Studies have shown that eddies can have both negative and positive impacts on fish depending on their size relative to fish body length, with most problems appearing for a relative size of approximately 1 (Cotel and Webb, 2015). Lindberg et al. (2016) further found that fish swimming performance diminished significantly when the eddy diameter exceeds approximately two-thirds of the fish body length, although this ratio varies across species and individuals. Thus, Cotel and Webb (2015) proposed that the ratio of eddy size to fish size be used as a standard parameter in determining thresholds for the fish's posture and trajectory within a system.

2.2.2 Eddy Momentum

The impacts the presence of eddies have on fish movement and migration have been studied by Taguchi and Liao (2011), who showed that while low average velocity contributed to a lower oxygen consumption by fish, this consumption was further decreased when fish were able to exploit vortices shed periodically within the wake of an object. Rainbow trout swimming in a vortex street were observed to beneficiate energetically from the presence of vortices in reduced velocity zones, more so when the turbulence was of the appropriate intensity, orientation and scale i.e., when they are able to slalom between vortices by adapting their body movement instead of swimming through the vortices (Liao et al., 2003). This adaptation of their swimming capabilities is termed Kármán gaiting, a specific form of swim performed by fish and that can be described by undulatory movements of the body of the fish superimposed with lateral translation and rotational motion, that generates body lift (Akanyey and Liao, 2013).

Cotel and Webb (2015) proposed the ratio between momentum of the eddy and the momentum of the fish also be used as a standard parameter. The momentum of the eddy can be estimated by calculating its circulation (Γ), which is a measure of rotation of a fluid (Childress, 2009) and is obtained by integrating vorticity (ω) over the surface (S) of an eddy (Equation 2.3).

$$\Gamma = \iint_S \omega \cdot dS$$

Equation 2.3 : Circulation

Whenever a fluid is rotating, vorticity is present. As per Childress (2009), the vorticity field $\vec{\omega}$ is used to describe the spinning motion of a continuum near a chosen point; it is the curl of the flow velocity ($\vec{u}$) of a fluid as defined in Equation 2.4.

$$\vec{\omega} = \nabla \times \vec{u}$$

Equation 2.4 : Vorticity field

Where ∇ is the del operator and represent the curl of the velocity vector field. OpenFoam can calculate vorticity for the user. Alternatively, within a closed recirculation zone, when the main vortex velocity is constant, the vorticity can be taken as twice the mean angular velocity vector of the water particles relative to the center of the eddy, oriented according to the right-hand rule (Shamloo et al., 2001).

2.3 Modelling Turbulence

In a three-dimensional turbulent flow, energy cascades from large scales to small scales via both strain self-amplification and vorticity stretching (Johnson, 2020). Motions of all scales affect one-another. Direct numerical simulations (DNS) give highly accurate results in modelling turbulence because they solve all motions sizes within a turbulent flow, large and small. However, very fine calculation meshes are required. Because of their massive computational needs, they are only suitable for very low Reynold numbers, making them impractical for everyday applications. Large eddy simulation (LES) was born from a need to solve turbulent flows at a lower computational cost.

LES enables the resolution of the large-scales motion of the flow, and modelling of the fine ones, thus rendering possible the use of a somewhat coarser mesh compared to DNS. Large-scale motions to be resolved are distinguished by applying a filter to the Navier-Stokes equations. The Navier-Stokes equations form the basis of any simulations which aim the modelling of turbulence. They express both the conservation of momentum and of mass, while accounting for the viscosity of the fluid, as shown in Equation 2.5, Equation 2.6 and Equation 2.7 for an incompressible fluid such as water (Fröhlich and Rodi, 2002).

$$\frac{\partial u_i}{\partial x_i} = 0$$

Equation 2.5 : Continuity

$$\frac{\partial u_i}{\partial t} + \frac{\partial (u_i u_j)}{\partial x_j} + \frac{\partial \Pi}{\partial x_i} = \frac{\partial (v\ 2S_{ij})}{\partial x_j}$$

Equation 2.6: Navier-Stokes

$$S_{ij} = \frac{1}{2}(\frac{\partial u_j}{\partial x_i} + \frac{\partial u_i}{\partial x_j})$$

Equation 2.7 : Strain rate tensor

Where S_{ij} is the strain rate tensor, $\Pi = p/\rho$ and v is the kinematic viscosity in m^2/s.

The filtering process can be implicit i.e., via discretization schemes; or explicit i.e., where the size of the filter is user-defined and serves to decrease the influence of the truncation error inherent to implicit filtering by reducing or removing smaller scales (Gullbrand, 2001). OpenFOAM uses a Schumann-type approach, within which calculations start from a finite volume mesh (Castano et al., 2019). For each cell, the Navier-Stokes equations are discretized, which result into the splitting of large and small-scale motions. While this approach facilitates the use of inhomogeneous and anisotropic grid, it implies a close tie-in between scale separation, discretization and the subgrid-scale (SGS) model, making it difficult to assess the contributions of each stage to the overall error (Fröhlich and Rodi, 2002).

2.3.1 The Solvers

LES is a time-dependant model and transient solvers must be used. Steady-state solvers reach a specific solution in a given number of iterations, while transient solvers calculate a complete solution for every timesteps, enabling the capture of the dynamic formation of eddies and vortices associated with turbulence. In OpenFOAM, transient solvers that can be used in modelling turbulence include:

- interFoam, a multi-phase standard solver that enables modeling of free surface flow using the volume of fluid method;
- pisoFoam, a one-phase solver for incompressible flow;
- pimpleFoam, a one-phase large time-step transient solver for incompressible flow. It merges the PISO and SIMPLE algorithms; the latter being used for steady-state incompressible flow with turbulence.

The main difference between pisoFoam and pimpleFoam resides in the number of inner and outer iterations that those solvers can complete when solving the matrices of equations of a model. Within pimpleFoam, it is possible to set a specific number of inner correctors which define how

many times the pressure will be corrected within one iteration; while outer correctors define how many times the system of equations will be solved before the solver is forced to move onto the next timestep. Thus, pimpleFoam provides more stability at an increased time-step size, but to a higher computational cost. To make pimpleFoam act like pisoFoam, the outer corrector can simply be set at a value of one.

The pisoFoam algorithm is the one that is mostly used for LES studies, including pimpleFoam operated in PISO mode. Castano et al. (2019) have shown that with the PISO algorithm, errors on pressure tend to accumulate in time for very low Courant numbers, thus making pisoFoam more dissipative in nature. However, the numerical dissipation of this algorithm does not seem to overwhelm the effect of the SGS model and is therefore still considered a reasonably good algorithm of LES studies.

2.3.2 Discretization

In OpenFOAM, discretization schemes must be chosen for various variables to allow solving of the equations of the system for each point within the computational grid. In implicit filtering, the smallest resolved scales are significantly affected by the chosen schemes, which impact the contribution of the SGS model (Fröhlich and Rodi, 2002). Edoh and Gallagher (2018) showed that high-order discretization schemes helped decrease those numerical errors.

2.3.3 The Smagorinsky Model

While many SGS models are made available within OpenFOAM, this thesis focuses on the Smagorinsky model, well liked for its simplicity. The Smagorinsky model can be used classically or dynamically. In the latter, the Smagorinsky coefficient is defined locally in time and space, thus requiring extra computational strength. Using the Runge-Kutta algorithm, Mallik et al. (2020) showed that the classical Smagorinsky model performed better than the Dynamic Smagorinsky model for turbulent channel flow simulations.

With the classical Smagorinsky model, the Reynolds stress tensor (τ_{ij}) is considered proportional to the filtered strain rate tensor ($\bar{S}_{ij}$), and the eddy viscosity (v_s) is defined as:

$$v_s = (C_s\Delta)^2\left|\bar{S}_{ij}\right|$$

Equation 2.8 : Eddy viscosity

The Smagorinsky constant (C_s) is usually varied between 0.1 and 0.2; larger values can give smoother spatial structures of turbulence but in the extreme, they lead to large-scale decay (Zou et al., 2006).

In OpenFOAM, the default C_s value is approximately 0.168. Because of the way the Smagorinsky model is implemented in OpenFOAM, the value of C_s is difficult to adjust (fumiya, 2016). It varies following the value of two model constants set in the source code, namely C_k, which has a value of 0.094, and C_ϵ, which has a value of 1.048. In OpenFOAM, for an incompressible fluid and assuming an equilibrium between the subgrid scale energy production and its dissipation, the subgrid scale viscosity (v_{sgs}) is defined as:

$$v_{sgs} = C_k \Delta \sqrt{\frac{C_k \Delta^2 |\overline{D}|^2}{C_\epsilon}}$$

Equation 2.9 : Subgrid scale viscosity

Where $\overline{D}$ is the resolved-scale strain rate tensor. The subgrid length scale (Δ) can be calculated different ways.

Used on a fine mesh, the Smagorinsky model can provide accurate and realistic results when modeling flow turbulence (Chorda et al., 2019) and can accurately predict the U-shape of the mean streamwise velocity in the case of a separated flow (Feng et al., 2021). However, the Smagorinsky model tends to overestimate flow dissipation, leading to a significantly lower velocity near walls (Pakzad, 2017), as well as in the wake area of an object (Feng et al., 2021). Use of a wall damping function such as Van Driest, coupled with a very fine mesh, can compensate for this over-dissipation effect (Pakzad, 2017). The Van Driest damping function (D) is defined in Equation 2.10, and its associated length scale in Equation 2.11.

$$D = 1 - e^{\left(-\frac{y^+}{A^+}\right)}$$

Equation 2.10: Van Driest damping function

$$\Delta = \min\left(\frac{k \cdot y}{C_D} D, \Delta_g\right)$$

Equation 2.11: Subgrid length scale

In Equation 2.11, Δ_g is a geometric-based delta function, such a cube-root volume; and C_D can be calibrated but has a starting value of 0.158. For a smooth wall, Van Driest (1956) recommends a value of 27 for A^+ and a value of 0.4 for k, which are both user-specified. While y is the distance

from the wall, the y^+ value is a non-dimensional distance used to describe how fine a computational mesh is; it is a normalized distance. For best results with the Smagorinsky model coupled with the Van Driest damping function, the first cell centre near the wall should be maintained below y+=1 if at all possible, and y+ kept under 10 for the overall mesh (Cintolesi and Mémin, 2020).

2.3.4 Mesh Sizing

For a wall-resolved LES, the y+ value is kept under 1 in the near wall-region. However, since this leads to substantive computational needs, the near-wall region can also be wall-modeled via the use of wall functions. Each function requires a specific range of y^+ values. Following the methodology of Van Driest (1956), the y^+ value can be estimated by:

$$y^+ = \frac{y \cdot u_*}{v}$$

Equation 2.12 : Normalized distance from wall

Where y is the span of the mesh cells normal to the wall in m; and u_* is the friction velocity in m/s calculated from:

$$u_* = \sqrt{\frac{\tau_w}{\rho}}$$

Equation 2.13 : Friction velocity

In Equation 2.13, ρ is the density of the fluid in kg/m^3 and the wall shear stress (τ_w), in Pa, is obtained from:

$$\tau_w = C_f \cdot \frac{1}{2}\rho V^2$$

Equation 2.14 : Wall shear stress

Where C_f is a friction coefficient which, for a Reynold number under 10^9, varies following:

$$C_f = \left[2log_{10}(Re_f) - 0.65\right]^{-2.3}$$

Equation 2.15 : Coefficient of friction

The friction Reynold number (Re_f) is calculated by using the length of the canal as the reference length in Equation 2.2.

While the computational needs of LES are reduced compared to DNS, they are still quite massive, rendering the wall-resolved strategy difficult to apply for high Reynold numbers and large meshes. Nicoud et al. (2001) showed that accurate modeling of the mean velocity profile in the near-wall region can also be ensured by forcing the outer LES towards the desired solution by setting a specific wall stress boundary condition as control. While efficient for Reynold numbers

varying between 640 and 20,000, the suboptimal control strategy is hard to apply since wall stress cannot be predicted. Therefore, wall-modeled LES are most commonly used for higher Reynold numbers.

The use of wall functions assume that an equilibrium layer exists into which the wall-stress is constant. This assumption does not hold in the case of a separated flow, when the mean velocity is three-dimensional (Piomelli, 2008). A fine enough mesh should be used around the object to make this specific area wall-resolved. Additionally, the computational grid should be the most equispaced possible (Fröhlich and Rodi, 2002).

3 METHODOLOGY

3.1 Details of Physical Experimentation

The CFD models were calibrated using measurements obtained from the physical experimentation of Alexandre Pirolley (INRS) which had, for main objective, the evaluation of the response of fish to profiled spoiler baffles when facing challenging hydraulic conditions (Pirolley, 2021).

The experimentation was completed in an acrylic canal with a length of 6.3 meters, a width of 0.31 meters and a height of 0.3 meters. Two reservoirs, connected by an acrylonitrile butadiene styrene pipe with a diameter of 101.6 mm, were attached to the canal: one to its upstream end, and the other to its downstream end. A diffuser was installed at the inlet to mitigate the turbulence generated by the reservoir overflow. About 3,000 liters of water was poured into this closed system, until a water depth of 16 centimeters was reached within the canal, installed horizontally. Flow velocity was controlled via a five inches MEGGA PCF-4L pump. In order to keep the fish in the vicinity of the spoiler baffles, two steel grates, with openings of 5.5 mm by 5.5 mm, were installed at a respective distance of 2.23 m and 4.53 m from the upstream end of the canal. The final testing area measured 0.713 m^2 (Figure 3.1).

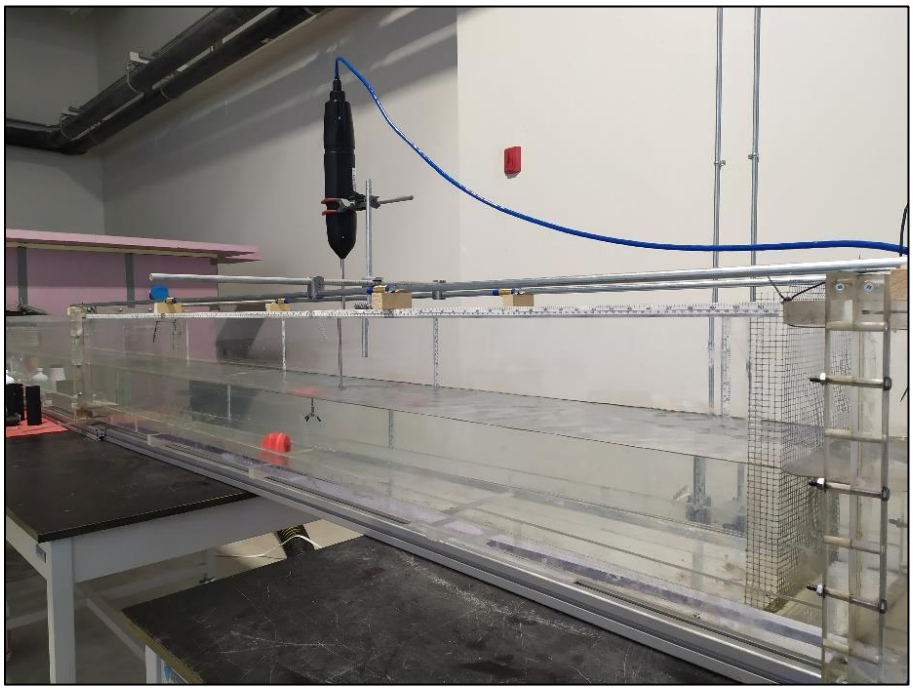

Figure 3.1 Picture of the canal used during the physical experimentation (credit: Alexandre Pirolley)

The profiled spoiler baffles tested were drawn in the opensource software FreeCAD before being printed in 3D. Both the height (H) and the width (W) of the spoiler baffles were varied between 20 mm, 30 mm and 40 mm, for a total of 9 spoiler baffles. A schematic of the general shape of the spoiler baffles is presented in Figure 3.2. The chosen shape aimed to graciously separate flow, keeping the turbulence generated on the upstream side of the spoiler baffle to a minimum, in accordance with the current work's objective of creating a stable reduced velocity zone (RVZ) downstream of the spoiler baffle while minimizing head loss through the canal.

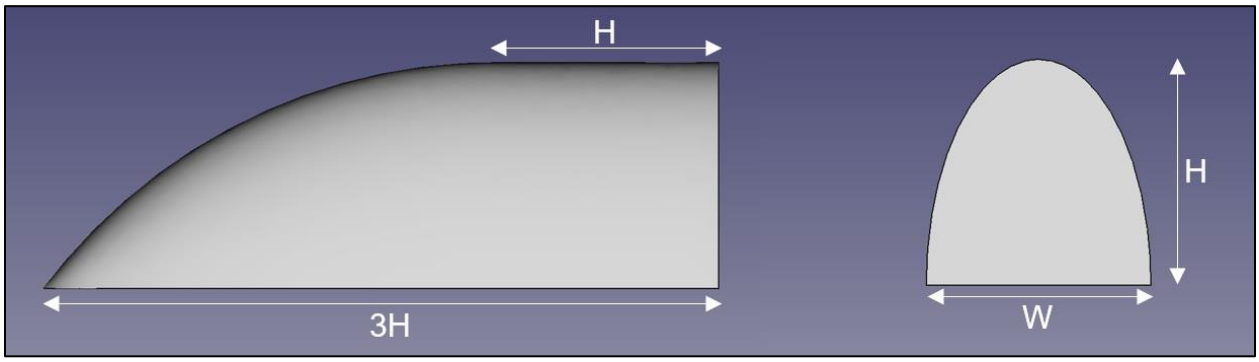

Figure 3.2 : Schematic of the side and front views of the spoiler baffles

In order to reduce the complexity of the flow within the canal and facilitate the analysis of the impacts of the spoiler baffle itself on flow, only one spoiler baffle was installed within the canal, with its middle line aligned with the middle of the canal. The distance between the downstream face of the spoiler baffles and the upstream steel grate was maintained at 1.19 meters to ensure consistency and facilitate the installation of the spoiler baffles. All measurements and observations were completed under two hydraulic conditions (Table 3.1). A list of all the simulations completed is presented in Table 3.2.

Table 3.1 : Hydraulic conditions tested during the physical experimentation

Hydraulic Conditions	**#1**	**#2**
Flow Rate	0.0127 m^3/s	0.0163 m^3/s
Average Flow Velocity	0.268 m/s	0.356 m/s
Average Water Depth	0.152 m	0.148 m
Reynold Number	15,800	16,900
Froude Number	0.31	0.35

Table 3.2 : List of simulations

Name of Simulation	Description of Simulation
Canal_01	No spoiler baffle installed, hydraulic condition #1
h20w20_01	Spoiler baffle with a height of 20 mm and a width of 20 mm installed, hydraulic condition #1
h20w20_02	Spoiler baffle with a height of 20 mm and a width of 20 mm installed, hydraulic condition #2
h20w30_01	Spoiler baffle with a height of 20 mm and a width of 30 mm installed, hydraulic condition #1
h20w30_02	Spoiler baffle with a height of 20 mm and a width of 30 mm installed, hydraulic condition #2
h20w40_01	Spoiler baffle with a height of 20 mm and a width of 40 mm installed, hydraulic condition #1
h20w40_02	Spoiler baffle with a height of 20 mm and a width of 40 mm installed, hydraulic condition #2
h30w20_01	Spoiler baffle with a height of 30 mm and a width of 20 mm installed, hydraulic condition #1
h30w20_02	Spoiler baffle with a height of 30 mm and a width of 20 mm installed, hydraulic condition #2
h30w30_01	Spoiler baffle with a height of 30 mm and a width of 30 mm installed, hydraulic condition #1
h30w30_02	Spoiler baffle with a height of 30 mm and a width of 30 mm installed, hydraulic condition #2
h30w40_01	Spoiler baffle with a height of 30 mm and a width of 40 mm installed, hydraulic condition #1
h30w40_2	Spoiler baffle with a height of 30 mm and a width of 40 mm installed, hydraulic condition #2
h40w20_01	Spoiler baffle with a height of 40 mm and a width of 20 mm installed, hydraulic condition #1
h40w20_02	Spoiler baffle with a height of 40 mm and a width of 20 mm installed, hydraulic condition #2
h40w30_01	Spoiler baffle with a height of 40 mm and a width of 30 mm installed, hydraulic condition #1
h40w30_02	Spoiler baffle with a height of 40 mm and a width of 30 mm installed, hydraulic condition #2
h40w40_01	Spoiler baffle with a height of 40 mm and a width of 40 mm installed, hydraulic condition #1
h40w40_02	Spoiler baffle with a height of 40 mm and a width of 40 mm installed, hydraulic condition #2

3.1.1 Data Available for the Calibration and Validation of the CFD Models

Data available for the calibration and validation of the CFD models include:

1. **Water depths** | A ruler was used to manually measure water depths every 68 cm along the length of the canal.
2. **Videos** | Ink was injected downstream of the spoiler baffle via a dropper and filmed to assess the behavior of the RVZ and gauge its size.

3. **Instantaneous velocities** | Water velocities were recorded at a frequency of 25 Hz over 180 seconds using an acoustic doppler velocimeter (ADV). Velocity was recorded twice within the water column, namely at z = 7.5 mm and at z = 1H from the bottom of the canal. The location of the velocity measurements along the length of the canal varied following the height of the spoiler baffles. Toward the upstream end of the canal, starting from the downstream face of the spoiler baffle (y = 0), measurements were taken at -1H, -2H, -4H, -8H and -13H; toward the downstream end of the canal, they were taken at 1.5H, 2H, 2.5H, 3H, 5H, 10H and 20H. One extra measurement was taken for all spoiler baffles 30 mm from their downstream face. A total of six lines of measurements were taken, located at three different locations along the width of the canal. The location of those lines varied following the width of the spoiler baffle installed: two lines were taken for the middle of the canal (x = 0), and the others were taken at a distance of W/2 and 3W/2 from the middle of the canal. Velocities within the canal without any spoiler baffle installed were also recorded, resulting in a total of 20 datasets available for the validation of the CFD models, constituted of eleven water levels and of maximum 78 velocity points.

3.2 Details of the CFD Modelling Work

3.2.1 Mesh Building

LES are computationally intensive because very fine computational grids are required to ensure reliable results and convergence of the model. The meshes were built in two steps. First, equidistant calculation grids having the required dimension were built using the OpenFOAM function *blockMesh*. Then, the shape of the spoiler baffle was cut into the modelled canal using the function *snappyHexMesh* and the FreeCAD 3D models previously created by Alexandre Pirolley.

Because of computational constraints, the minimal size of the grid, in all direction, was maintained at 0.001 meters, resulting in a y+ value of 10 for hydraulic condition #1 and a y+ value of approximatively 13 for hydraulic condition #2. In order to decrease the memory requirement and the time of calculation for all simulations, the size of the meshes was varied following the height of the spoiler baffle, as follows:

- A distance of 3.5H was maintained between the inlet of the model and the beginning of the profiled slope of the spoiler baffle;

- A distance of 20H was maintained between the downstream face of the spoiler baffle and the outlet of the model.

The characteristics of the meshes used for each scenario are summarized in Table 3.3.

Table 3.3 : Characteristics of the meshes developed for all simulations

Parameter		**HC #1**	**HC #2**
Height of Mesh		0.152 m	0.148 m
Width of Mesh		0.31 m	0.31 m
Length of Mesh	**Spoiler baffle with a height of 2 cm**	0.53 m	0.53 m
	Spoiler baffle with a height of 3 cm	0.795 m	0.795 m
	Spoiler baffle with a height of 4 cm	1.06 m	1.06 m
Grid Size		0.001 m	0.001 m
y+ value		10	13

The mesh created for the spoiler baffle h20w20 is presented in Figure 3.3 as an example. The length of the canal extends from upstream to downstream following the Y-axis, with the origin located at the downstream face of the spoiler baffle. The width of the canal extends parallel to the X-axis, with the origin aligned with the middle of the spoiler baffle. The height is in the Z-axis direction with the origin located at the bottom of the canal.

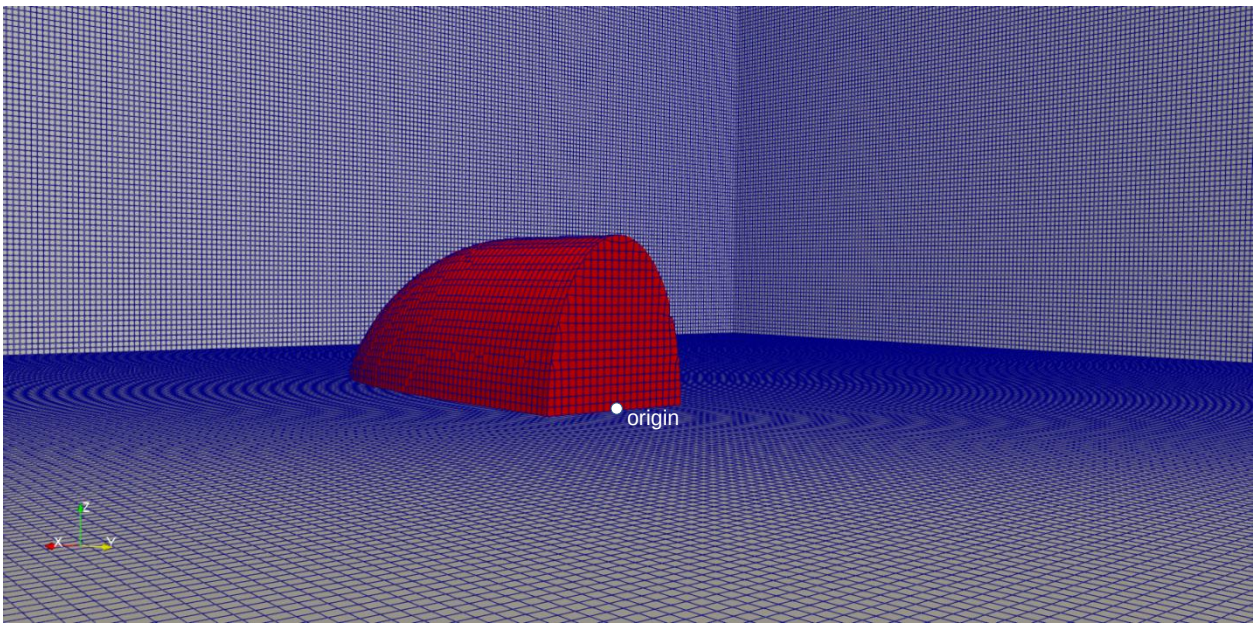

Figure 3.3 : Example of computational grid (example taken from h20w20_01)

3.2.2 Calculations Setup

The *constant* folder of each case is where the calculation models are setup, namely using the *fvOptions*, *momentumTransport* and *transportProperties* files. The Smagorinsky model was chosen within the *momentumTransport* file, coupled with the Van Driest damping function.

The recommended values for a smooth wall were set for *kappa* and *Aplus*, namely 0.4 and 27 respectively (Van Driest, 1956). The *Cdelta* variable was kept at its standard value of 0.158. The transport model used for the LES is Newtonian, with the water kinematic viscosity set at 1.31×10^{-6} m^2/s. The momentum source of the model is calculated using the *meanVelocityForce* approach instead of the gravity constant for the proper modelling of the use of a pump. The chosen discretization scheme for time is *backward*, a second order approach. *Gauss linear* was set for both the gradient and divergence schemes. *Gauss linear corrected* was set for the Laplacian scheme and interpolation is done linearly. Finally, the corrected surface-normal gradient scheme is used.

The algorithm used to solve the LES is the monophase *pimpleFoam* algorithm, used in its *piso* mode i.e., the outer correctors number is set to 1 and the number of correctors is set to 2. A relaxation factor of 0.4 was used to facilitate convergence of the model. For pressure, the *GAMG* solver is used; and for velocity, the *smoothSolver* is used. Based on the water velocity and final size of the cell of the mesh, a timestep of 0.001 seconds was used to ensure the maximum Courant number would be maintained under a value of 1.

3.2.3 Boundary Conditions

The Smagorinsky model does not require any added parameters; boundary conditions needed to run the simulations are for the standard parameters, namely the velocity, the pressure and the wall closure models, and are set within the *0* folder of each case.

For the velocity, the *noSlip* condition was used for the spoiler baffle and for all walls of the canal, while the *slip* condition was used on the top face of the system to mimic an air-water interface. For the inlet of the model, the *turbulentInlet* condition was used with a uniform fluctuation scale of 0.1 to reproduce the diffuser installed at the upstream of the canal. At the outlet, the *inletOutlet* condition was used, which forces the water out of the model, acting like the *zeroGradient* condition, but negating any backward flow.

In LES, a pressure gradient only serves to set where the water enters the computational grid and where it exits. Therefore, the *zeroGradient* condition was used at all boundaries except at the outlet, where a *fixedValue* condition of 0 was used.

For the wall closure models, the boundary condition *nutUSpaldingWallFunction* was used for the walls of the canal and for the spoiler baffle, which provides a constraint on the turbulent viscosity based on the flow velocity, and works well for a wide range of y+ value. For the atmosphere, the *zeroGradient* condition was applied. The inlet and outlet conditions were set to be calculated by OpenFoam.

3.2.4 Hardware

All simulations were run on Carcajou003, one of the supercomputers available through the *Institut national de la recherche scientifique*. Carcajou003 was given 20 physical cores and 100 GB of RAM, necessary to successfully run all simulations. Despite the strength of this hardware, some cases took as long as 5 days for completion.

3.3 CFD Model Calibration

Calibration of the CFD model was done simultaneously with its development. The model was ran numerous times using various builds and comparing results with the recorded velocity datasets for all points. Initially, the calibration process pointed to a tendency of the model to provide much faster velocities in the near-wall boundary layer than what was recorded. The near-wall turbulence closure models were varied, but adding the Van Driest damping function to the Smagorinsky model is ultimately what allowed for a better reproduction of all velocities. A sensitivity analysis was also completed by modifying various coefficients that did not result in significant changes in the modelled velocities. This overall stability of the model was attributed to the use of a very fine mesh (Fröhlich and Rodi, 2002). The remaining lack of accuracy was considered inherent to the Smagorinsky model and inability to modify its coefficients in OpenFOAM.

3.4 Data Analysis and Post-Processing

3.4.1 Videos of Physical Model

All videos of the physical model were thoroughly analyzed to better understand how the size of the RVZ evolved over time. Images of the videos were extracted and processed in the free software IMAGEJ to measure the length of the RVZ. This analysis is founded on the premise that

it is possible to measure the length of the RVZ on the images, as long as the measure is made within the same plane as the measure of the known length of the spoiler baffle, used to calibrate the ratio of pixels to length in millimetres. However, because of perspective distortion, this methodology suffers strong limitations and uncertainties, and can only be used to provide a rough estimate of the physical length of the RVZ and its overall behaviors.

Figure 3.4 presents the image used to measure the RVZ generated by the spoiler baffle with a height of 40 mm and a width of 20 mm. To minimize the uncertainties for this analysis and quantify the variance of the results, the length of the spoiler baffle (yellow line on Figure 3.4), used to calibrate the ratio of pixels to length of the video image, was measured three times for each image. The video was observed carefully to identify how the RVZ behaved and extract an image where it was particularly visible. Two measurements were then taken i.e., one for what was understood as being the shortest possible length for the RVZ (blue line on Figure 3.4), and another for the longest visible length on the image (green line on Figure 3.4). This enabled the calculation of the average RVZ length and an estimate of the variance of the measurements.

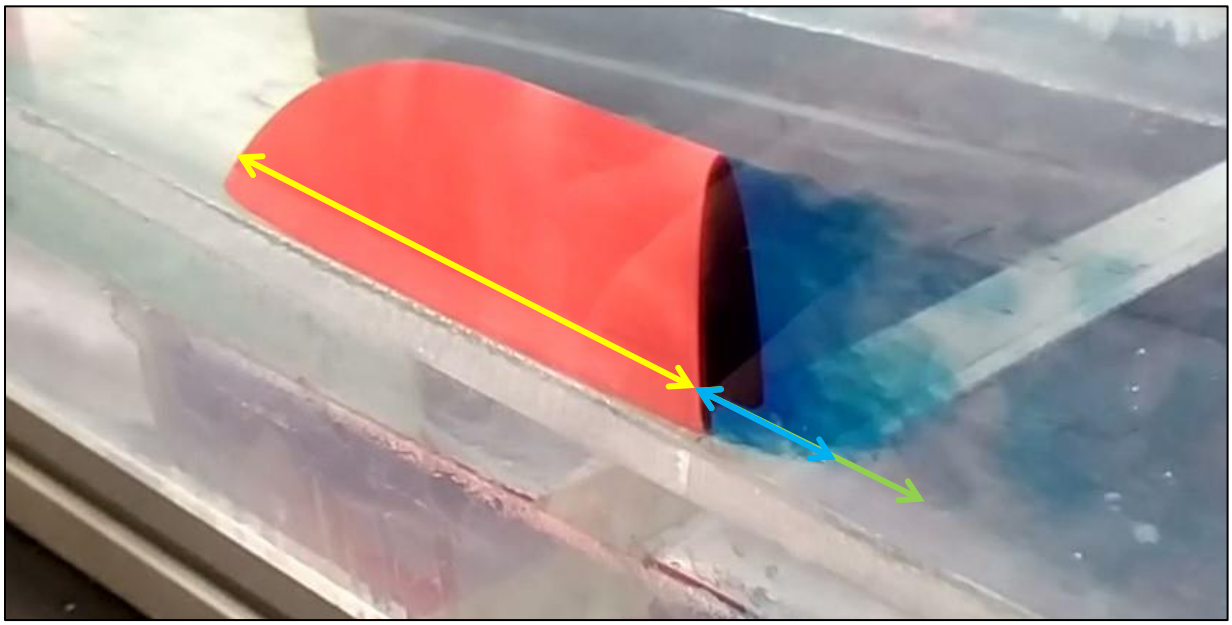

Figure 3.4 : Image processing methodology used to estimate the length of the RVZ generated by the spoiler baffle h40w40_01 during the physical modelling work. The yellow line is the calibration line; the blue line is the shortest estimated length; and the green line is the longest estimated length of the RVZ.

3.4.2 Recorded Velocities

Velocities within the canal were recorded in all directions (x-axis, y-axis, z-axis), but only velocities in the direction of the current were considered for the current work, as velocities in the x- and z-axis were mostly null. Velocities recorded by the ADV and used as part of this thesis have been

post-processed using version 2.031 of the WinADV32 software. Communication error removal was performed by filtering the raw data ensuring a signal to noise ratio (SNR) under 5 dB and an average correlation of values (COR) under 70%; suspicious values that did not correspond to natural fluctuations in the flow, but rather to the reverberation of the signal on the walls of the channel were eliminated using the phase-space thresholding method (Pirolley, 2023). The recorded instantaneous velocities vary considerably over time, with an example provided in Figure 3.5, which presents the recorded velocity magnitude for the canal_01 setting.

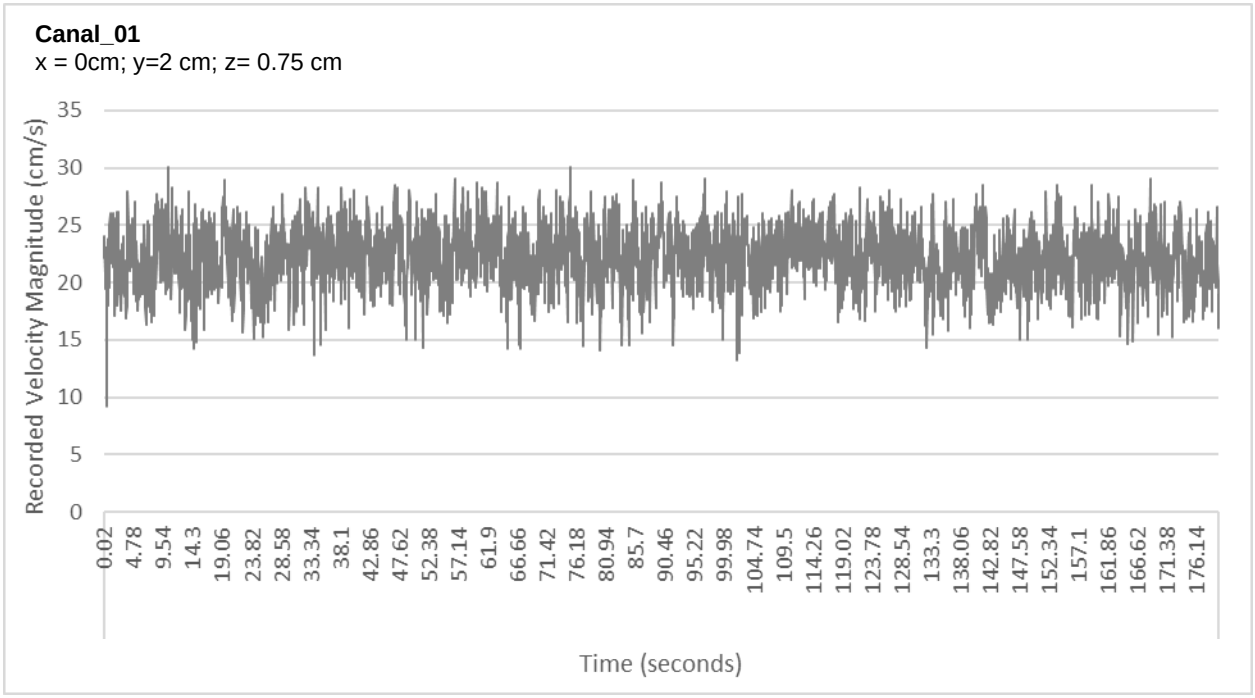

Figure 3.5 Instantaneous velocities recorded during the physical experimentation - no spoiler baffle | HC#1. The position of the recorder, per the computational mesh coordinates, is at (x= 0, y = 2, z = 0.75) cm.

Simulation results from LES consist in a snapshot in time of the flow velocity within the canal. Because turbulence is also being modeled, the velocity at one specific point will change from one moment to the next. Compared to RANS, LES does not provide average velocities, but instantaneous ones. In order to obtain average velocities from a LES, the function object *fieldAverage* can be used in OpenFOAM. Within the scope of the current work, to save on computing power, the minimum, average and maximum recorded filtered velocities were calculated and directly compared to the modelled instantaneous velocities of the CFD models at time t = 14 seconds.

This methodology is based on the hypothesis that obtaining modelled instantaneous velocities within the minimum and maximum recorded velocities would be indicative of the model

reproducing the conditions within the canal, albeit a bias might be present. It is also hypothesized that from one simulation to the next, an accurate model should provide instantaneous velocities varying from one side to the other of the recorded average velocity; the contrary i.e., all simulations giving modelled velocities either above or under the recorded average, would be indicative of a bias or model tendency to either overestimate or underestimate velocities. The recorded average velocity was subtracted from the modelled instantaneous velocity, and data was analysed to identify any possible tendency in the model; the closer the medians and averages are to a value of 0, the more accurate the model would be. While it is acknowledged that this methodology constitutes a limit to the precision of our validation process, it is not believed that the conclusions and modelling decisions would have differed if average velocities had been used during the validation process instead; this methodology still allows for the identification of the model's biases.

3.4.3 CFD Results

All CFD simulations results were analyzed in ParaView, an open-source, multi-platform data analysis and visualization application which comes hardcoded within OpenFoam.

3.4.3.1 Measurements of the Wake and RVZ Generated by the Spoiler Baffles

The height, width and length of the wakes and of the RVZs generated by the spoiler baffles were measured following the subsequent guidelines (Figure 3.6).

- The wake of the object refers to the region of flow showing high disturbances both in velocity and directions. To facilitate measurements of the wake, a clear limit was set at v = 0.21 m/s for hydraulic condition #1, and at v = 0.25 m/s for hydraulic condition #2, both defined as a bright yellow line in ParaView;
- The RVZ is defined as the region of the wake, fragmented or not, with a flow velocity under 0.10 m/s for hydraulic condition #1, and under 0.12 m/s for hydraulic condition #2, both defined as a bright cyan line in ParaView;
- The length of the wake and RVZ are averaged using 6 measurements taken over two elevations, namely z = 7.5 mm and z = 2H/3, and over three locations along the width of the spoiler baffle, namely x = 0 mm, x = -W/4 and x = W/4.
- The height and width of the wake and RVZ are averaged using all measurements, which are taken every 2 cm from the downstream face of the spoiler baffle over the measured lengths.

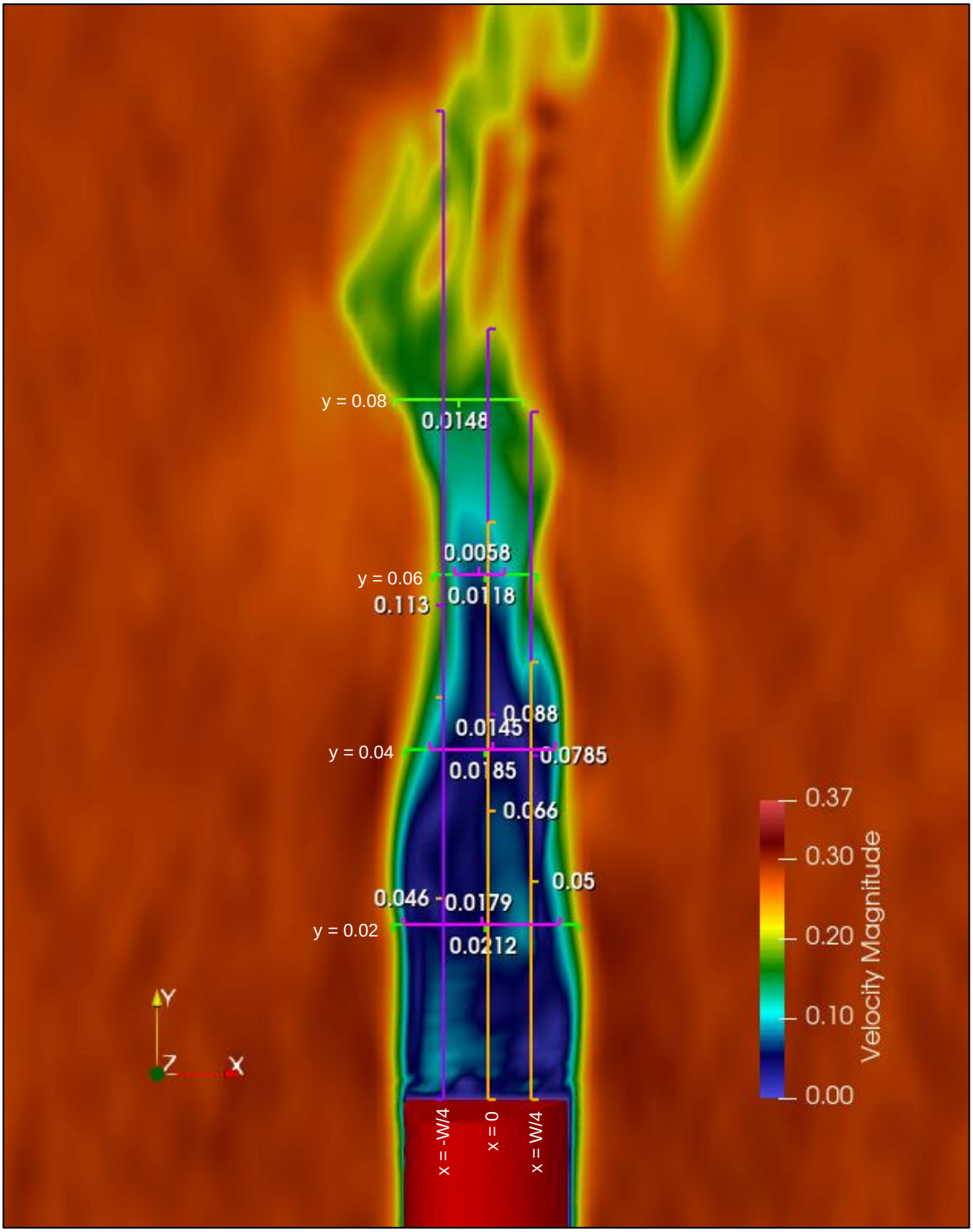

Figure 3.6 : Measurements of the spoiler baffle's wake length (purple) and width (green), and of its RVZ length (orange) and width (pink), in Paraview. Example taken from simulation h20w20_01, at z = 7.5 mm.

The limit of the RVZ was defined by analysing the stream lines forming downstream of the spoiler baffles and ensuring the capture of circulating flow patterns that are characteristics to the wake of an object (Fan and Tsuchiya, 1990). For many spoiler baffles, vortex shedding was observed that led to the creation of reduced velocity pockets downstream of the object. Those pockets had higher velocities than the identified RVZ, yet did not match the average velocity of the canal and were therefore considered part of the object wake. Thus, a second limit was deemed necessary i.e., the wake limit.

The limits for the RVZ and wake respectively correspond to 27% and 57% of the maximum recorded velocity within the canal for both hydraulic conditions. Using a percentage of the maximum recorded velocity value allows a better analysis of how the RVZ and wake regions for a same object will evolve under different hydraulic conditions, as the comparison considers the velocity gradient and energy within the system, which affect the average flow velocity within a closed recirculation region.

3.4.3.2 Measurement of the Confined Turbulent Wake Region

Following the literature review, it was hypothesized that the confined turbulent wake region (Figure 2.2) could be construed as the RVZ; it seemed like a particularly interesting characteristic to evaluate. Only the length of the confined turbulent wake region was measured, as its width and height are defined by the same limits than when using flow velocities. In order to identify the cut-off stream outlining the confined turbulent wake region, the StreamTracer tool of Paraview, which uses seed points within the modelled vector field to allow the visualisation of stream lines, was set at a depth of 7.5 mm and extended across the width of the spoiler baffle to allow a proper visualization of the stream lines. The confined turbulent wake region length was then measured from the spoiler baffle downstream face up to the first line crossing the region from one side of the shear-layer to the other, with a visual aid provided in Figure 3.7.

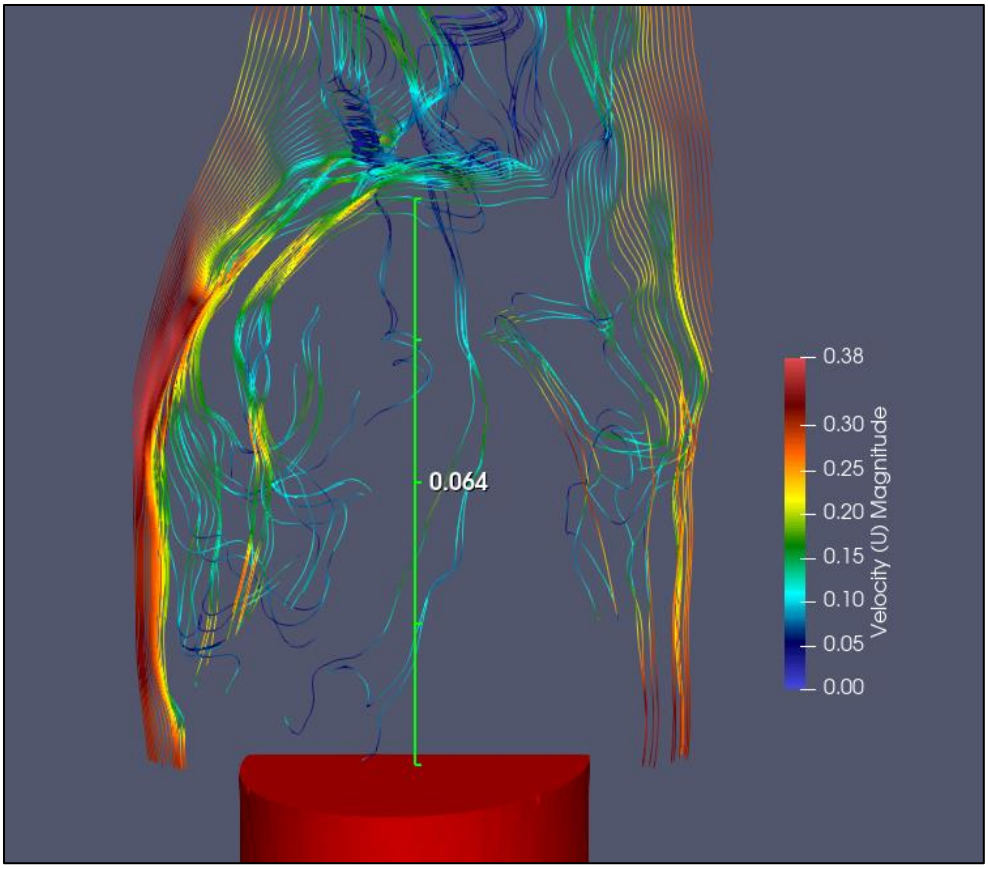

Figure 3.7 : Example of the measurement of the confined turbulent wake region using the StreamTracer tool of Paraview, on simulations results from h40w40_01, at z = 7.5 mm

3.4.3.3 Definition of the Fragmentation Level of the Modelled RVZ

A fragmentation level was attributed to the RVZ. This level refers to the presence of higher velocity zones within the RVZ. A low level of fragmentation indicates a uniform, low speed RVZ while a strong level indicates frequent regions of higher velocities contained within the envelop of the RVZ. This definition is highly qualitative and based on the judgment of the observer, yet it should still provide some useful information on how the level of turbulence of the RVZ generated by a spoiler baffle varies following the characteristics of the spoiler baffles.

3.4.3.4 Analysis of the Vortices Generated Within the RVZ

The vortices generated within the RVZ were analysed using the StreamTracer tool of Paraview to better understand the nature of the RVZ created. The StreamTracer tool can be moved around the vector field to get a thorough comprehension of the vortices modelled within a system at a precise moment of a simulation. Observations were systematically noted to identify patterns between simulations.

4 RESULTS

Results of the CFD modeling work are presented in three sections. First, the CFD models were validated to ensure the obtained variability and accuracy were within an acceptable range, and to identify possible causes of discrepancies. Second, the sizes of the wake and of the RVZ are presented, with the assessment focussing on the effects of the size and geometry of the spoiler baffles, and surrounding hydraulic conditions (HC), on the results. Finally, details are given on the identified vortices observed within the RVZ and on how fish could potentially respond to the RVZ.

4.1 Validation of the CFD Models

Part of the validation process requires comparing the instantaneous velocities modelled by the LES to the recorded velocities, while the other part aims to compare the length, width and height of the modelled RVZs to the length, width and height of the observed RVZs.

4.1.1 Recorded Against Modelled Velocities

All figures comparing the minimum, average and maximum recorded filtered velocities to the modelled instantaneous velocities are annexed to this manuscript (Appendix 1). Analysing those figures showed that generally, the instantaneous velocities modelled by the Smagorinsky model are within the range of the recorded velocities; and that less variability is observed within the modeled instantaneous velocities than within the recorded instantaneous velocities. Most velocity points outside the range of the recorded velocities are under the minimum recorded velocity, indicating that the model seems to overestimate the width of the RVZ. Finally, the meshes having a y+ value of 13 (HC#2) were not associated to any loss of accuracy compared to the meshes having a y+ value of 10 (HC#1).

Boxplots of the difference between the recorded and modeled velocities were plotted for each location where flow velocities were recorded and are provided in Figure 4.1, Figure 4.2, Figure 4.3 and Figure 4.4. Because hydraulic conditions were not shown to impact anything other than the width of the RVZ (section 4.2.1), all simulations were lumped together for the calculations of the boxplots. Generally, the differences between the modelled and recorded velocities are symmetrically distributed, as indicated by the mean and median values being close to each other. A higher variability is observed in the shear layers, in proximity of the spoiler baffles. A model trend can be inferred for boxplots having a median value consistently above or under zero, with

positive values indicating an overestimation of the recorded velocities, while negative values indicate an underestimation.

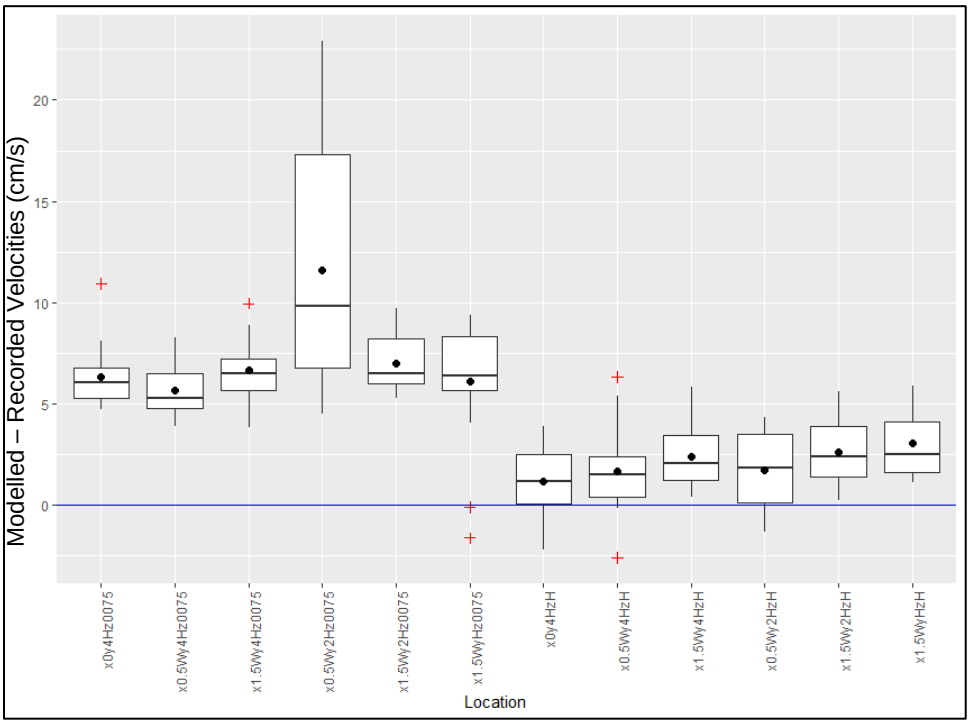

Figure 4.1 : Difference between modelled and recorded velocities for various locations upstream of the spoiler baffles

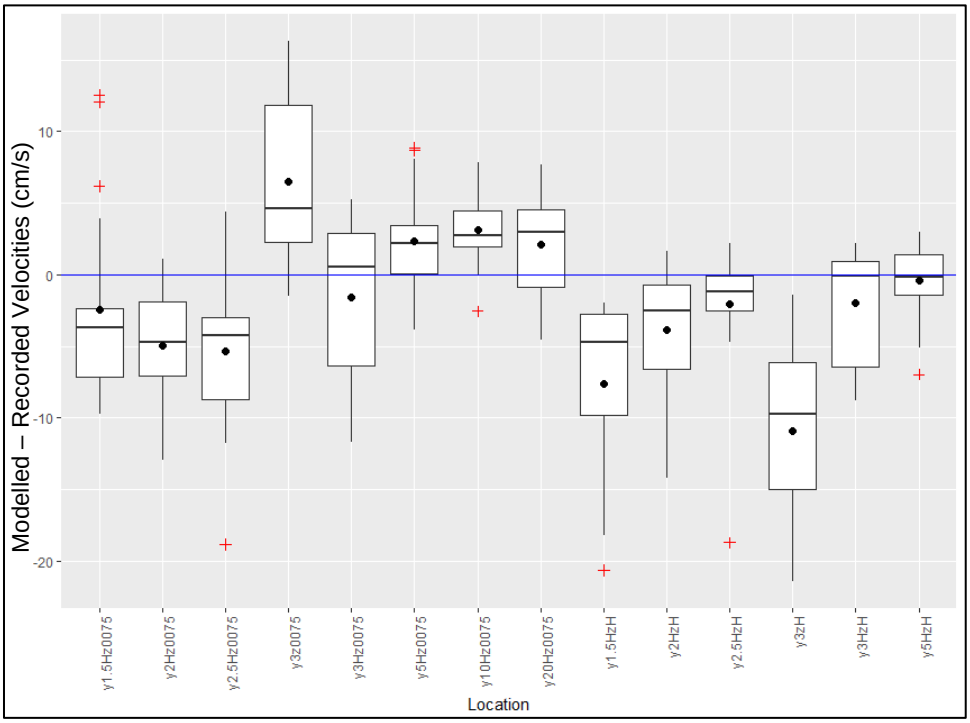

Figure 4.2 : Difference between modelled and recorded velocities for various locations downstream of the spoiler baffles, in the middle of the Canal (x=0)

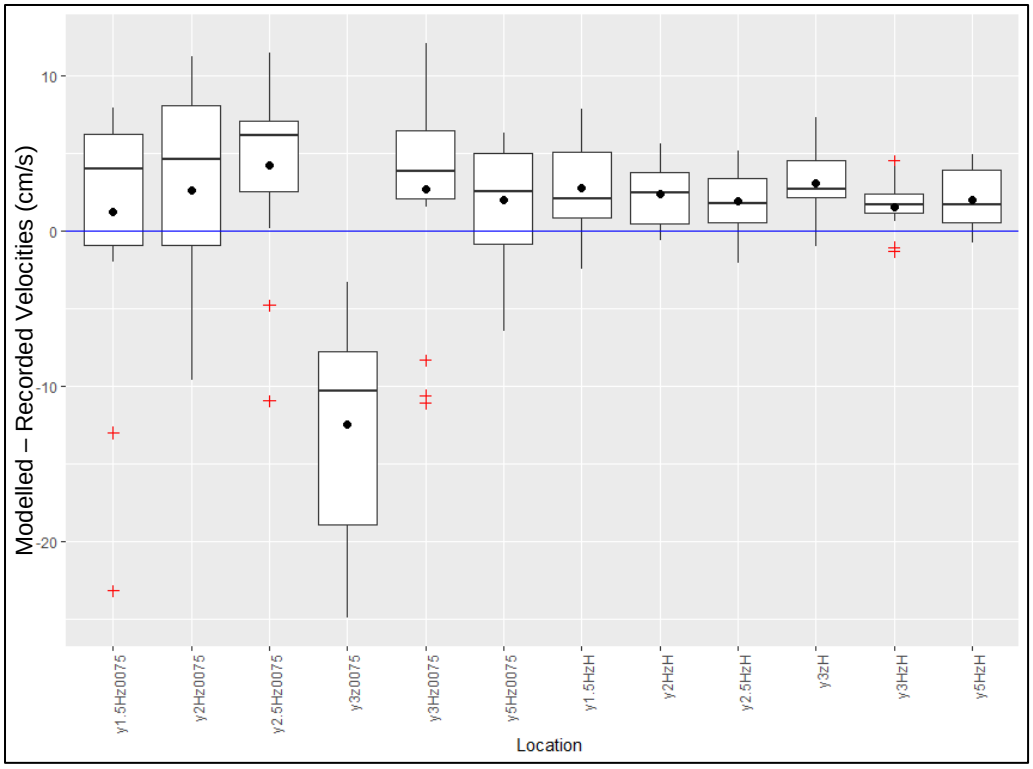

Figure 4.3 : Difference between modelled and recorded velocities for various locations downstream of the spoiler baffles, at the extremity of the spoiler Baffles (x=W/2)

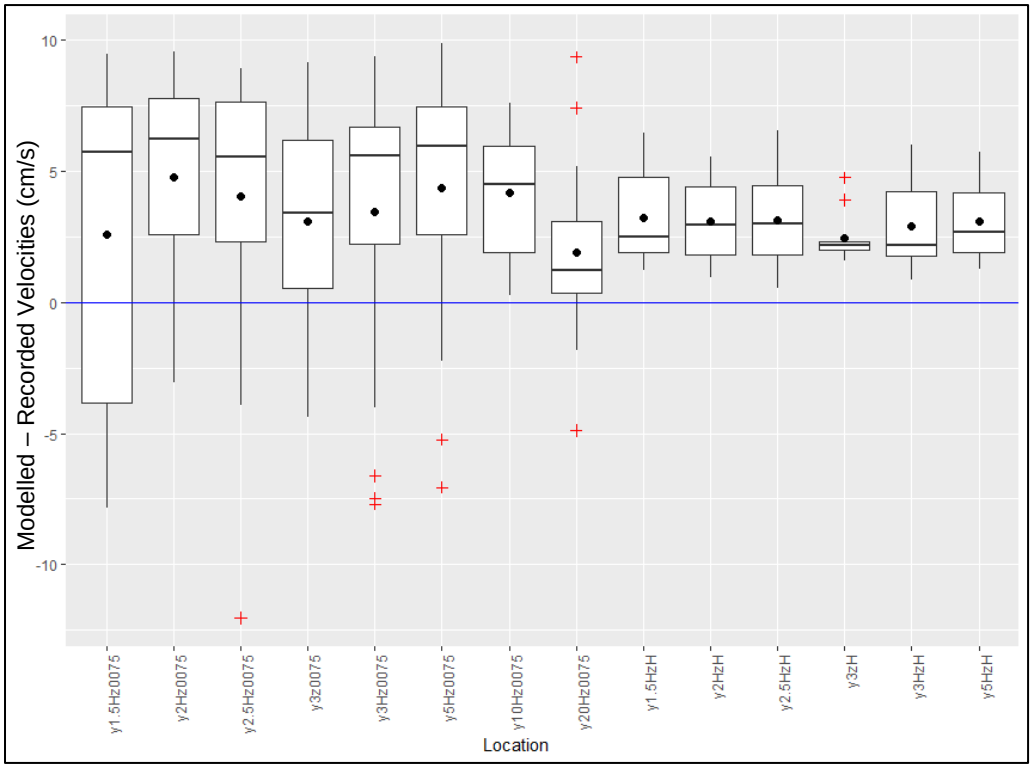

Figure 4.4 : Difference between modelled and recorded velocities for various location downstream of the spoiler baffles, near the spoiler baffles (x=3W/2)

Further analysis of the figures shows that the model tends to overestimate free-flow velocities and to underestimate velocities within the RVZ and wake region. It is also possible to note, using charts provided in Appendix 1, that these overestimations are more significant for smaller spoiler baffles. For spoiler baffles with a height of 40 mm, velocities are generally closer to the recorded average velocity than they are for spoiler baffles with a height of 20 mm and 30 mm; for which more underestimations are observed.

Most outliers observed in Figure 4.2, Figure 4.3 and Figure 4.4 relate to the modelling of the RVZ and spoiler baffler's wake. The Smagorinsky model seems to overestimate slightly the width and height of the RVZ. It however seems to underestimate the length of the RVZ, with velocities recorded in Figure 4.2 at location y3z0075 being consistently lower than every other point within the RVZ, and grossly overestimated by the model. Another explanation for outliers lies in the methodology for positioning the ADV. There could have been small variations in the exact placement of the device, leading to velocities being recorded in a slightly different position; when close to the RVZ location, a slight difference in positioning will lead to significantly different records.

One location showed an impressive amount of variation, namely x0.5Wy2Hz0075 located upstream of the spoiler baffle. For the spoiler baffles with a height of 20 mm specifically, the recorded dataset shows a sudden decrease in velocity upstream of the spoiler baffle under both HCs. This sudden decrease in velocity is less significant as the width of the spoiler baffle increases, is not observed for spoiler baffles with a height of 30 mm and 40 mm and was not modelled by the Smagorinsky model.

4.1.2 Modelling of Flow Separation

For all models, fragments of a Ω-shaped vortex ring can be observed close to the floor of the canal. Their impact is more significant for wider spoiler baffles and seem especially important for H40W40, as shown in Figure 4.5.

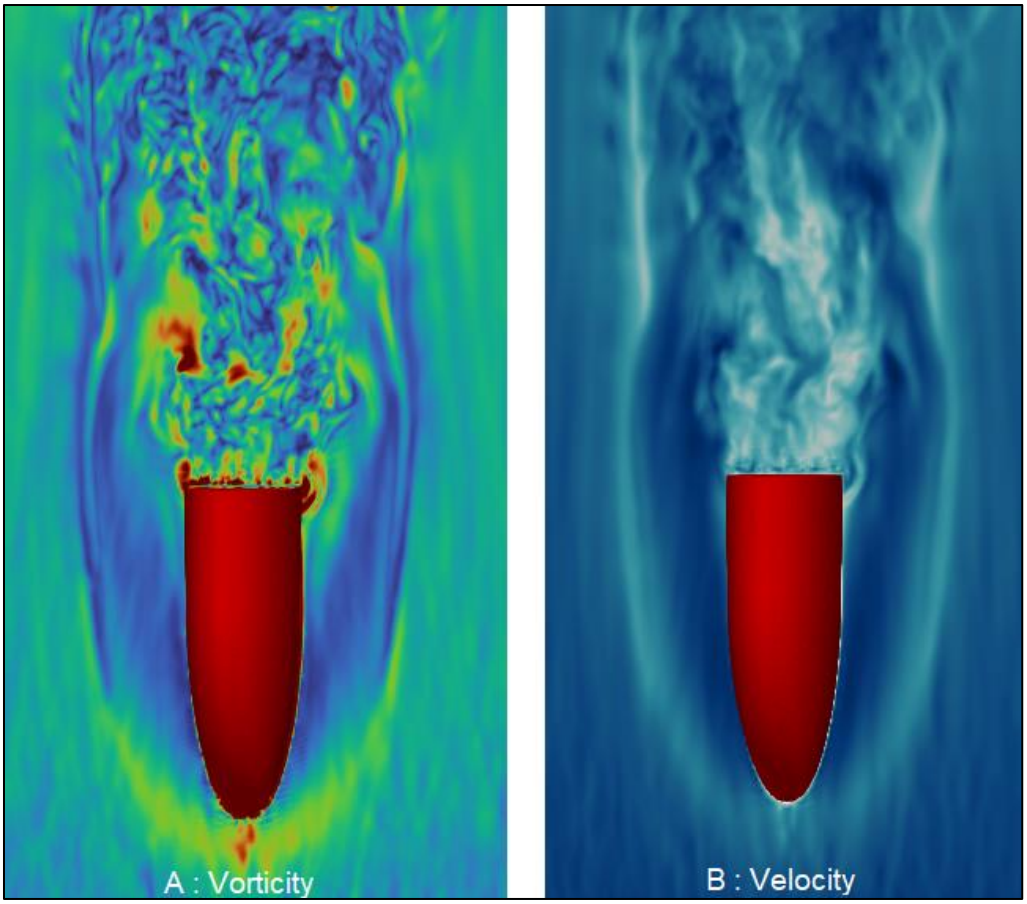

Figure 4.5 : Evidence of a Ω-shaped vortex ring fragment attached to the body of the spoiler baffle; Simulation h40w40_01 | z = 3 mm

4.1.3 Physical Against Modelled Length of RVZs and Confined Turbulent Wake Region

Using recorded videos of the ink experiment, a rough estimate of the length of the RVZ was measured (Figure 4.6). The differences between the height and width of the recorded and modelled RVZs was not deemed significant enough to warrant extensive comparisons, as they are directly linked to the height and width of the spoiler baffle.

The average length of the physical RVZ measured from the videos is between 0.7 and 2.2 times the height of the spoiler baffle; while the average length of the modelled RVZ varies between 1.1 and 2.9 times the height of the spoiler baffle. The confined turbulent wake region is, on average, 10% shorter than the modelled RVZs measured based on flow velocities, with a length varying between 1.1 and 2.8 times the height of the spoiler baffle. Definite conclusions cannot be drawn from the comparison between the physical and modelled RVZs due to the nature of the measures from the recorded videos, which suffers significant limitations. However, it is possible to note that the same pattern of behavior is detected from one spoiler baffle to the other i.e., an

increase in the length of the RVZ following an increase in the width of the spoiler baffle. This pattern seems more marked for the physical RVZ than it is for the modelled RVZ and confined turbulent wake region.

The strong variation observed for physical RVZs of the wider spoiler baffles with a height of 30 mm and 40 mm is attributable to the more turbulent nature of the RVZs, which rendered their boundaries harder to locate. A similar challenge was faced when measuring the length of the confined turbulent wake region, for which more room is left to biases and judgment, as finding the precise location of the cut-off stream confining the turbulent wake region strongly depends on the placement of the stream tracer too and the nature of the RVZ itself i.e., more turbulent RVZs might not have a clearly defined confined turbulent wake region.

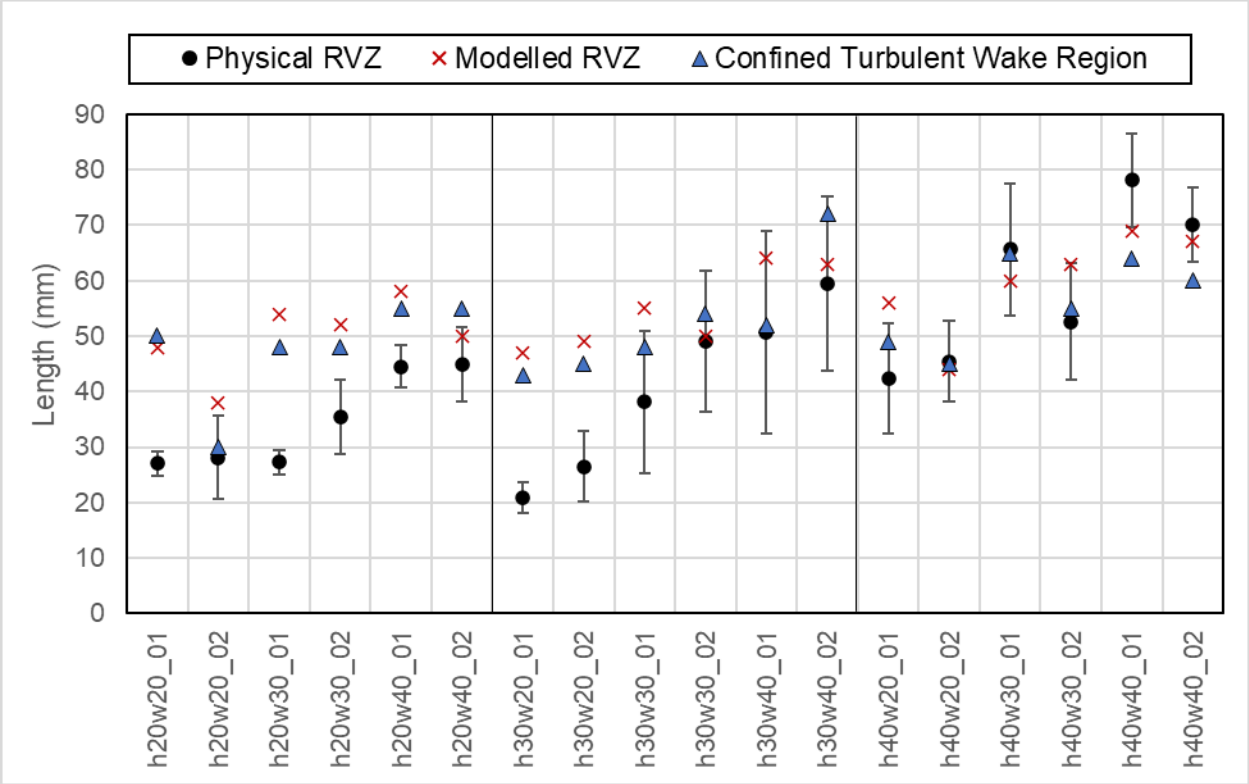

Figure 4.6 : Comparison of the measured lengths of the physical RVZs, of the modelled RVZs and of the confined turbulent wake region

4.2 Dimensions of the Wake and of the RVZ

Following the procedure listed in section 3.4.3, both the wake (W) and RVZ regions were sized in height (H), width (W) and length (L) under both hydraulic conditions (HC) tested. The level of fragmentation of the RVZs was also evaluated and all figures used for this qualitative assessment can be found in Appendix II. Results and observations are presented in Table 4.1.

Table 4.1 Measurements of the wake and RVZ regions in millimetres;
The level of fragmentation of the RVZ is color-coded as follows: green-low, yellow-moderate, red-strong.

Spoiler baffle	HC	RVZ.L	RVZ.H	RVZ.W	W.L	W.H	W.W
H20W20	#01	48	17	13	80	16	17
	#02	38	14	14	54	16	13
H20W30	#01	54	14	17	72	18	22
	#02	52	15	18	72	18	18
H20W40	#01	58	14	24	81	16	26
	#02	50	14	23	81	17	28
H30W20	#01	47	20	12	63	21	18
	#02	49	24	13	73	22	19
H30W30	#01	55	20	18	74	26	25
	#02	50	22	18	70	27	25
H30W40	#01	64	23	22	113	25	32
	#02	63	22	29	109	25	36
H40W20	#01	56	26	11	85	29	18
	#02	44	27	14	60	29	20
H40W30	#01	60	29	18	128	33	24
	#02	63	28	23	134	32	28
H40W40	#01	69	27	29	140	31	40
	#02	67	28	29	102	33	38

Various ratios were calculated from the measurements to render the variables unitless and facilitate further analysis of the data, with results presented in Table 4.2.

Table 4.2 Ratios calculated from the length, height and width of the RVZ and wake

Spoiler baffle	HC	$\frac{W.W}{SB.W}$	$\frac{W.H}{SB.H}$	$\frac{W.L}{SB.H}$	$\frac{RVZ.W}{W.W}$	$\frac{RVZ.H}{W.H}$	$\frac{RVZ.L}{W.L}$	$\frac{RVZ.W}{SB.W}$	$\frac{RVZ.H}{SB.H}$	$\frac{RVZ.L}{SB.H}$
h20w20	#01	0.85	0.81	3.99	0.78	1.04	0.60	0.66	0.84	2.40
	#02	0.63	0.82	2.71	1.13	0.83	0.71	0.71	0.68	1.92
h20w30	#01	0.74	0.88	3.61	0.79	0.79	0.75	0.58	0.69	2.70
	#02	0.61	0.88	3.58	1.00	0.83	0.72	0.61	0.73	2.59
h20w40	#01	0.65	0.80	4.07	0.92	0.86	0.71	0.60	0.69	2.88
	#02	0.71	0.83	4.03	0.82	0.85	0.62	0.58	0.70	2.49
h30w20	#01	0.92	0.71	2.08	0.65	0.92	0.75	0.60	0.66	1.57
	#02	0.93	0.74	2.44	0.72	1.06	0.67	0.67	0.79	1.63
h30w30	#01	0.83	0.86	2.46	0.72	0.78	0.74	0.60	0.67	1.82
	#02	0.83	0.91	2.33	0.74	0.82	0.71	0.62	0.74	1.66
h30w40	#01	0.79	0.84	3.78	0.69	0.90	0.56	0.55	0.76	2.13
	#02	0.90	0.83	3.62	0.81	0.90	0.58	0.73	0.75	2.11
h40w20	#01	0.91	0.73	2.13	0.62	0.90	0.66	0.56	0.66	1.40
	#02	0.99	0.72	1.49	0.70	0.96	0.75	0.69	0.69	1.11
h40w30	#01	0.81	0.83	3.20	0.72	0.87	0.47	0.59	0.72	1.49
	#02	0.92	0.80	3.34	0.83	0.88	0.47	0.77	0.71	1.58
h40w40	#01	1.00	0.77	3.49	0.73	0.89	0.49	0.73	0.68	1.71
	#02	0.94	0.82	2.55	0.77	0.87	0.66	0.72	0.71	1.68

4.2.1 Impacts of Hydraulic Conditions

The t-test of Student, which the null hypothesis (H_0) states that “the means are not statistically different”, was applied to all calculated ratios presented in Table 4.2, with results presented in Table 4.3. The only variable seemingly impacted by a change in the surrounding hydraulic condition is the width of the RVZ, which generally increases from HC#1 to HC#2, with the only

exception being H20W40. No other trend could be observed to predict the height and width of the RVZ other than they being directly related to the height and width of the spoiler baffle respectively.

Table 4.3 Average and standard deviation calculated for all ratios under the two hydraulic conditions tested, and results of Student's t-test with H_0 – The means are not statistically different

Ratio	Average HC#1	Average HC#2	Average All Simulations	Results of t-test
$\frac{W.W}{SB.W}$	0.83 ± 0.10	0.83 ± 0.14	**0.83 ± 0.12**	p-value = 0.9328 H_0 accepted
$\frac{W.H}{SB.H}$	0.80 ± 0.06	0.82 ± 0.06	**0.81 ± 0.06**	p-value = 0.6507 H_0 accepted
$\frac{W.L}{SB.H}$	3.20 ± 0.78	2.90 ± 0.80	**3.05 ± 0.78**	p-value = 0.4308 H_0 accepted
$\frac{RVZ.W}{SB.W}$	**0.61 ± 0.05**	**0.68 ± 0.06**	0.64 ± 0.07	p-value = 0.0214 H_0 rejected
$\frac{RVZ.H}{SB.H}$	0.71 ± 0.06	0.72 ± 0.03	**0.71 ± 0.05**	p-value = 0.5789 H_0 accepted
$\frac{RVZ.L}{SB.H}$	2.01 ± 0.54	1.86 ± 0.03	**1.94 ± 0.50**	p-value = 0.5441 H_0 accepted
$\frac{RVZ.W}{W.W}$	0.73 ± 0.09	0.84 ± 0.14	**0.79 ± 0.13**	p-value = 0.093 H_0 accepted
$\frac{RVZ.H}{W.H}$	0.88 ± 0.08	0.89 ± 0.08	**0.89 ± 0.08**	p-value = 0.9023 H_0 accepted
$\frac{RVZ.L}{W.L}$	0.64 ± 0.11	0.65 ± 0.09	**0.65 ± 0.10**	p-value = 0.7089 H_0 accepted

4.2.2 Length of the RVZ

As shown in Table 4.3, the ratio of length of the RVZ to the height of the spoiler baffle (RVZ.L/SB.H) varies significantly between simulations, namely from 1.1 to 2.9, with an average of 2.01 for HC#1 and of 1.86 for HC #2, with no statistical difference between both sets. Further analysis showed a trend in the data. RVZ.L/SB.H can be predicted by two variables, namely by

the ratio of the spoiler baffle's width to its height (SB.W/SB.H) and by the submergence level of the spoiler baffle defined as the ratio of the water depth to the height of the spoiler baffle (W.D/SP.H), as shown in Figure 4.7.

Increasing the width of the spoiler baffle generally results in an increase of the RVZ length, with the only exception being the spoiler baffle with a height of 20 mm under HC #2. This discrepancy can however be explained by where the measurements for the RVZ sizing fell following the methodology outlined in section 3.4.3.1. It could be argued that the RVZ generated by h20w40_02 is also lengthier than h20w30_02.

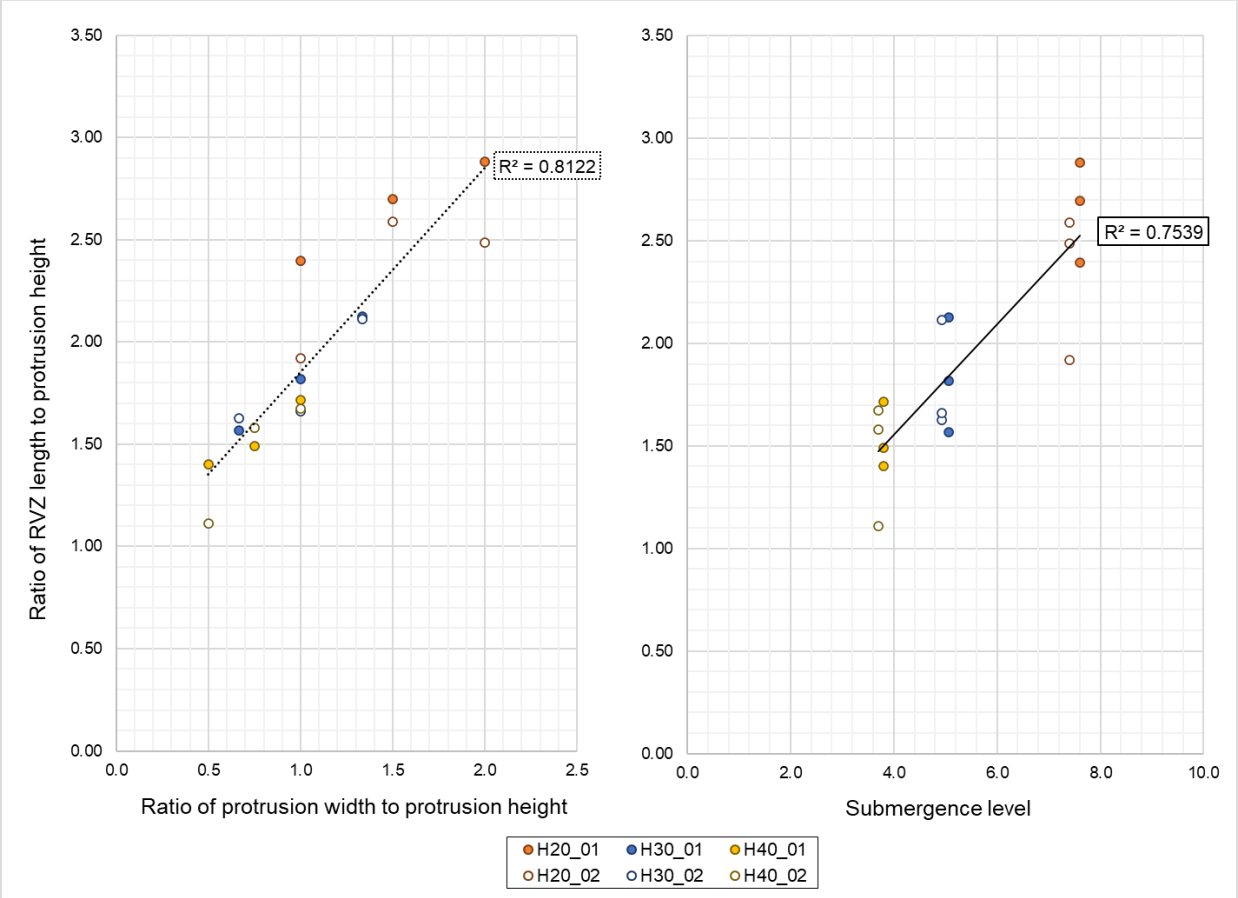

Figure 4.7 Ratio of the length of the RVZ to the height of the spoiler baffle as a function of the ratio of the width of the spoiler baffle to the height of the spoiler baffle and of the submergence level under hydraulic condition #1 (dashed line) and #2 (solid line)

A multivariant model was developed, given in Equation 4.1 and presented graphically in Figure 4.8. Applying the test of Student, which H_0 states that "the variable is statistically null", showed that both variables are statistically significant, with a p-value of 6.9×10^{-5} obtained for SB.W/SB.H and of 7.0×10^{-4} for the submergence level (W.D/SB.H). The model is based on the hypothesis

that changes in flow velocity and turbulence level between HC #1 and HC#2 are inferred by the submergence level.

$$\frac{RVZ.L}{SB.H} = 0.6574\frac{SB.W}{SB.H} + 0.1410\frac{W.D}{SB.H} + 0.4596 \qquad \begin{bmatrix} \frac{SB.W}{SB.H} \in [0.5, 2.0] \\ \frac{W.D}{SB.H} \in [3.7, 7.6] \end{bmatrix}$$

Equation 4.1 Model to predict the ratio of the length of the RVZ to the height of the spoiler baffle

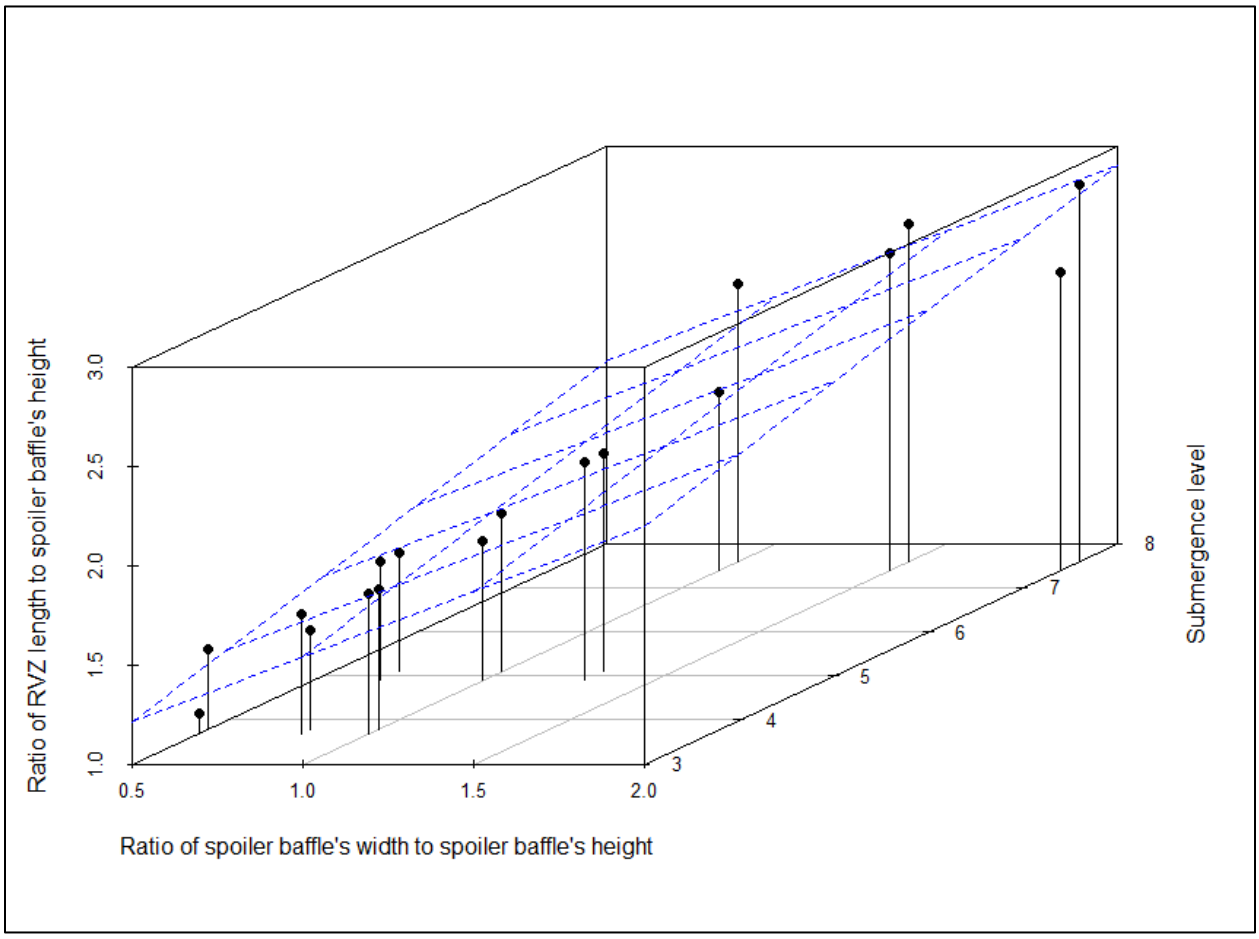

Figure 4.8 : 3D presentation of the prediction model for RVZ.L/SB.H from SB.W/SB.H and from the submergence level (R^2_a = 0.9052)

4.2.3 Fragmentation Level of the RVZ

The fragmentation level of the RVZs increases with the width and height of the spoiler baffles i.e., a higher volume of higher velocities envelopes is modeled within the RVZs for bigger spoiler baffles. The average speed within those envelopes goes well above the chosen velocity boundary

for the RVZs for HC#1 (10 cm/s) and HC#2 (0.125 cm/s). The highest modeled velocity within an envelope is 30 cm/s, obtained for h40w40_02.

The pattern identified on the recorded velocities differs. On the recorded velocity data, shown on Figure 4.9, the maximum recorded flow velocity, at a same point within the RVZ (x = 0 m; y = 0.03 m; z = 0.0075 m), decreases as the ratio of spoiler baffle width to its height (SB.W/SB.H) increases. The only increase in the maximum recorded velocity is observed for H20_02. For all spoiler baffles, the minimum flow velocity recorded for this same location is null.

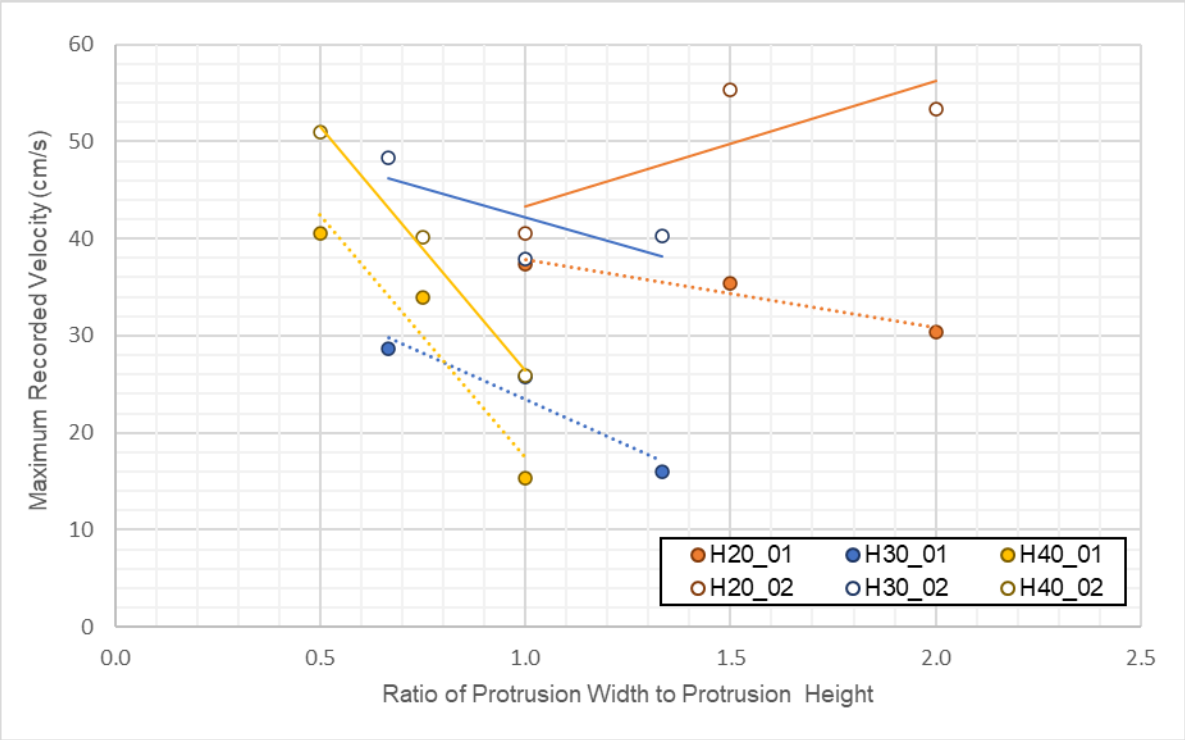

Figure 4.9 Maximum recorded velocity in function of SB.W/SB.H

4.2.4 Volume of the RVZ

As shown in Figure 4.10, significant gains are made in the overall volume of the RVZ when increasing the width of the spoiler baffle up to SB.W/SB.H = 1. Above SB.W/SB.H = 1, the gain in volume is less significant with the extra width. It can also be seen that for SB.W/SB.H > 1, the volume of the RVZ tend to increase from HC#1 to HC #2, likely due to the increase in the width of the RVZ identified in section 4.2.1.

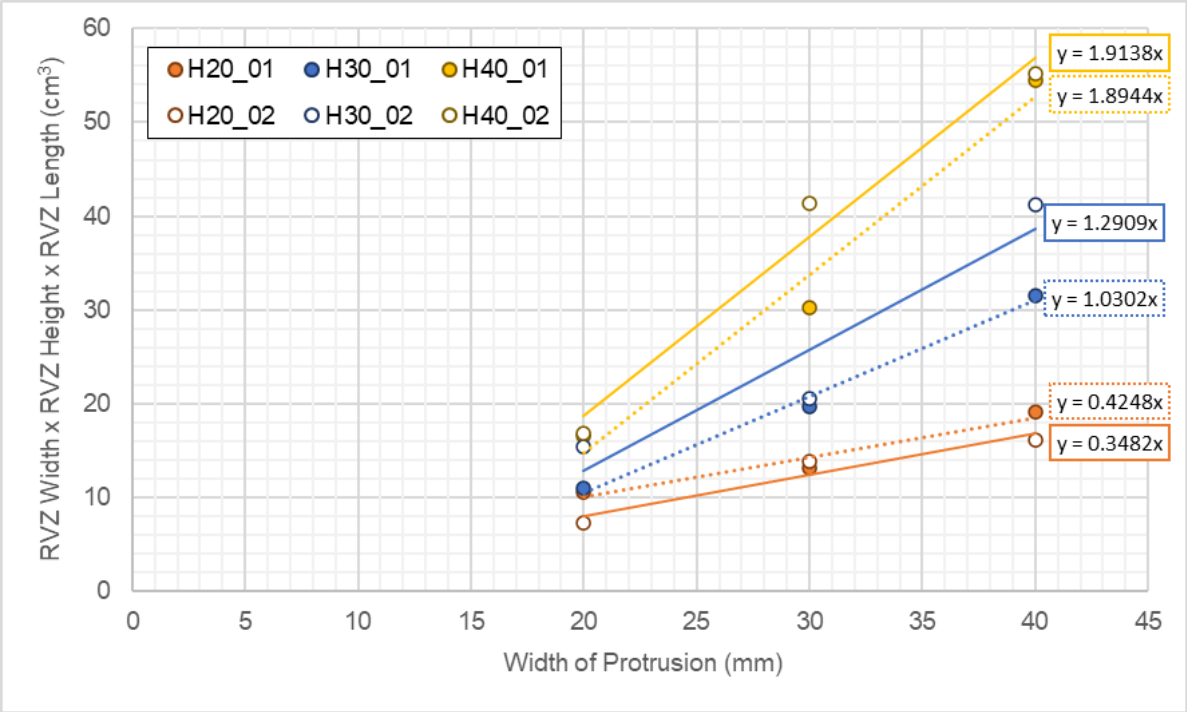

Figure 4.10 Volume of the RVZ as a function of the width of the spoiler baffle for hydraulic condition #1 (dashed line) and hydraulic condition #2 (solid line)

4.3 Vortices Within the RVZ

An analysis of the vortices modelled within the RVZ was conducted to better understand the nature of the RVZ generated by the spoiler baffles and the impact of the surrounding hydraulic conditions on it, with a summary of observations presented in Table 4.4. Note that a toroidal vortex-ring refers to a vortex spinning in the XY plan i.e., parallel to the floor of the canal; a helical vortex refers to a vortex spinning in the XZ plan i.e., parallel to the inlet/outlet of the canal; and an arch-type vortex refers to a vortex which starts in a plan and spins along a reversed "J" line toward another plan. A total of three general arrangements was observed:

Type A. A small chain of vortices is identified along the downstream face of the spoiler baffle. It evolves into a number of small toroidal vortex-rings, observed in the bottom section of the RVZ. In one case, the vortex-rings seem to constitute a set of mothers and daughters' rings; in others, only one or two rings are observed that give lieu to a chain of vortices transiting along the volume of the RVZ and seemingly evolving randomly across all plans. The RVZ is closed by helical vortices, usually two, but sometimes more (Figure 4.11).

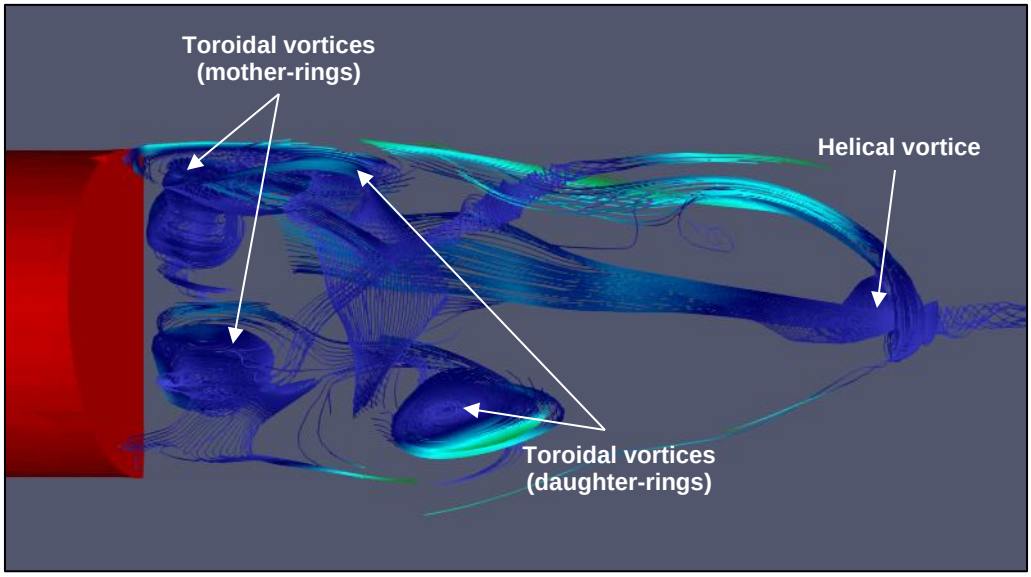

Figure 4.11 : Type A Vortices arrangement, taken from h20w20_01 (top view)

Type B. A small chain of vortices is identified along the downstream face of the spoiler baffle. In lieu of toroidal rings, the RVZ is dominated by arch-type vortices. In one case, two counter-rotating arc-type vortices are observed, linked together and forming one big arch-type vortex. The RVZ is closed by helical vortices (Figure 4.12).

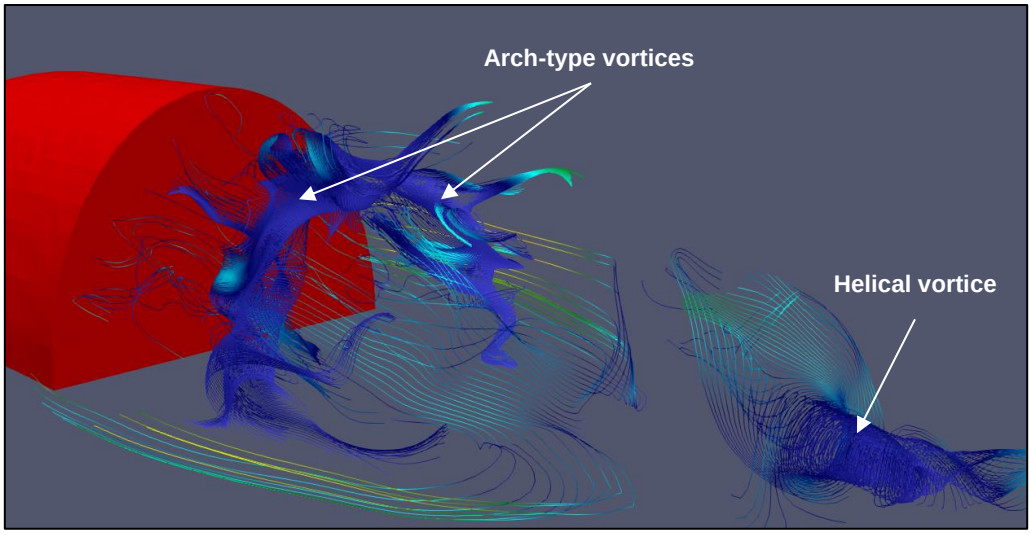

Figure 4.12 : Type B Vortices arrangement, taken from h20w30_02 (angled, side view)

Type C. Arrangement C shows a highly disorganized RVZ, with no toroidal rings, nor arch-type vortices observed in the bottom section of the RVZ. A chain of vortices randomly evolving across all plans is observed, from the downstream face of the spoiler baffle to the end of the RVZ, which is closed by helical vortices. The main feature of this type is the presence of a main vortex, seemingly stable and spinning in the YZ plan (Figure 4.13).

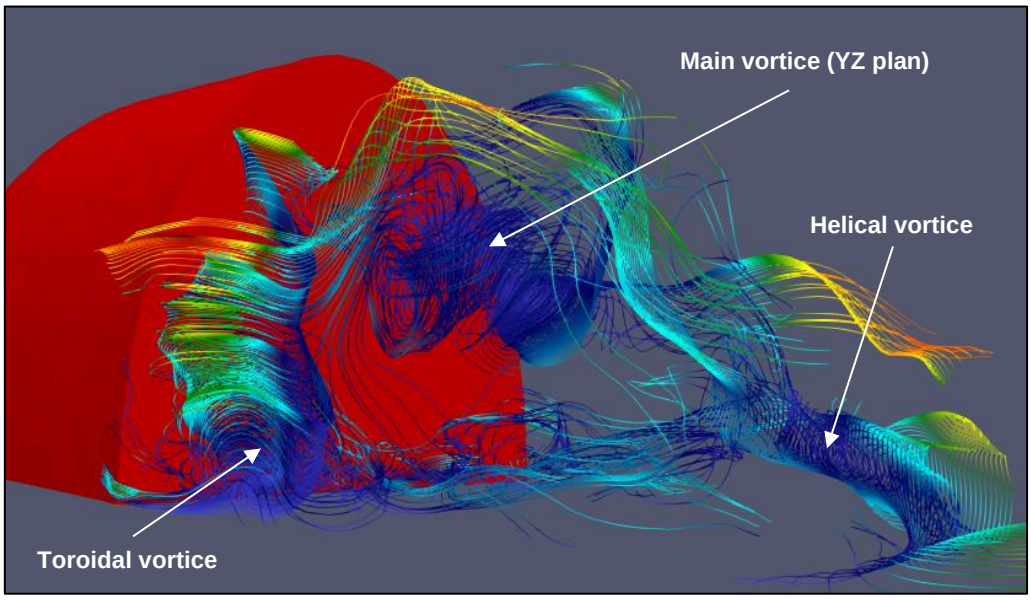

Figure 4.13 : Type C Vortices arrangement, taken from h30w30_02 (angled, side view)

The most common arrangement observed is “Type C”, which occurs in 61% of all cases, followed by “Type B” (33%) and “Type A” (6%). Note that in all cases, the overall shape of the RVZ mirrors the shape of the spoiler baffle.

In Table 4.4, a special attention was given to the presence or absence of a vortex spinning in the YZ plan because this vortex seems more stable in nature and could be construed as the main eddy of the RVZ, particularly for Type C.

The presence or absence of a stable Kármán vortex street was not linked to any specific arrangement but rather seems to depend on the width of the spoiler baffle and surrounding hydraulic conditions. The smaller spoiler baffle’s width of 20 mm is the only one associated with the generation of a stable Kármán vortex street. More turbulent hydraulic conditions seem to diffuse the Kármán vortex street, reducing its length. Note that the only spoiler baffle which wake touches the walls of the canal is H40W40; the proximity of the walls of the canal is therefore not what is keeping the formation of a stable Kármán vortex street for wider spoiler baffles.

Table 4.4 Summary of vortices and their arrangement observed within the RVZ for each simulation (angles are estimated)

Name	HC	Type	Length of Kármán vortex	Middle point of main YZ vortex	Comments
H20W20	#1	A	215 mm	-	Two pairs of mother-daughter toroidal vortex rings
	#2	B	170 mm	y = 10 mm; z = 10 mm	Two counter-rotating arch-type vortices, one evolving toward the YZ plan
H20W30	#1	B	-	y = 18.5 mm; z = 14 mm	Two counter-rotating arch-type vortices, one evolving toward the YZ plan
	#2	B	-	y = 10 mm; z = 14 mm	Two counter-rotating arch-type vortices, both linked together in the YZ plan
H20W40	#1	C	-	y = 9 mm; z = 14 mm	YZ vortex is angled (10° from x-axis), on right side of RVZ
	#2	C	-	y = 29 mm; z = 13 mm	YZ vortex is parallel to x-axis, on right side of RVZ
H30W20	#1	C	155 mm	y = 19 mm z = 23.5 mm	Pair of toroidal rings evolving into a chain of vortices.
	#2	C	-	y = 16 mm; z = 17 mm	YZ vortex is parallel to x-axis, on right side of RVZ
H30W30	#1	C	-	y = 20 mm; z = 18 mm	YZ vortex is angled (15° from x-axis), across the width of RVZ
	#2	C	-	y = 20 mm; z = 18 mm	YZ vortex is parallel to x-axis, across the width of RVZ
H30W40	#1	C	-	y = 13 mm; z = 13 mm	YZ vortex is parallel to x-axis, toward the middle of RVZ
	#2	B	-	y = 26 mm; z = 21 mm	Two counter-rotating arch-type vortices, one evolving toward the YZ plan
H40W20	#1	C	120 mm	y = 16 mm; z = 25 mm	YZ vortex is angled (45° from x-axis), toward the middle of RVZ
	#2	C	100 mm	y = 11 mm; z = 17 mm	YZ vortex is angled (20° from x-axis), toward the middle of RVZ
H40W30	#1	C	-	y = 15 mm; z = 27 mm	YZ vortex parallel to x-axis, toward the middle of RVZ
	#2	C	-	y = 21 mm; z = 28 mm	YZ vortex is angled (30° from x-axis), toward the middle of RVZ
H40W40	#1	B	-	y = 20 mm; z = 30 mm	One arch-type vortex evolving toward the YZ plan followed by helical vortices
	#2	B	-	y = 19 mm; z = 24 mm	One arch-type vortex evolving toward the YZ plan followed by helical vortices

4.4 Predicted Body Length of Fish Able to Use the RVZ

The ratio provided by Lindberg et al. (2016) i.e., a RVZ exceeding two-third of the fish body length, was used to calculate minimum body length of fish that would theoretically be able to use the RVZ generated by the designed spoiler baffles without confusion. Observations from Cotel and Webb (2015), whom stated that problems appeared when eddy diameter was the same as the fish body length, were also used for those calculations, with results presented in Table 4.5.

Table 4.5 Minimum fish length able to use the RVZ created by the spoiler baffles

Simulation	HC	Minimum Fish Length (cm)	
		(Lindberg et al., 2016)	(Cotel and Webb, 2015)
H20W20	#01	3.2	4.8
	#02	2.6	3.8
H20W30	#01	3.6	5.4
	#02	3.5	5.2
H20W40	#01	3.8	5.8
	#02	3.3	5.0
H30W20	#01	3.1	4.7
	#02	3.3	4.9
H30W30	#01	3.6	5.5
	#02	3.3	5.0
H30W40	#01	4.3	6.4
	#02	4.2	6.3
H40W20	#01	3.7	5.6
	#02	3.0	4.4
H40W30	#01	4.0	6.0
	#02	4.2	6.3
H40W40	#01	4.6	6.9
	#02	4.5	6.7

The most conservative results, namely those obtained using a ratio of two-thirds the fish body length, were charted in Figure 4.14. While a slight increase in the minimum fish length is observed from H20 to H40, there is a strong overlap between the data. Considering the precision of results, it seems spoiler baffles with a height of 30 mm and a varying width can achieve the same level of sheltering than spoiler baffles with a height of 20 mm and 40 mm.

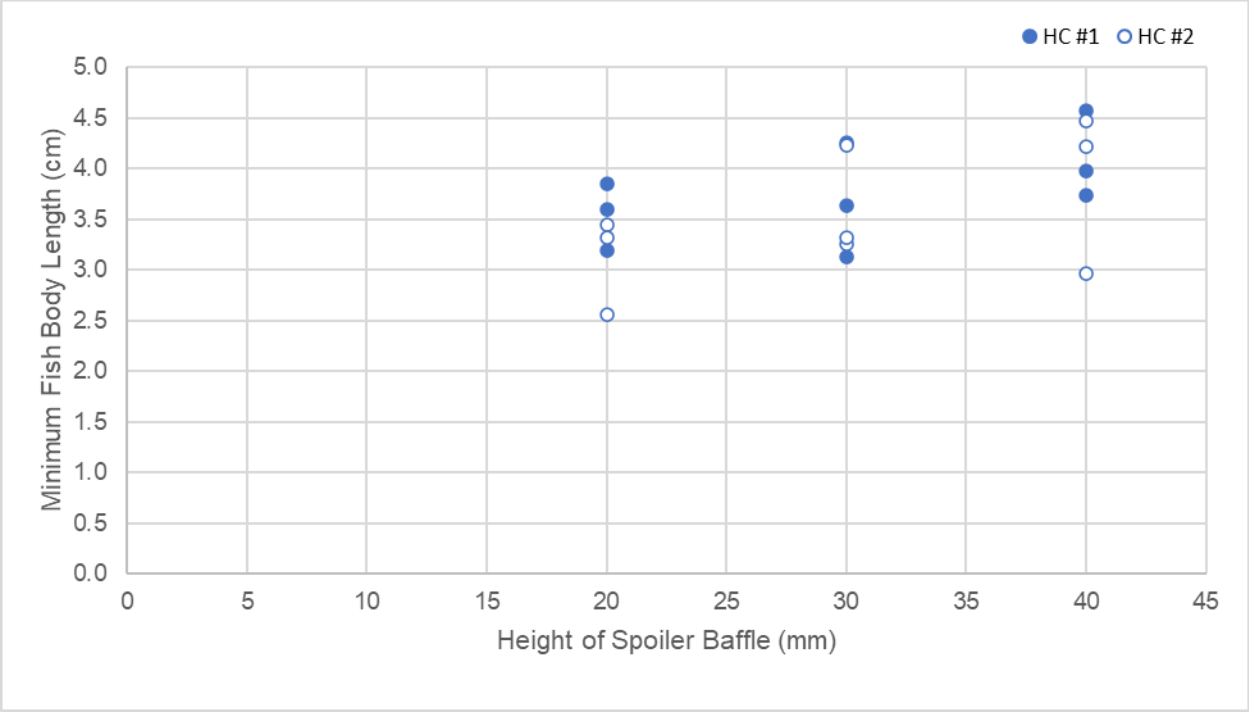

Figure 4.14 : Minimum fish length able to use the RVZ created by the spoiler baffles in function of the spoiler baffle height

5 DISCUSSION

CFD modelling holds great potential in supporting fish specialists in the design of systems aiming to facilitate fish movements and migration upstream of strong currents. The completion of the current work showed CFD modelling takes a considerable amount of time to learn, particularly if using OpenFOAM. OpenFOAM does not have a user-friendly interface like other commercial CFD software, such as Flow-3D or Ansys. However, its use was found incredibly useful in truly understanding the calculations and programs running in the background of CFD modelling work. For research particularly, its open-source operating system proved an incredible asset in avoiding the black-box phenomenon. When just starting in CFD modelling, the Smagorinsky model has the net advantage, over other models, to be simple of use. It runs smoothly, and can model the complex flow patterns associated with an object opposing the current. Its simplicity, as well as evidences from other researchers that this model could accurately reproduce turbulence (Chorda et al., 2019) is what made it the go-to model for the current research work.

5.1 The Smagorinsky Model

Generally, the Smagorinsky model both underestimated velocities within the RVZ, and overestimated free-flow velocities. Due to the absence of velocity measurements closer to the center depth of the canal, it is impossible to know how the model behaves in this region and above. Considering the available data and simulations results, modelled velocities in this region would however be expected to be above observed velocities.

Fröhlich and Rodi (2002) pointed out that an infinite amount of velocity field is compatible with one mean velocity and Pakzad (2017) observed the Smagorinsky model tends to underestimate velocities in the near-wall region. Because of the use of the solver pimpleFoam, the average flow velocity within the canal is set and will remain constant over the simulation; therefore, lower modeled near-wall velocities will automatically lead to an overcompensation of velocities elsewhere in the canal. In the context of fish performance, the overestimation of the free-flow velocities and underestimation of the velocities within the RVZ could be considered conservative assumptions. It is therefore concluded that the Smagorinsky model can be use to support the design of spoiler baffles.

An interesting observation is that the overestimation of the velocities decreases significantly for bigger spoiler baffles, particularly those with a height of 40 mm. Those spoiler baffles are both higher and lengthier than the others; they use up more volume, and the flow

separation starts closer to the inlet of the canal than for other spoiler baffles. This leads to a slight acceleration of the water velocity surrounding them, as the pump system maintains the same flow rate within the canal. It also leads to more significant “low-velocity trailing” on both sides of the RVZ.

It is proposed here that this slight increase in the velocity differential between the walls and the middle of the canal, without allowing the model to adjust its water-depth, forces an increase in the rate at which the near-wall velocities rise, rendering the overall results more accurate. It is therefore hypothesized that the accuracy of the Smagorinsky model, when modeled using a one-phase solver, might improve for conditions with higher degree of flow separation and level of turbulence, such as would be expected for a system of multiple spoiler baffles installed within a culvert or canal. On the other end, it also indicates that the use of a one-phase solver instead of a two-phases solver, which would allow modelling of the water-air interface, might lead to a reduction in the ability of the model to accurately reproduce recorded velocities.

5.1.1 Limitations of the Smagorinsky Model

The practicability of use of the Smagorinsky model for academic purpose was confirmed, but the usefulness of this model within the private sector is questionable. As a Large-Eddy Simulation (LES) model, the Smagorinsky model requires considerable computing power to run, and the memory space required to record the results can seem extreme, as accurate results will require the use of very fine meshes. Simply put, it requires the use of a supercomputer, which many consulting firms don’t have.

Additionally, when using the Smagorinsky model within OpenFOAM, the user cannot easily calibrate the coefficients used in the Van Driest Damping function. This is a major limit when working on obtaining more accurate results. While the user could hypothetically code his own version of the Van Driest Damping function to allow calibration of those coefficients, this defeats the purpose of using the Smagorinsky model, which is mostly recommended for its simplicity of use.

5.1.2 Alternatives to the Smagorinsky model

CFD modelling is a somewhat new technology undergoing rapid evolution and many new numerical strategies were developped to link the Wall-Resolved and Wall-Modeled LES approaches, resulting in increased model accuracy while maintaining practical computational demand (De Vanna et al., 2021). Detached Eddy Simulations (DES) and Improved Delayed

Detached Eddy Simulations (IDDES) are hybrid RANS/LES models. They explicitely switch from RANS to LES depending on the local size of the mesh and the turbulent length scale (Gritskevich et al., 2013) via the use of the Spalart-Allamaras eddy viscosity model. The Spalart-Allmaras model is commonly used within RANS, but by modifying the length scale in the destruction term of the equation, the eddy viscosity near the wall can cross over to a LES (Nicoud et al., 2001).

The main challenge with those models is that convergence is harder to achieve, as it requires precise and carefully crafted computational grids. Piomelli (2008) notes that DES and IDDES are most effective in modelling turbulence in area of instability, as is observed in the context of flow separation. Their use could potentially decrease the computational cost significantly, with possibly no loss of accuracy.

5.2 Sizing of the Wake of the Spoiler Baffles

The wake of an object is commonly defined as the layer over which the flow reverts back to the background velocity. While the “wake length” was measured, the actual wake generated by the spoiler baffles all extend, in length, to the end of the computational mesh. Using the chosen limits allowed the measure of the length of the wake immediately behind the object without including its tail. Thus, the wake, as defined by the protocol of section 3.4.2, is in actuality a measure of the primary wake, including its shear layers, while the measure of the RVZ does not include the shear layers.

It could be argued that the wake extends over the chosen limits, both in height and width. However, using the exact same easily recognizable limits decreased the risk of confirmation bias in areas where the actual limit was less clear, while still allowing the detection of signals and patterns. The actual loss in the measurement of width and height of the wake remains under 2 mm approximately.

5.3 Characteristics of the RVZs

Considering the frame of the current master’s thesis, and with the data available, the analysis was constrained to an overview of the near-wake, up to the presence/absence of a Kármán vortex street downstream of the spoiler baffles. The near-wake, or primary wake of the spoiler baffle is what was identified as the RVZ, a region where the fish could potentially rest during upstream movements and migration.

It is believed that the Smagorinsky model mostly replicates what was observed on videos, and current observations seem to agree with literature. Based on the work from Fan and Tsuchiya (1990), the wakes generated by the spoiler baffles correspond to the category of arrangement #5 for three-dimensional objects (section 2.1.3), namely a pair of streamwise line vortices trailing from a horse-shoe (Ω)-shaped vortex ring fragment attached to the body.

5.3.1 Arrangement of Vortices Within the RVZ

The generation of turbulent structures within the wake of an object is a complex phenomenon. Here, an attempt is made to better understand the configuration of vortices within the RVZs of the spoiler baffles by further dividing the RVZ into three regions, previously identified by researchers.

The configuration of vortices contained within the first region of the RVZ, closest to the spoiler baffle, is the same for all spoiler baffles and can be described as a small chain of vortices evolving randomly across all plans. This region is equivalent to what Coppus (1977) refers to as a “quiet zone directly behind the rear surface of an object”. This quiet zone has been shown to hold up to 10% of the total volume of a RVZ, which is consistent with what was observed through all simulations.

The second region of the RVZ constitutes the confined turbulent wake region and the configuration of vortices within it changes across simulations. The observed configurations vary between (Type A) toroidal rings evolving within the bottom part of the RVZ, interpreted as pairs of mother-daughter vortex rings; (Type B) arch-type vortices, starting within the XY plan and moving toward the YZ plan and XZ plan; and (Type C) a chain of vortices evolving across all plans, with one main and seemingly stable vortex spinning in the YZ plan.

While no trend could be captured from the current analysis, based on literature review, this change in configuration is likely tied to (1) the changing ratio of the spoiler baffle height to the spoiler baffle width; (2) the proximity of the walls of the canal for bigger spoiler baffles; and (3) the submergence level of the spoiler baffles. The configuration would also be expected to evolve over time, as the vortices connect and disconnect from one another. This region is understood as being where the buildup of vorticity and energy takes place.

The third region of the RVZ seems to play an important role in the shedding of vortices, which happens for all types and was attributed to the presence of helical vortices closing the RVZs, most often present to the count of two. A parallel can be drawn between this third region and the shedding vortical wake region (Fan and Tsuchiya, 1990).

5.3.1.1 How Vortices Within a RVZ Might Impact Fish

While it was impossible, within the current scope, to match the analysis of vortices with the behavior of fish around the spoiler baffles, it is strongly believed that not all RVZ are created equal. It is expected that fish would respond differently to a RVZ depending on the nature of the vortices created within it. Based on the information collected, some hypotheses were developed that could be further tested by modelling at least one of the systems of spoiler baffles that was physically tested with fish within the canal over a period of time. This work could provide useful insights for the design of the spoiler baffles.

It is expected that Type A would be associated to fish positioning themselves further downstream of the RVZ, more precisely within the Kármán vortex street generated with this type. In actuality, any time a Kármán vortex street is present, fish would likely prefer positioning themselves within it, as they are capable of Kármán gaiting, an ability to adapt their swimming behavior to a vortex street, which lower the cost of swimming in free-flow condition by approximately half (Liao and Akanyey, 2017). If this behavior is verified, it could be worth considering designing spoiler baffles that lead to the creation of Kármán vortex streets under various hydraulic conditions by prioritizing spoiler baffles with a smaller ratio of spoiler baffle width to spoiler baffle height.

Type B might result in more fish confusion, as the arch-type vortices are assumed to be characterized by less stability and a stronger tendency to move around the RVZ, as they connect and disconnect from one another.

For Type C, the behavior of the fish would depend in the location of the main vortex spinning in the YZ plan. For example, if it is angled, such as was observed for various spoiler baffles, a fish would likely position itself at an angle too, adapting to the main vortex location in a way to save energy and decrease confusion.

5.3.2 Length of the RVZ

Analysing measurements of the length of the RVZ revealed that the ratio of the length of the RVZ to the height of the spoiler baffle (RVZ.L/SB.H) was strongly influenced by the shape of the spoiler baffle i.e., by the ratio of the spoiler baffle width to its height (SB.W/SB.H) and by its submergence level. For both variables, an increase is associated with an increase in the length of the RVZ. The average ratio RVZ.L/SB.H was calculated at 1.94, with a minimum of 1.11 and a maximum of 2.88.

When measuring the physical wake length, the only data available to validate the CFD models were measures taken from videos. Based on current analysis, the Smagorinsky model seems to overestimate the length of the physical RVZ. However, because of the perspective of the camera lense and highly imprecise nature of the physical measurements, it is deemed impossible, within the current scope, to precisely quantify the accuracy of the CFD models in reproducing the size of the spoiler baffle's RVZ.

What could be observed is that the pattern of behavior, from one spoiler baffle to the other, was the same for both the physical and modelled measurements. More precise measures of the length of the physical RVZs would have been useful to better validate results from the Smagorinsky model. More physical testing for lower values of submergence would also have been useful to better define the boundaries of the model developped in Equation 4.1.

Another limit lies in the intrinsic nature of LES. Data available within the current scope is limited to snapshots in time for each spoiler baffle. However, literature states the size of the vortical shedding wake region of a RVZs varies significantly over-time following a saw-tooth function (Coppus, 1977, Fan and Tsuchiya, 1990). A time-average RVZ size would be therefore preferable to more thoroughly define how the primary wake fluctuates, not only from one spoiler baffle to the other, but over time.

Overall, current findings are in agreeance with literature. Mirauda et al. (2007), who studied the impact of the submergence level of a tethered sphere on its RVZ, showed that an increase in the level of submergence of the object was associated with an increase in the size of the object's RVZ. While Shamloo et al. (2001) found the length of the recirculation region to be about twice the diameter of a hemisphere, or four times its height, Fan and Tsuchiya (1990) noted that the size of a primary-wake, or RVZ, will vary significantly over time and that it depends heavily on the shape of an object.

5.3.2.1 How the Length of the RVZ Might Impact Fish

Following what Cotel and Webb (2015) and Lindberg et al. (2016) observed, it is hypothesized that fish with a body length under two-third the length of RVZ would likely become confused and unable to exploit the spoiler baffles for shelter. In this event, a much smaller spoiler baffle than those tested would need to be used for fry fish under 3 cm.

5.3.3 Length of the Confined Turbulent Wake Region of a RVZ

In identifying and characterizing the RVZ and its potential influence on fish, it appeared that the confined turbulent wake region, due to its closed and stable nature, could have particular impacts on fish migration. The confined turbulent wake region is, in average,10% shorter than the RVZ.

The method used to identify and measure the confined turbulent wake region was found to leave significant room to biases and judgment, as the localization of the cut-off stream is strongly influenced by the placement of the stream tracer tool. In particular, the boundary of the confined turbulent wake region was found to move over the depth of the spoiler baffles. This movement may be because the downstream limit of the RVZ is profiled, matching the shape of the spoiler baffle.

5.3.4 Width and Height of the RVZ

The height of the RVZs was found to vary following the height of the spoiler baffles. The width of the RVZs was found to vary following the width the spoiler baffles, but was also impacted by the hydraulic conditions within the canal; The RVZ was wider for hydraulic condition #2 than for hydraulic condition #1.

This observation seems counter-intuitive, and it is believed that it could have been generated by the use of a somewhat coarser mesh under hydraulic condition #2. A y+ value of 13 was used for hydraulic condition #2, as opposed to a y+ value of 10 for hydraulic condition #1. This slight increase in the sizing of the mesh cells, extending on both sides of the RVZ, as opposed to just one side when measuring the height of the RVZ, might have contributed to the obtention of a statistically different average between the width measured for both conditions.

5.3.5 Level of Fragmentation of the RVZ

Results showed that for spoiler baffles with a same height, increasing the width of the spoiler baffles lead to more important level of fragmentation within the RVZ i.e., to a higher volume of velocity envelopes containing higher flow velocity. The recorded data show that increasing the spoiler baffle width is generally associated to a decrease in the maximum recorded flow velocity for a same point (x = 0; y = 0.03; z = 0.0075) mm.

Considering the law of energy conservation, if the hydraulic conditions within the canal are maintained, and for a specific average speed within a RVZ, the occurrence of larger regions of

higher flow velocity within the RVZ would hereby lead to a decrease in the maximum speed occurring within the region.

While this observation might result from the features of the spoiler baffles (SB.W/SB.H), it might also result from an intensified the wall-effect, as the extremities of the wider spoiler baffles are closer to the walls of the canal. Fan and Tsuchiya (1990) states that the wall effect was associated to a delay in vortex shedding. It is therefore believed that this delay would be associated to an increased capacity of the RVZ to absorb more energy before vorticity is shed downstream, hence the appearance of regions characterized by higher flow velocity.

5.3.5.1 How the Level of Fragmentation Might Impact Fish

Considering higher levels of fragmentation are likely the result of an increased capacity of the RVZ to absorb more energy before vorticity is being shed downstream, it is possible that an increased width might lead to a higher risk of fish being expulsed from the RVZ during vortex shedding. Fish might be able to withstand vorticity shedding associated to a smaller degree of energy, but less so when the energy buildup is more significant.

6 CONCLUSION

The work of the current thesis confirmed that the Smagorinsky model can reproduce complex turbulence patterns associated to the flow separation resulting from an object opposing the current.

However, the model tends to underestimate near-wall velocities, as well as velocities within the wake of the spoiler baffle, likely leading to an overestimation of the free-flow velocities. In the context of fish passage, velocities are particularly important in predicting fish behaviors and their capacity to migrate upstream a hydraulic structure, as it is directly linked to the time to exhaustion of fish (Lindberg et al., 2016, Wang and Chanson, 2018). The vortices and vortex-shedding phenomenon also hold great value when evaluating fish passage, as fish have been shown to adapt their swimming performance to the vortices in their path to reduce the energy cost of migration (Liao and Akanyey, 2017). The relevance of using the Smagorinsky model results as inputs for the design of the spoiler baffles was confirmed, as the overestimation of the free-flow velocities and underestimation of the velocities within the RVZ, in the context of fish passage, are conservative; if the velocities modelled are within the threshold supported by fish, then fish should be able to transit within the real system.

In terms of predicting the characteristics of the RVZ, analysis of the data showed it varies following the shape of the spoiler baffles and their level of submergence. Both the ratio of the width of the spoiler baffle to its height, and its submergence level were found to be good predictors for the length of the RVZ that a spoiler baffle creates. The surrounding hydraulic conditions, however, only statistically impacted the ratio of the width of the RVZ to the width of the spoiler baffle, with more turbulence associated to a wider RVZ for a same spoiler baffle. This statistical difference is however believed to be caused by the use of a higher y+ value for hydraulic condition #2 than for hydraulic condition #2. Note that in all cases, the shape of the RVZ mirrors the shape of the spoiler baffle.

Validating the length of the modelled RVZ proved challenging. It is intuited that the modelled wake is lengthier than the physical wake generated by the spoiler baffles, but a substantial limit of the current work laid in the impossibility to precisely measure the physical length of the RVZ. It is recommended that future similar physical experimentations include the presence of a ruler underneath the canal to note approximate measurements of the RVZ and better validate CFD modelling work.

Additionally, because of the heaviness of each simulation results, analysing how the RVZ evolves through time was not possible. However, the size of a primary wake is strongly time-dependent. Therefore, the length of the RVZ should be calculated as a time-averaged length. This could be achieved by cutting the mesh to the minimum length that would enable the capture of the RVZ and by running the model over a period of time, saving results to a small enough time-step to visualise the oscillations of the primary wake.

If current results are to be taken into account for design considerations, note that, in the end, the spoiler baffles tested lead to comparable RVZ lengths. A much smaller spoiler baffle would be needed to allow fish with a body length under 3 centimeters to use the RVZ to rest. For the spoiler baffles modelled, there is a significant overlap in the body length of fish that could potentially use the spoiler baffles as shelters without becoming confused (3 to 4.5 centimeters). Other than the length of the RVZ, the main features to consider for final design relate to the stability of the RVZ generated, namely the type of arrangement of vortices within it and its level of fragmentation. Those features will likely have a significant impact on fish and on their capacity to remain within the RVZ generated.

Three types of arrangements of vortices were observed, with Type C observed for more than half the simulations. Type C is a seemingly highly disorganized RVZ that could be described as a chain of vortices randomly evolving across all plans. However, the presence of one main vortex, seemingly stable and spinning in the YZ plan, indicates Type C might actually be the most stable of all observed arrangements.

Within the scope of the current thesis, it was impossible to link fish behavior to the modelled vortices. This master thesis was useful in defining the level of accuracy and caveats of the Smagorinsky model, and a logical next step would be to model the system of two spoiler baffles that was physically tested with fish to better understand if and how the vortices within the RVZ impact the behavior of fish around the spoiler baffles. This extra effort could also shed light on one hypothesis that aroused within the current work, namely that generating Kármán vortex streets within the canal might be preferable to the creation of stable RVZ with chaotic far wake.

For future modelling work, also note the main caveat of the Smagorinsky model is its high computational cost. A very fine mesh is required to ensure convergence of the model, namely the maintenance of a $y+$ value under 10. In the current work, a value of 13 did not result in significant loss of accuracy, indicating that for very simple models, the $y+$ value could likely be increased to save on computational cost. Even then, for what can be considered a very simple model, and despite the use of 20 physical cores, the time of simulation was significant.

This high computational cost is also what lead to the use of the *pimpleFoam* solver, which due to its one-phase nature, did not allow modelling of the free-surface of the system, but permitted to cut the simulation time considerably compared to using the *interFoam* solver. While this decision resulted in some loss of information, as the eddies created by the water-interface could not be modelled, data shows the use of *pimpleFoam* still permitted appropriate reproduction of flow velocities within the lower region of the canal and within the wake of the spoiler baffle, where the fish transit. The use of a simplified one-phase model is therefore considered an appropriate way to model eddy-dominated flows. In the case of wave-dominated systems, *interFoam* should be used.

One recommendation, however, would be to model one of the 18 spoiler baffles modelled again, this time using the IDDES model. In the event this second model provides similar results than the Smagorinsky model, it could prove useful in decreasing significantly the computational strength required for simulations, further improving the relevance of using CFD modelling in supporting the design effort of the spoiler baffles. Note that the IDDES model is also a one-phase model.

The current thesis is the only one, to our knowledge, to look this deeply into the use of the Smagorinsky model in the context of design. While the Smagorinsky model was previously used to model systems for fish passage, a thorough analysis of how it compared with observations and its main issues was not available in the context of fish. While there is still more to be done to further confirm this extensive modelling work, this work provided some useful insights in the future of hybrid modelling.

7 BIBLIOGRAPHY

Akanyey, O. and J. C. Liao (2013). "A kinematic model of Kármán gaiting in rainbow trout." The Journal of Experimental Biology **216**(24): 4666-4677.

Alfonsi, G. (2009). "Reynolds-Averaged Navier-Stokes Equations for Turbulence Modeling." Applied Mechanics Reviews **62**: 20.

Cabonce, J., R. Fernando, H. Wang and H. Chanson (2017). Using Triangular Baffles to Facilitate Upstream Fish Passage in Box Culverts: Physical Modelling. Australia, University of Queensland. **Report CH107/17**.

Cabonce, J., R. Fernando, H. Wang and H. Chanson (2018). "Using small triangular baffles to facilitate upstream fish passage in standard box culverts." Environmental Fluid Mechanic **19**(1): 157-179.

Castano, S. L., A. Petronio, G. Petris and V. Armenio (2019). "Assessment of Solution Algorithms for LES of Turbulent Flows Using OpenFOAM." Fluids **4**(171).

Castro-Santos, T. (2005). "Optimal swim speeds for traversing velocity barriers: an analysis of volitional high-speed swimming behavior of migratory fishes." The Journal of Experimental Biology **208**.

Castro-Santos, T. (2006). "Modeling the Effect of Varying Swim Speeds on Fish Passage through Velocity Barriers." Transactions of the American Fisheries Society **135**.

Chen, D. and G. H. Jirka (1995). "Experimental study of plane turbulent wakes in a shallow water layer." Fluid Dynamics Research **16**(1): 11-41.

Childress, S. (2009). An Introduction to Theoretical Fluid Dynamics. Courant Institute of Mathematical Sciences, American Mathematical Society.

Chorda, J., L. Cassan and P. Laurens (2019). "Modeling Steep-Slope Flow across Staggered Emergent Cylinders: Application to Fish Passes." Journal of Hydraulic Engineering **145**(11).

Cintolesi, C. and E. Mémin (2020). "Stochastic Modelling of Turbulent Flows for Numerical Simulations." Fluids **5**.

Cloutier, M., M. Dubé, M. Jean, J. Boivin and G. Potvin (1997). L'aménagement des ponts et des ponceaux dans le milieu forestier. M. d. R. naturelles. Bibliothèque nationale du Québec, Gouvernement du Québec.

Constantin, P.-M. (2017). Analyse du comportement spatial de l'ombre de fontaine (Salvelinus fontinalis) dans un ponceau ondulé par suivi vidéo à éclairage infrarouge. Maître ès sciences Master, Université du Québec.

Coppus, J. H. C. (1977). The structure of the wake behind spherical cap bubbles and its relation to the mass transfer mechanism. PhD Thesis 1 (Research TU/e Graduation TU/e), Technische Hogeschool Eindhoven.

Cotel, A. J. and P. W. Webb (2015). "Living in a Turbulent Worlds - A New Conceptual Framework for the Interactions of Fish and Eddies." Integrative and Comparative Biology **55**(4): 662-672.

Darghani, B. (1989). "The turbulent flow field around a circular cylinder." Experiments in Fluids **8**: 1-12.

De Vanna, F., M. Cogo, M. Bernardini, F. Picano and E. Benini (2021). A Wall-Modeled/Wall-Resolved LES Method for Turbulent Wall Flows. World Congress on Computational Mechanics (WCCM). Virtual Congress.

Ducrocq, T., L. Cassan, J. Chorda and H. Roux (2017). "Flow dans drag force around a free surface piercing cylinder for environmental applications." Environmental Fluid Mechanic **17**: 629-645.

Duguay, J. M. and R. W. J. Lacey (2015). "Effect of Fish Baffles on the Hydraulic Roughness of Slip-Lined Culverts." Journal of Hydraulic Engineering (ASCE) **141(1)**: 04014065.

Duguay, J. M., R. W. J. Lacey and T. Castro-Santos (2018). "Influence of baffles on upstream passage of brook trout and brown trout in an experimental box culvert." Canadian Journal of Fisheries and Aquatic Sciences **76**: 28-41.

Duguay, J. M., R. W. J. Lacey and J. Gaucher (2017). "A case study of a pool and weir fishway with OpenFOAM and FLOW-3D." Ecological Engineering **103**: 31-42.

Edoh, A. K. and T. P. Gallagher (2018). Characterizing discretization and filter effects on LES via DNS-assisted evaluations, Center for Turbulence Research.

Enders, E. C. and D. Boisclair (2016). "Effects of environmental fluctuations on fish metabolism: Atlantic salmon Salmo salar as a case study." Journal of Fish Biology **88**: 344-358.

Enders, E. C., D. Boisclair and A. G. Roy (2003). "The effect of turbulence on the cost of swimming for juvenile Atlantic salmon (Salmo salar)." Canadian Journal of Fisheries and Aquatic Sciences **60**(9).

Fan, L.-S. and K. Tsuchiya (1990). Bubble Wake Dynamics in Liquids and Liquid-Solid Suspensions. Massachussetts, Butterworth-Heinemann.

Fausch, K. D., C. E. Torgersen, C. V. Baxter and H. W. Li (2002). "Landscapes to Riverscapes: Bridging the Gap between Research and Conservation of Stream Fishes." BioScience **52**: 483-498.

Feng, Z., H. Qi, X. Huang, S. Liu and J. Liu (2021). Comparisons of Subgrid-Scale Models for OpenFoam Large-Eddy Simulation. Journal of Physics: Conference Series. **1802**.

Fisheries and Oceans Canada (2015). Guidelines for the design of fish passage for culverts in Nova Scotia. Maritimes Region. **Fisheris Protection Program:** 95.

Fröhlich, J. and W. Rodi (2002). Introduction to Large Eddy Simulation of Turbulent Flows. Cambridge, Cambridge University Press.

fumiya. (2016, May 4, 2019). "Smagorinsky SGS model in OpenFOAM." Retrieved March 18, 2022, from https://caefn.com/openfoam/smagorinsky-sgs-model.

Gagnon-Poiré, R. (2017). Fragmentation de l'habitat du Saumon atlantique (Salmo salar) par les ponceaux routiers et forestiers. Thèse de Maîtrise, Université du Québec.

Gibson, J. R., R. L. Haedrich and M. C. Wernerheim (2011). "Loss of Fish Habitat as a Consequence of Inappropriately Constructed Stream Crossings." Fisheries **30**(1): 10-17.

Goerig, E., N. E. Bergeron and T. Castro-Santos (2017). "Swimming behaviour and ascent paths of brook trout in a corrugated culvert." River Research and Applications **33**(9): 1463-1471.

Gritskevich, M. S., A. V. Garbaruk and F. R. Menter (2013). "Fine-Tuning of DDES and IDDES Formulations to the k-w Shear Stress Transport Model." Progress in Flight Physics **5**: 23-42.

Gullbrand, J. (2001). Explicit filtering and subgrid-scale models in turbulent channel flow, Center for Turbulence Research. **Annual Research Briefs**.

Johnson, P. L. (2020). "Energy Transfer from Large to Small Scales in Turbulence by Multi-scale Nonlinear Strain and Vorticity Interactions." APS Physics **124**(10).

Keefer, M. L., C. A. Peery, S. R. Lee, W. R. Daigle and E. L. Johnson (2011). "Behaviour of adult Pacific lamprey in near-field flow and fishway design experiments." Fishes Management and Ecology **18**: 177-189.

Leng, X. and H. Chanson (2020). "Hybrid modelling of low velocity zones in box culverts to assist fish passage: Why simple is better!" River Research and Applications **36**(9): 1765-1777.

Liao, J. C. (2007). "A review of fish swimming mechanics and behaviour in altered flows." Philosophical Transactions of the Royal Society B **362**(1487).

Liao, J. C. and O. Akanyey (2017). "Fish Swimming in a Kármán Vortex Street: Kinematics, Sensory Biology and Energetics." Marine Technology Society **51**: 48-55.

Liao, J. C., D. N. Beal, G. V. Lauder and M. S. Triantafyllou (2003). "Fish Exploiting Vortices Decrease Muscle Activity." Science **302**(5650).

Liermann, C. R., C. Nilsson, J. Robertson and R. Y. NG (2012). "Implications of Dam Obstruction for Global Freshwater Fish Diversity." BioScience **62**: 539-548.

Lindberg, D.-E., K. Leonardsson and H. Lundqvist (2016). "Path selection of Atlantic salmon (Salmo salar) migrating through a fishway." River Research and Applications **32**(4): 795-803.

Lynch, A. J., S. J. Cooke, A. M. Deines, S. D. Bower, D. B. Bunnell, I. G. Cowx, V. M. Nguyen, J. Nohner, K. Phouthavong, B. Riley, M. W. Rogers, W. W. Taylor, W. Woelmer, S.-J. Youn and T. D. Beard Jr. (2016). "The social, economic, and environmental importance of inland fish and fisheries." Environmental Reviews **24**(2): 115-121.

Mahlum, S., Y. Wiersma, D. Côté and D. Kehler (2014). "Evaluating the Barrier Assessment Technique Derived from FishXing Software and the Upstream Movement of Brook Trout through Road Culverts." Transactions of the American Fisheries Society.

Mallik, M. S. I., M. A. Hoque and M. A. Uddin (2020). "Comparative Study of Standard Smagorinsky Model and Dynamic Smagorinsky Model in Large Eddy Simulation of Turbulent Channel Flow." Journal of Scientific Research **12**(1): 39-53.

McElroy, B., A. Delonay and R. Jacobson (2012). "Optimum swimming pathways of fish spawning migrations in rivers." Ecology **93**(1).

Mignot, E. and N. Riviere (2010). "Bow-wave-live hydraulic jump and horseshop vortex around an obstacle in a supercritical open channel flow." Physics of Fluids **22**: 117-105.

Mirauda, D., S. Malavasi, M. Greco and A. V. Plantamura (2007). Kinematic analysis of the movement of a tethered sphere immersed in a free surface flow. FLUCOME. Tallahassee.

Nicoud, F., J. S. Bagget, P. Moin and W. Cabot (2001). "Large eddy simulation wall-modeling based on suboptimal control theory and linear stochastic estimation." Physics of Fluids **13**.

OpenFOAM Foundation (2020). OpenFOAM User Guide Version 8**:** 243.

Pakzad, A. (2017). "Damping Functions correct over-dissipation of the Smagorinsky Model." Mathematical Methods in the Applied Sciences **40**: 5933-5945.

Piomelli, U. (2008). "Wall-layer models for large-eddy simulations." Progress in Aerospace Sciences **44**(6): 437-446.

Pirolley, A. (2021). Protocole Petit Canal. S. Larrivee-Larouche. Québec, Institut national de la recherche scientifique.

Pirolley, A. (2023). Traitements des données ADV. S. Larrivee-Larouche, E-mail Correspondance.

Radinger, J. and C. Wolter (2014). "Patterns and predictors of fish dispersal in rivers." Fish and Fisheries **15**: 456-473.

Richmond, M. C., Z. Deng, G. R. Guensch, H. Tritico and W. H. Pearson (2007). "Mean flow and turbulence characteristics of a full-scale spiral corrugated culvert with implications for fish passage." Ecological Engineering **30**(4).

Rosenhead, L. (1953). "Vortex Systems in Wakes." Advances in Applied Mechanics **3**: 185-195.

Sadeque, F., M. Loewen and N. Rajaratnam (2009). "Shallow turbulent wakes behind bed-mounted cylinders in open channels." Journal of Hydraulic Research **47**(6): 727-743.

Schlosser, I. J. (1991). "Stream Fish Ecology : A Landscape Perspective." BioScience **41**: 704-712.

Scott-Gatty, D. S., H. Rotton, W. M. Twardek, V. Marconi, L. McRae, L. J. Baumgartner, K. Brink, J. E. Claussen, S. J. Cooke, W. Darwall, B. K. Eriksson, C. Garcia de Leaniz, Z. Hogan, J. Royte, L. G. M. Silva, M. L. Thieme, D. Tickner, J. Waldman, H. Wanningen, O. L. F. Weyl and A. Berkhuysen (2020). The Living Planet Index (LPI) for migratory freshwater fish. Technical Report. The Netherlands, World Fish Migration Foundation.

Sforza, P. M. and R. F. Mons (1969). The wall wake: flow behind an obstacle on a flat surface. CASI/AIAA Subsonic Aero-and Hydro-Dynamics Meeting. Ottawa, Canada, American Institute of Aeronautics and Astronautics. **69**.

Shamloo, H., N. Rajaratnam and C. Katopodis (2001). "Hydraulics of simple habitat structures." Journal of hydraulic Research **39**(4): 351-366.

Silva, A. T., M. C. Lucas, T. Castro-Santos, C. Katopodis, L. J. Baumgartner, J. D. Thiem, K. Aarestrup, P. S. Pompeu, G. C. O'Brien, D. C. Braun, N. J. Burnett, D. Z. Zhu, J. G. Williams and S. J. Cooke (2017). "The future of fish passage science, engineering, and practice." Fish and Fisheries **19**(2).

Taguchi, M. and J. C. Liao (2011). "Rainbow trout consume less oxygen in turbulence: the energetics of swimming behaviors at different speeds." The Journal of Experimental Biology: 1428-1436.

Torterotot, J.-B., C. Perrier, N. E. Bergeron and L. Bernatchez (2014). "Influence of Forest Road Culverts and Waterfalls on the Fine-Scale Distribution of Brook Trout Genetic Diversity in a Boreal Watershed." Transactions of the American Fisheries Society **143**(6).

U.S. Department of Agriculture (2006). FishXing : User Manual and Reference, Version 3**:** 230.

Van Driest, E. R. (1956). "On Turbulent Flow Near a Wall." Journal of the aeronautical sciences: 1007-1011.

Wang, H. and H. Chanson (2018). "Modelling upstream fish passage in standard box culverts: Interplay between turbulence, fish kinematics, and energetics." River Research and Applications **34**(3): 244-252.

Watson, J. R., H. R. Goodrich, R. L. Cramp, M. A. Gordos and C. E. Franklin (2018). "Utilising the boundary layer to help restore the connectivity of fish habitats and populations." Ecological Engineering **122**: 286-294.

Zou, G. W., S. L. Liu, W. K. Chow and Y. Gao (2006). "Large Eddy Simulation of Turbulent Flows." International Journal on Architectural Science **7**(1): 26-34.

8 APPENDIX I

In order to facilitate the comprehension of the figures contained within this appendix, the x-axis labels have been taken out. Each point along the x-axis refers to a location of measurement, going from upstream of the canal toward its downstream end.

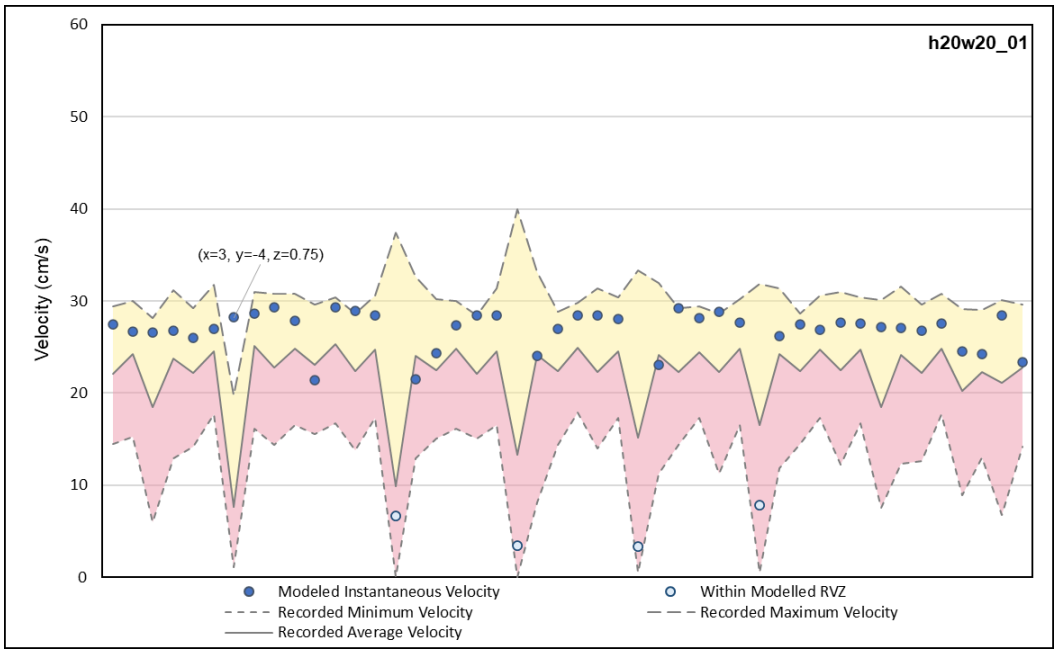

Figure 8.1 : Validation of simulation H20W20_01; the difference is observed just upstream of the spoiler baffle and is attributed to the possible inexact placement of the ADV

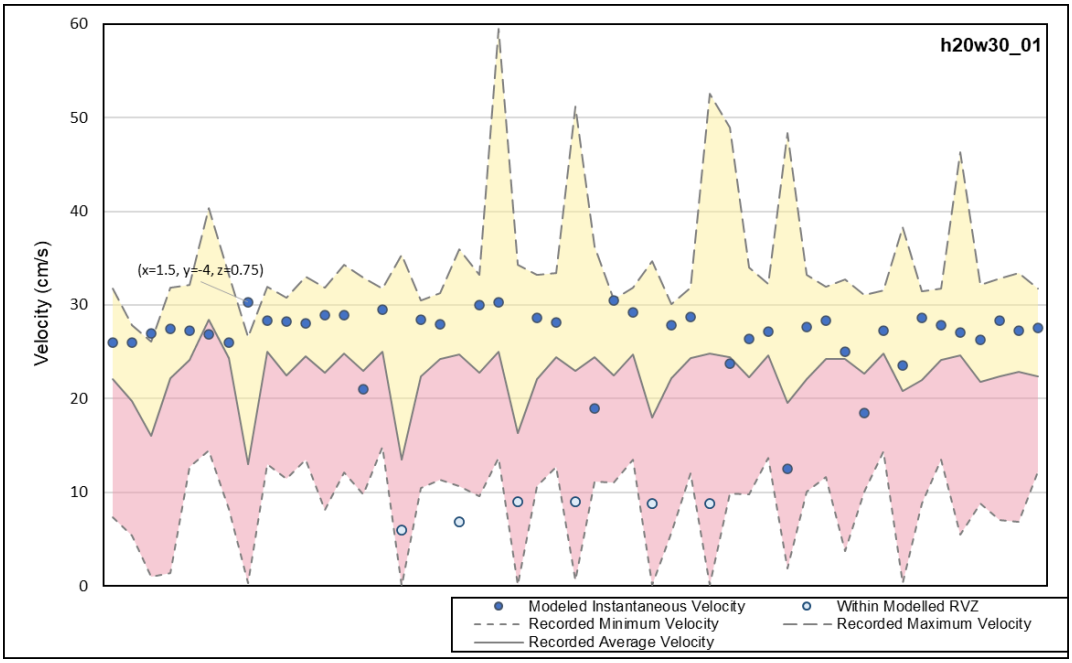

Figure 8.2 : Validation of simulation H20W30_01; the difference is observed just upstream of the spoiler baffle and is attributed to the possible inexact placement of the ADV

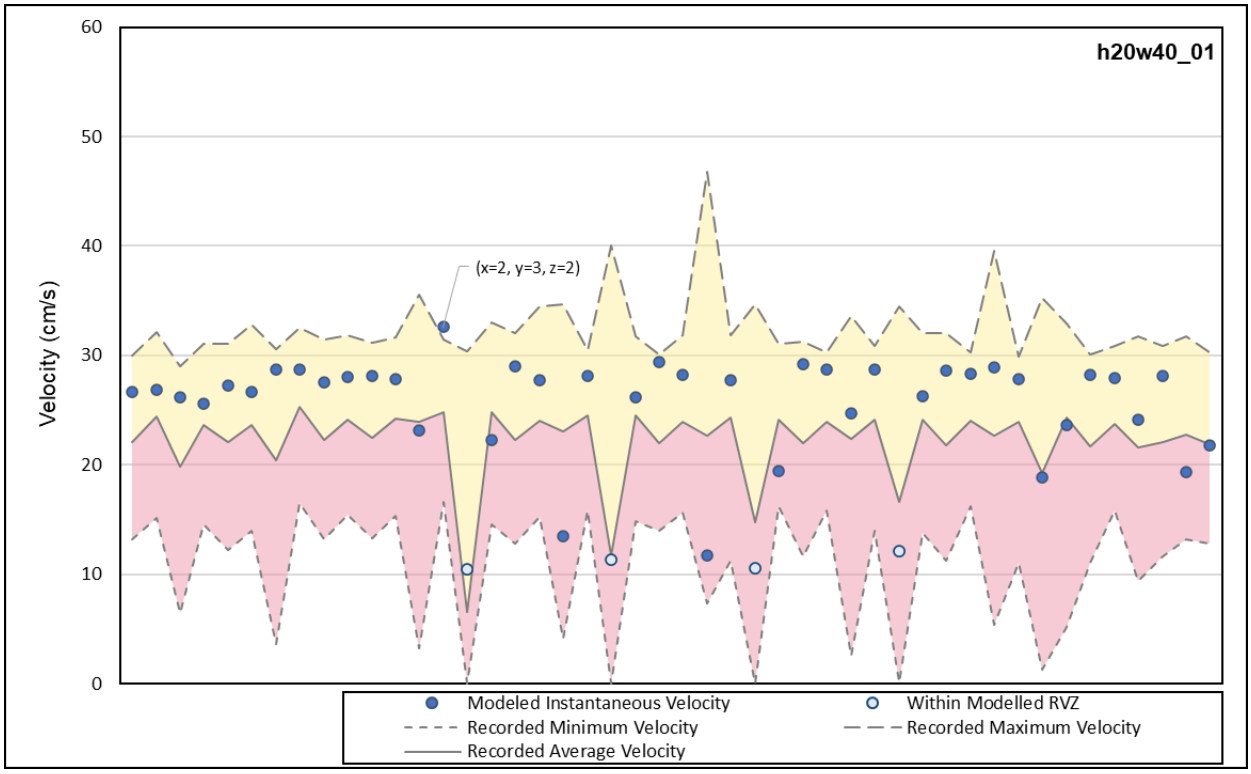

Figure 8.3 : Validation of simulation H20W40_01; the different reading is within the modelled shear layer of the wake

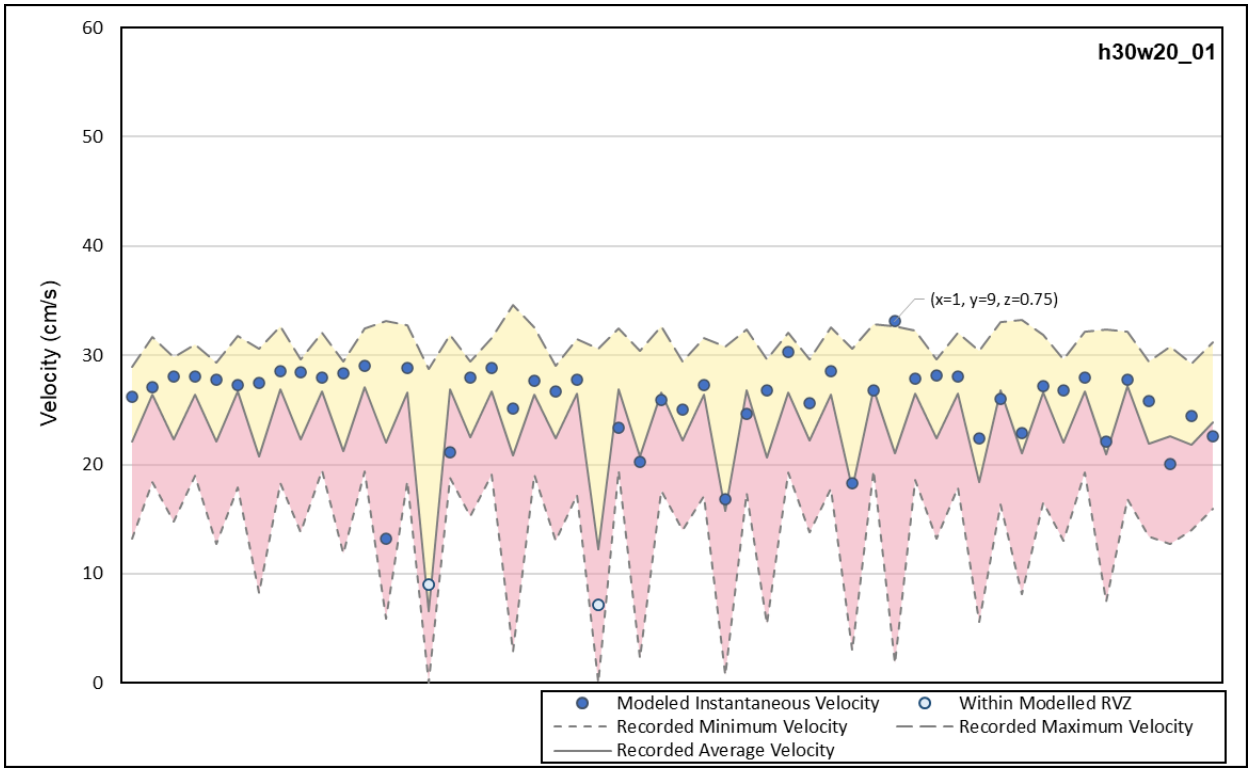

Figure 8.4 : Validation of simulation H30W20_01; the different reading is within the modelled shear layer of the wake

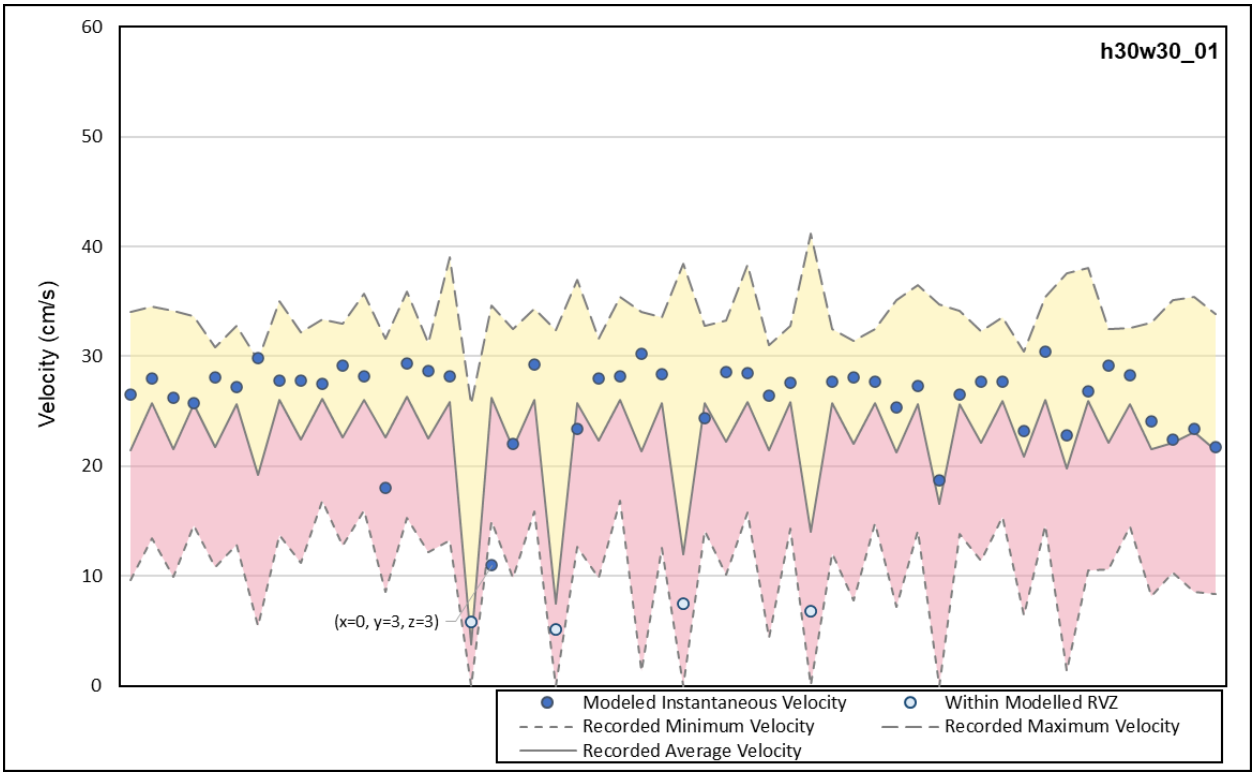

Figure 8.5 : Validation of simulation H30W30_01; the different reading is within the modelled wake

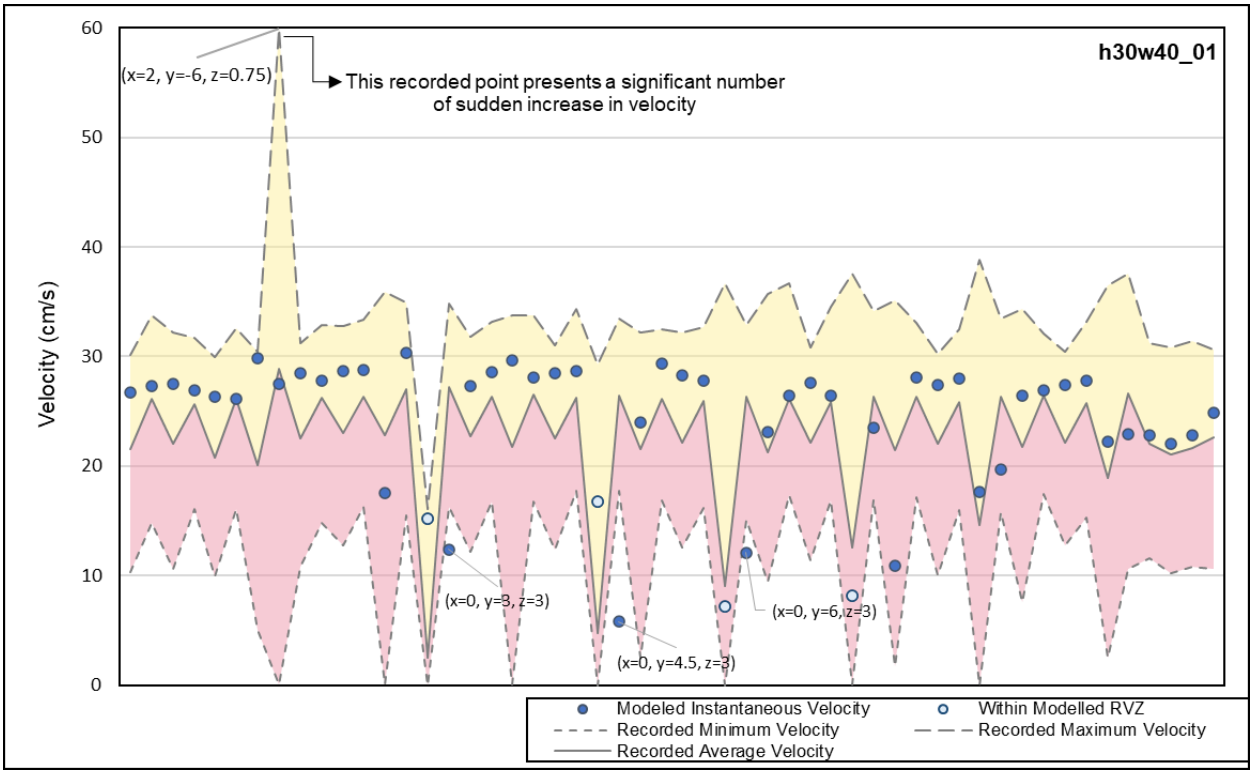

Figure 8.6 : Validation of simulation H30W40_01; the different readings are within the modelled wake

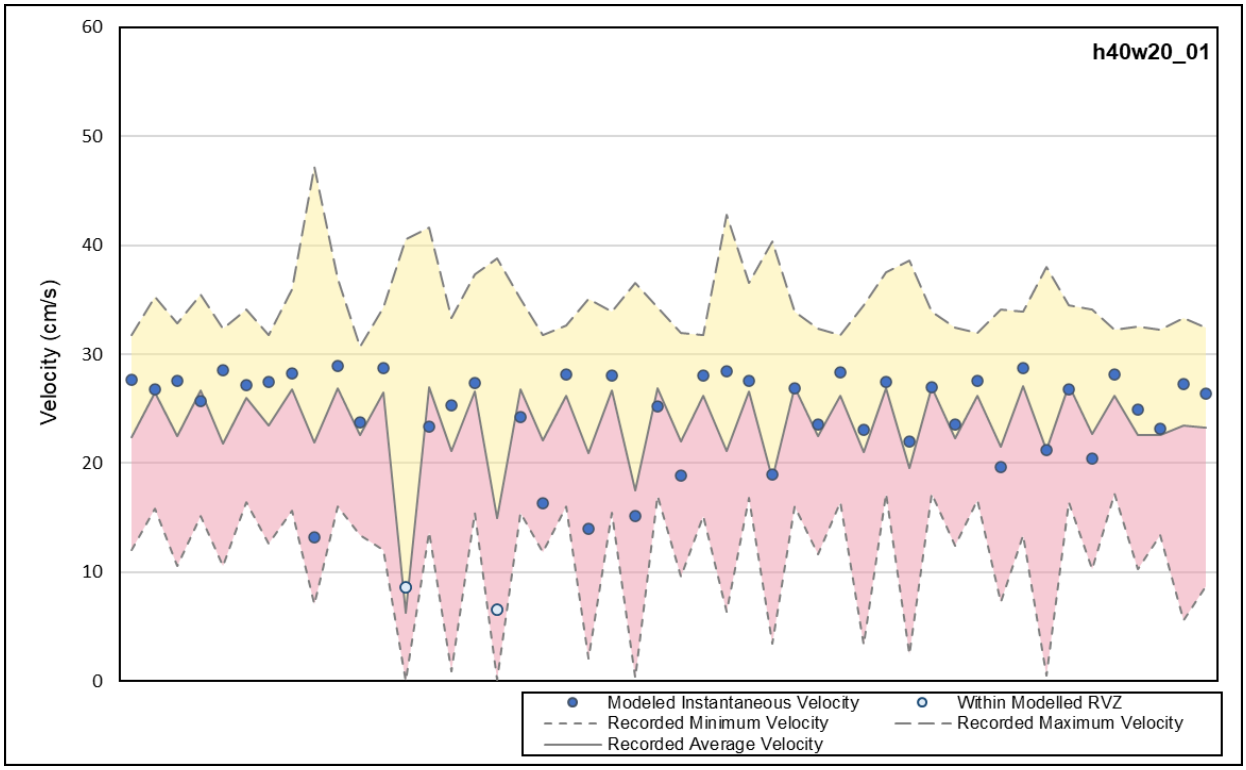

Figure 8.7 : Validation of simulation H40W20_01

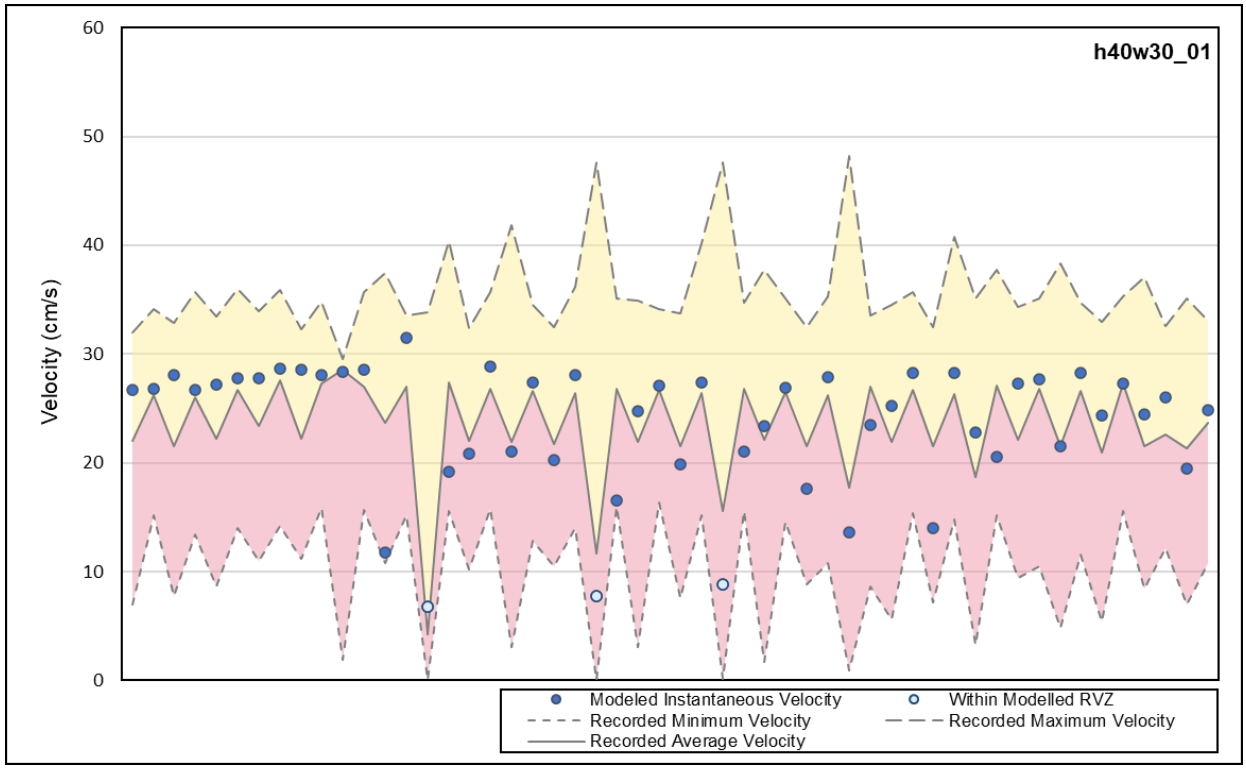

Figure 8.8 : Validation of simulation H40W30_01

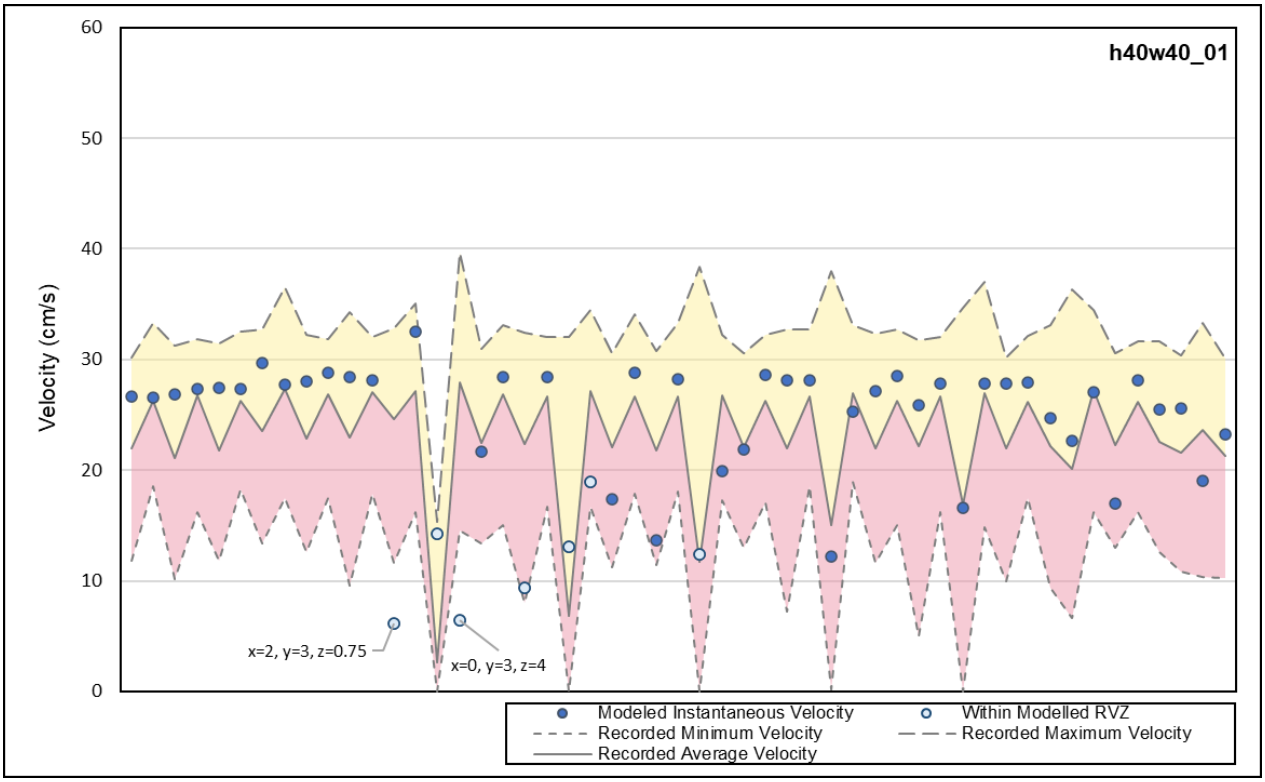

Figure 8.9 : Validation of simulation H40W40_01; the different readings are within the modelled RVZ

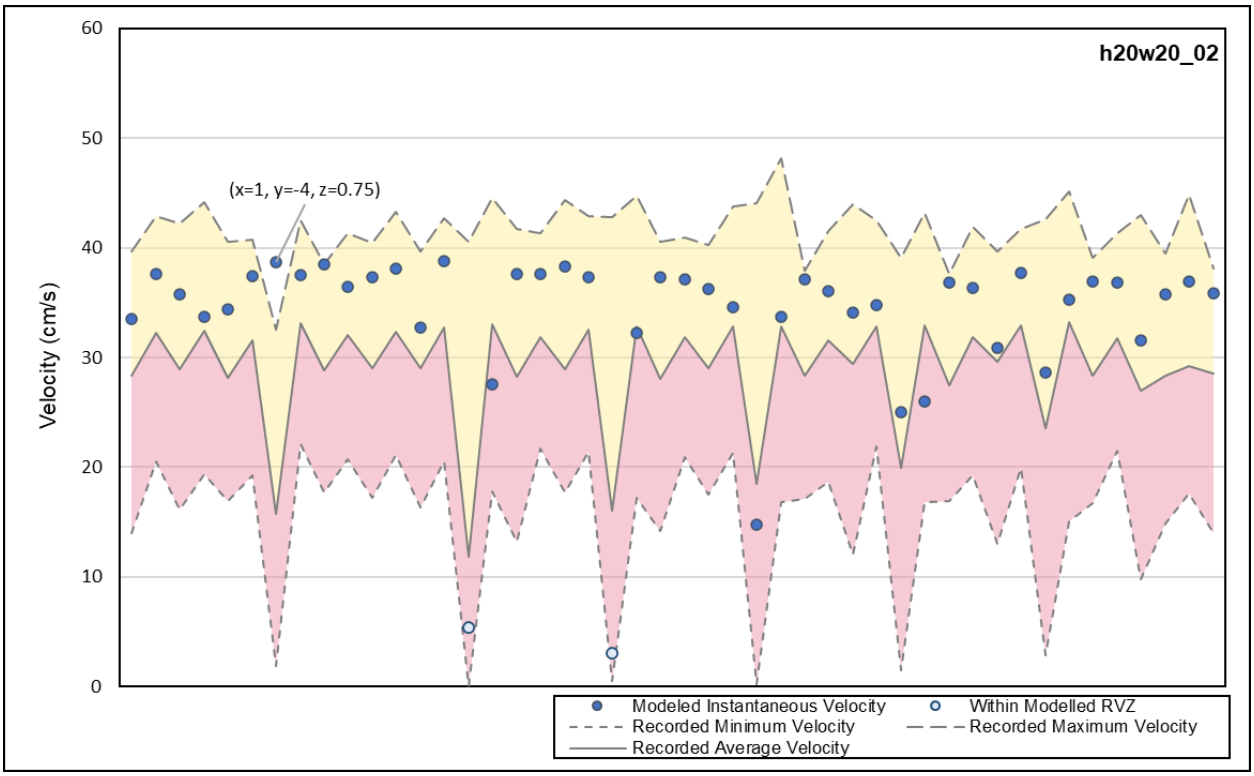

Figure 8.10 : Validation of simulation H20W20_02; the difference is observed just upstream of the spoiler baffle and is attributed to the possible inexact placement of the ADV

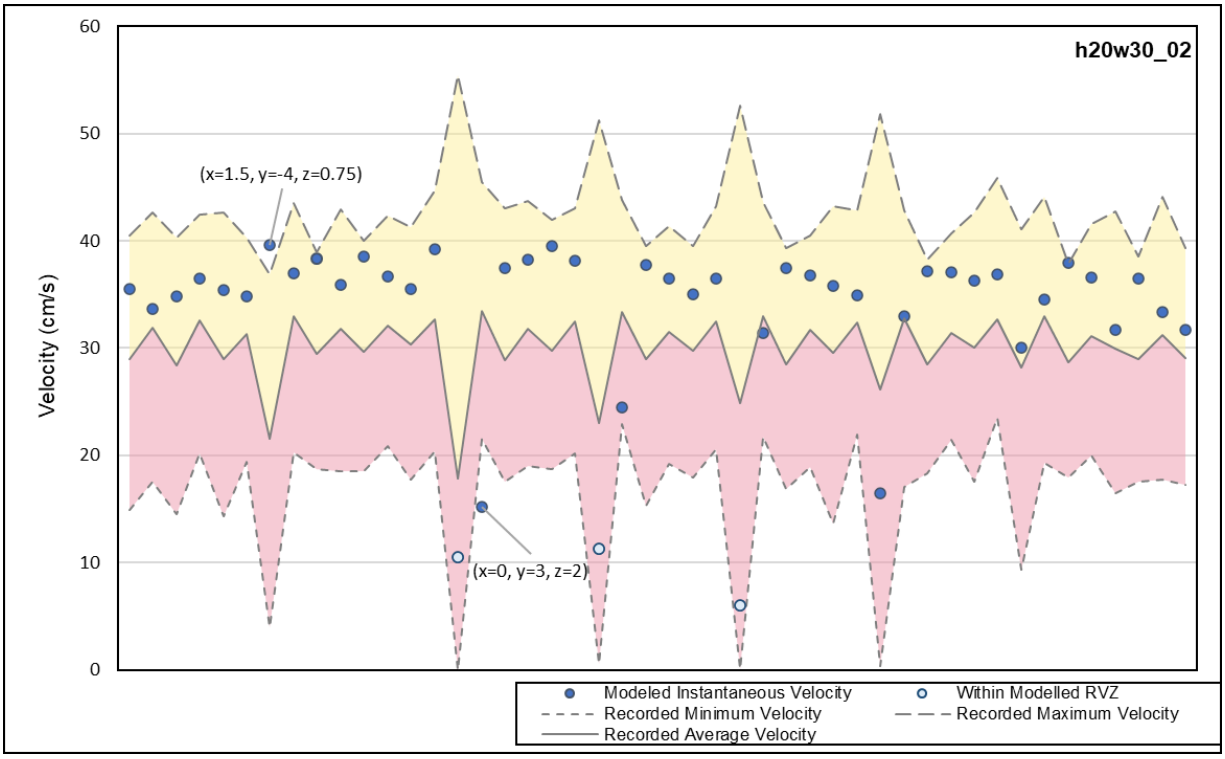

Figure 8.11 : Validation of simulation H20W30_02; the difference observed just upstream of the spoiler baffle is attributed to the possible inexact placement of the ADV, the other difference is within the modelled wake

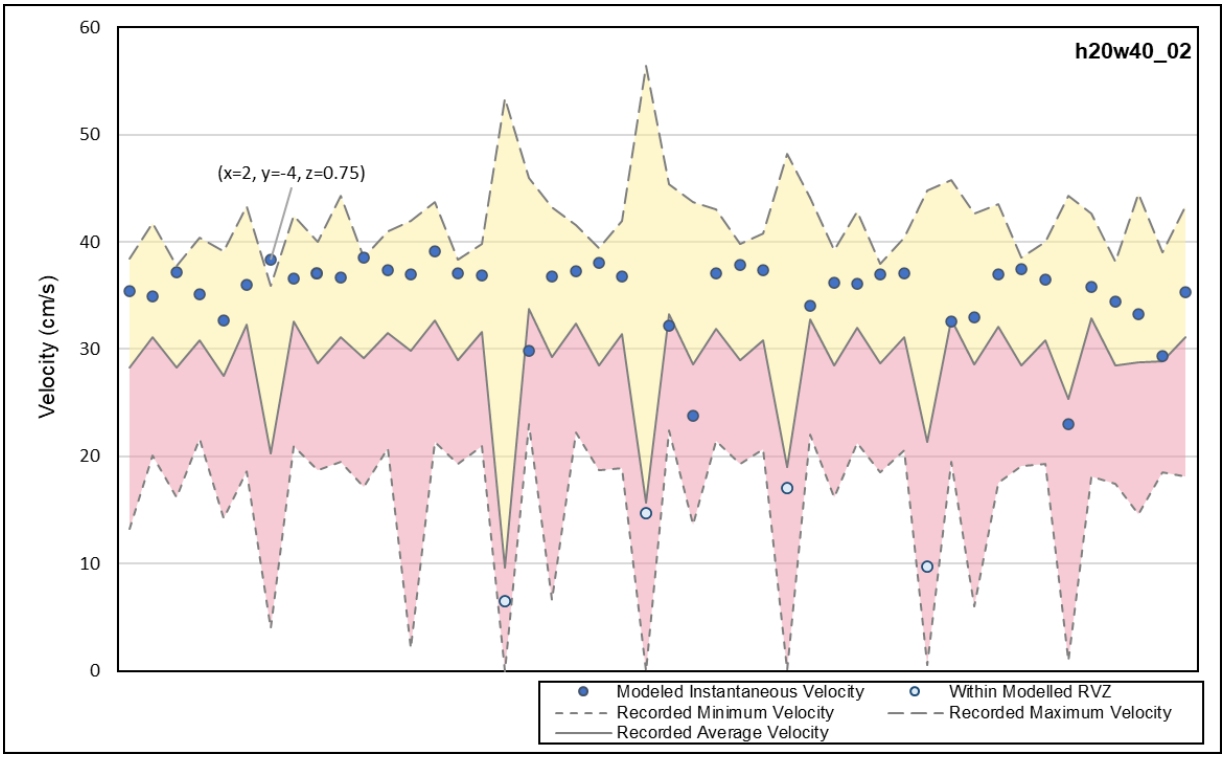

Figure 8.12 : Validation of simulation H20W40_02; the difference observed just upstream of the spoiler baffle is attributed to the possible inexact placement of the ADV

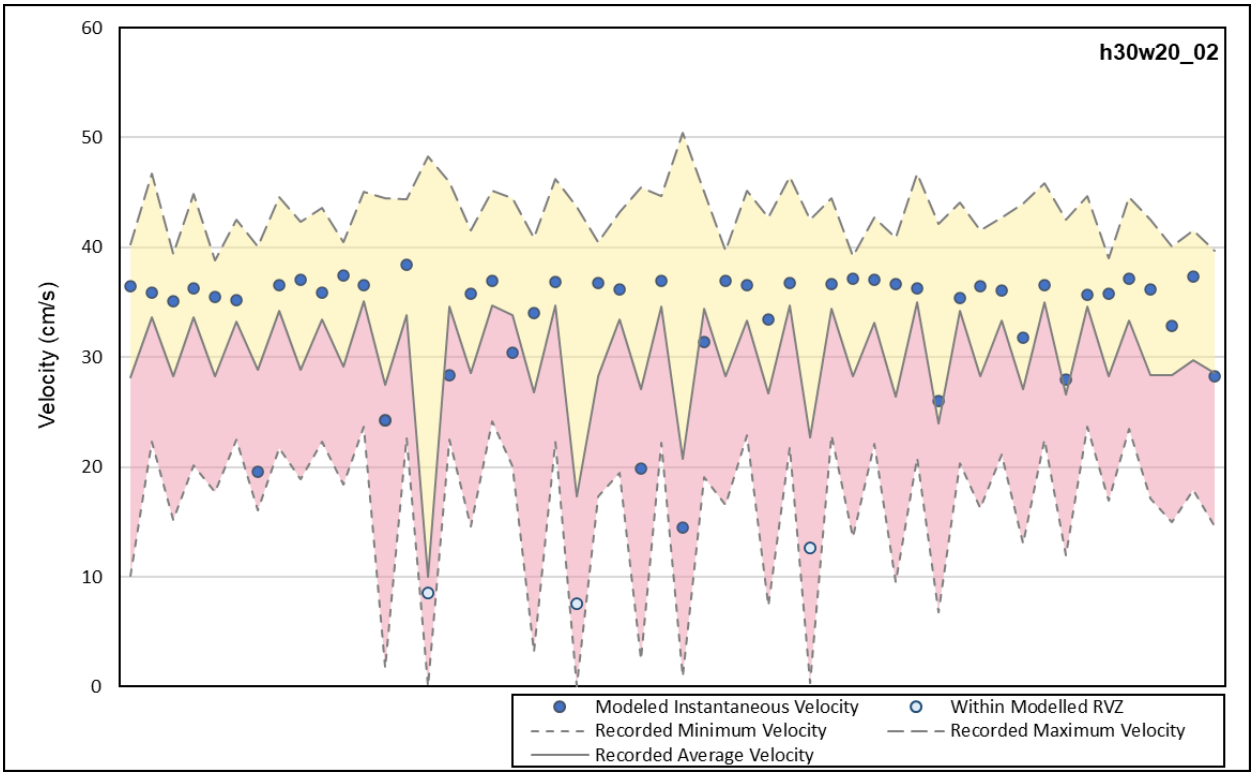

Figure 8.13 : Validation of simulation H30W20_02

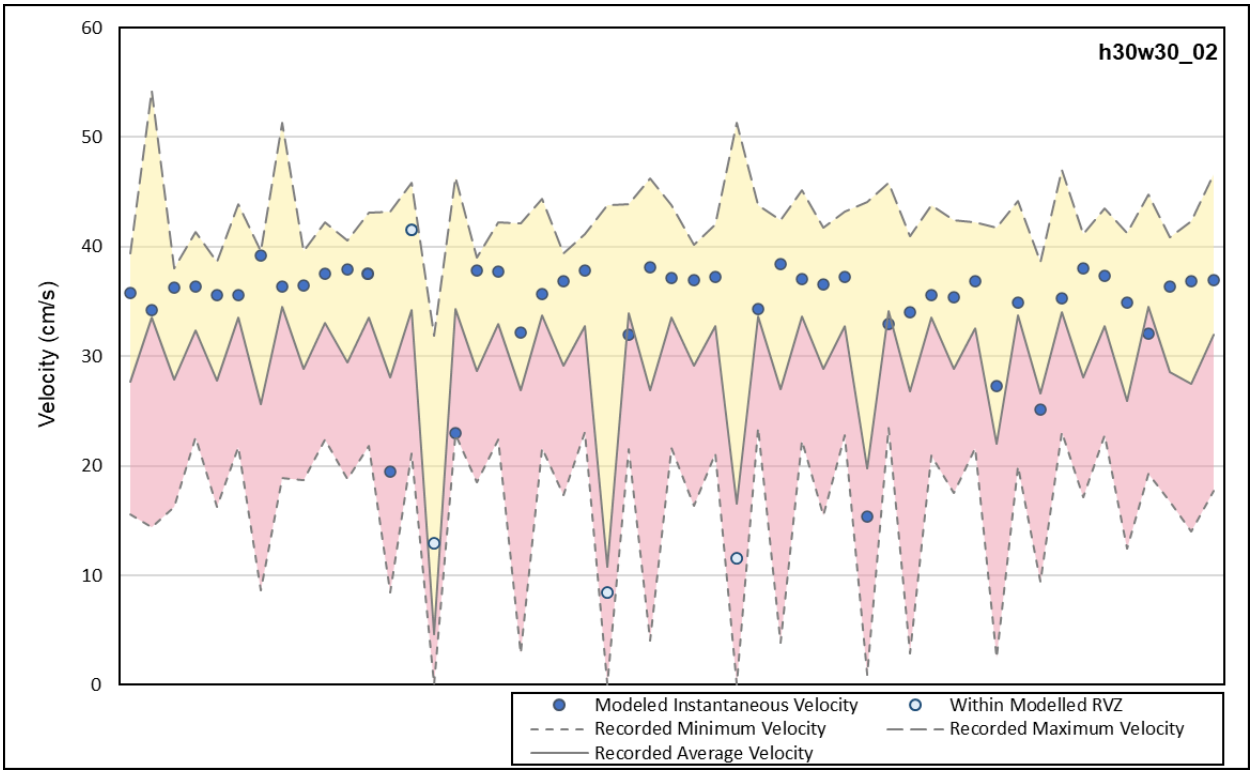

Figure 8.14 : Validation of simulation H30W30_02

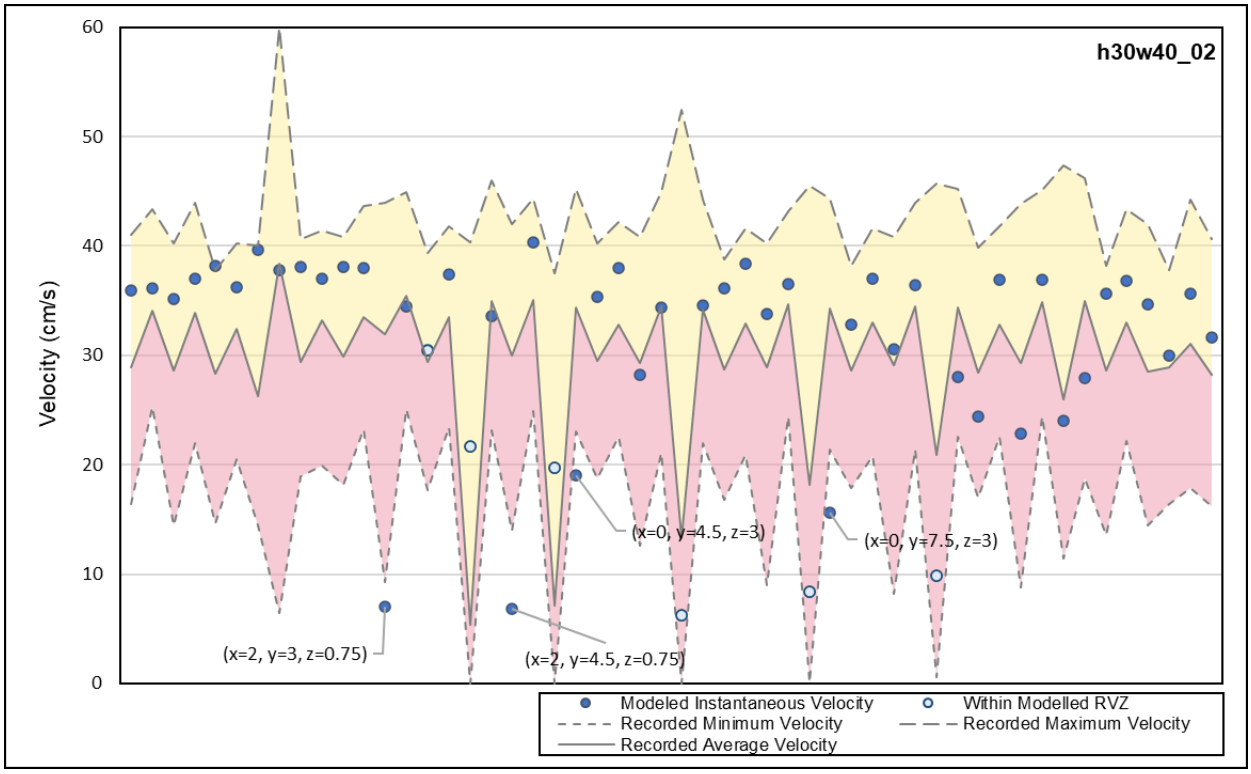

Figure 8.15 : Validation of simulation H30W40_02; the different readings are within the modelled wake

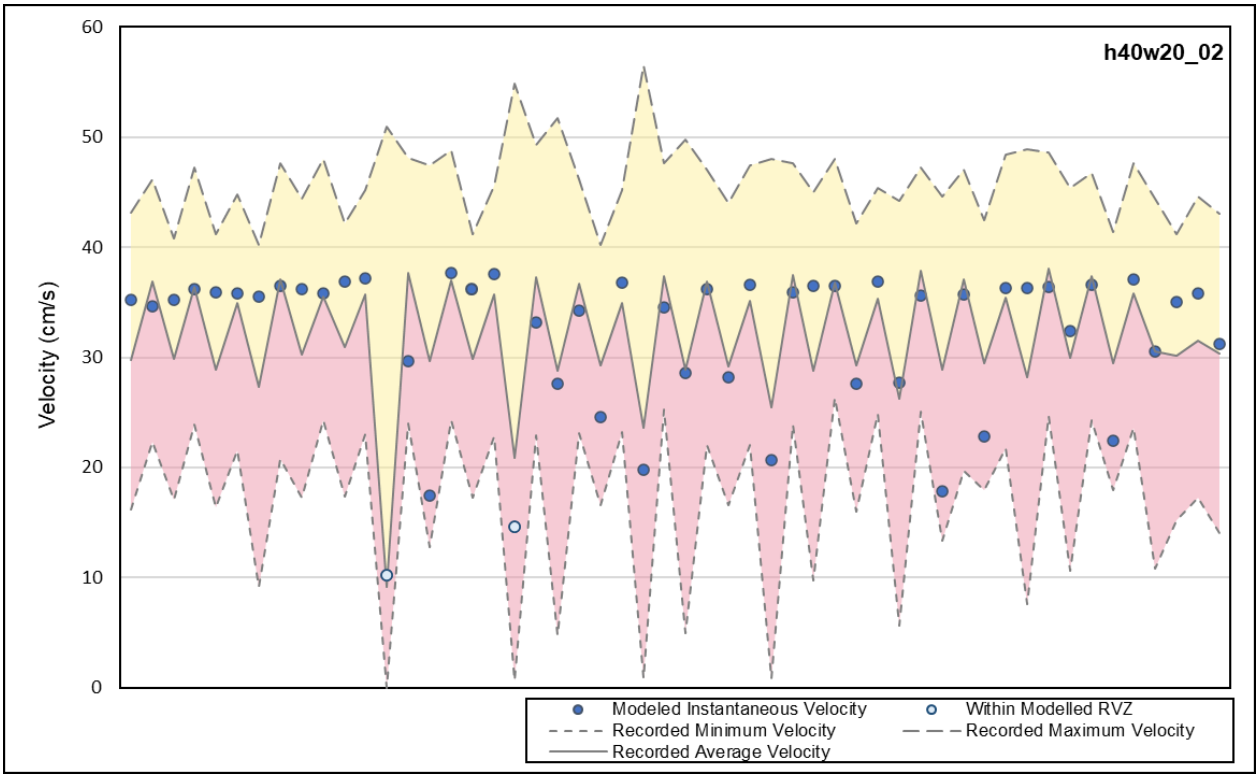

Figure 8.16 : Validation of simulation H40W20_02

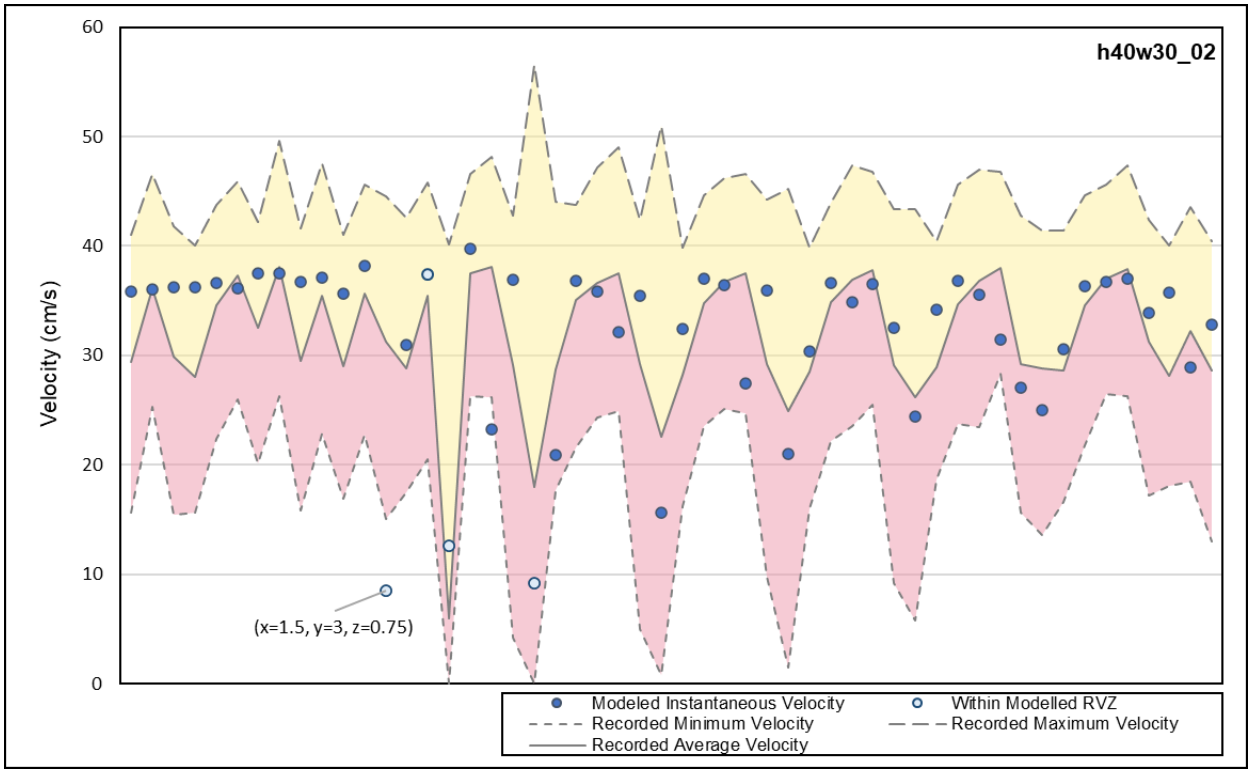

Figure 8.17 : Validation of simulation H40W30_02; the different data is within the modelled RVZ

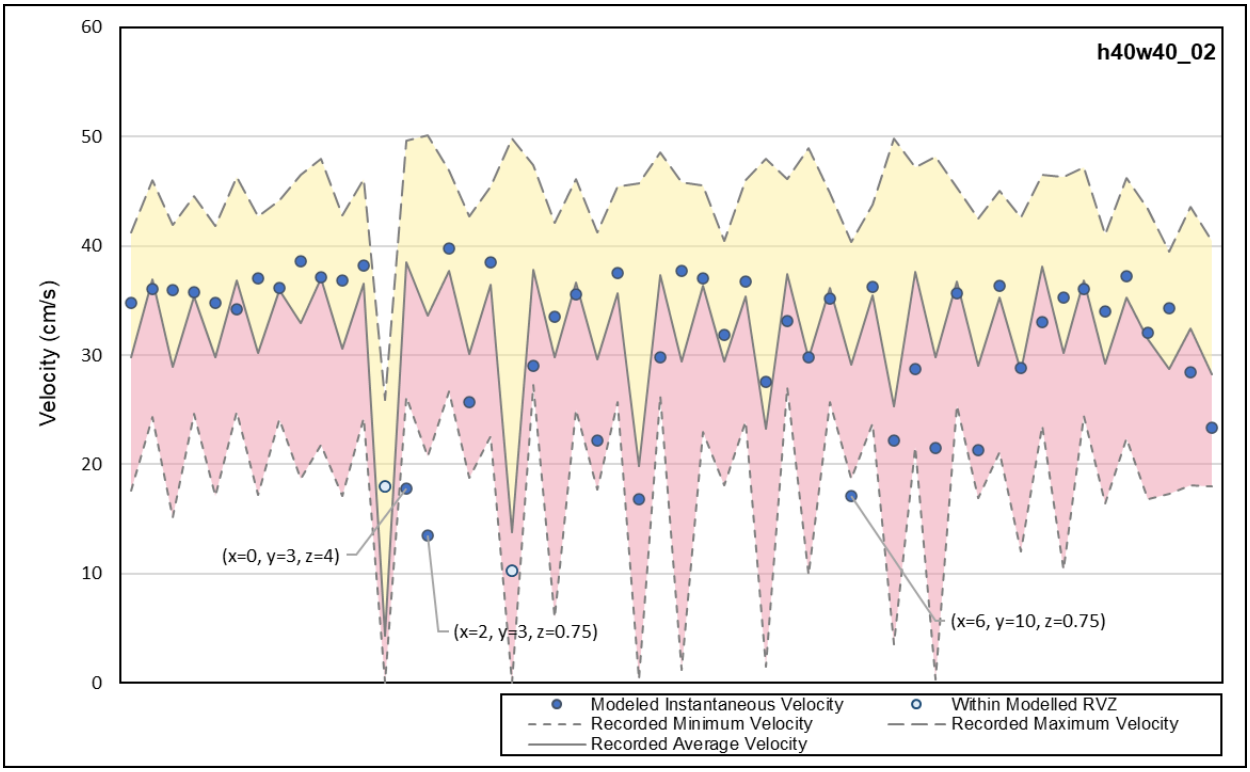

Figure 8.18 : Validation of simulation H40W40_02; different data is within the modelled wake

9 APPENDIX II

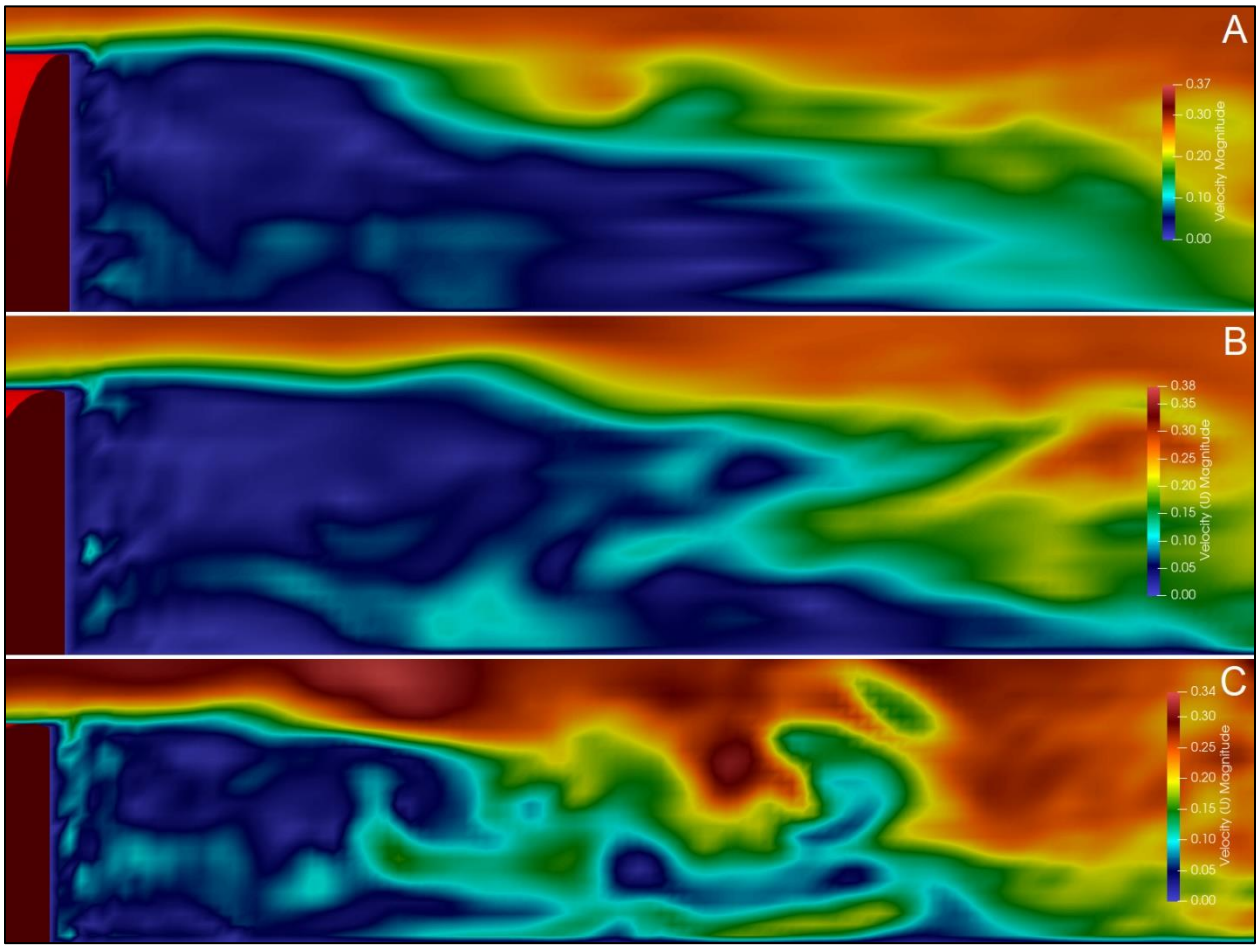

Figure 9.1 : Side view of RVZ (x = 0) generated for (A) h20w20_01 | Low level of fragmentation; (B) h20w30_01 | Low level of fragmentation; and (C) h20w40_01 | Moderate level of fragmentation

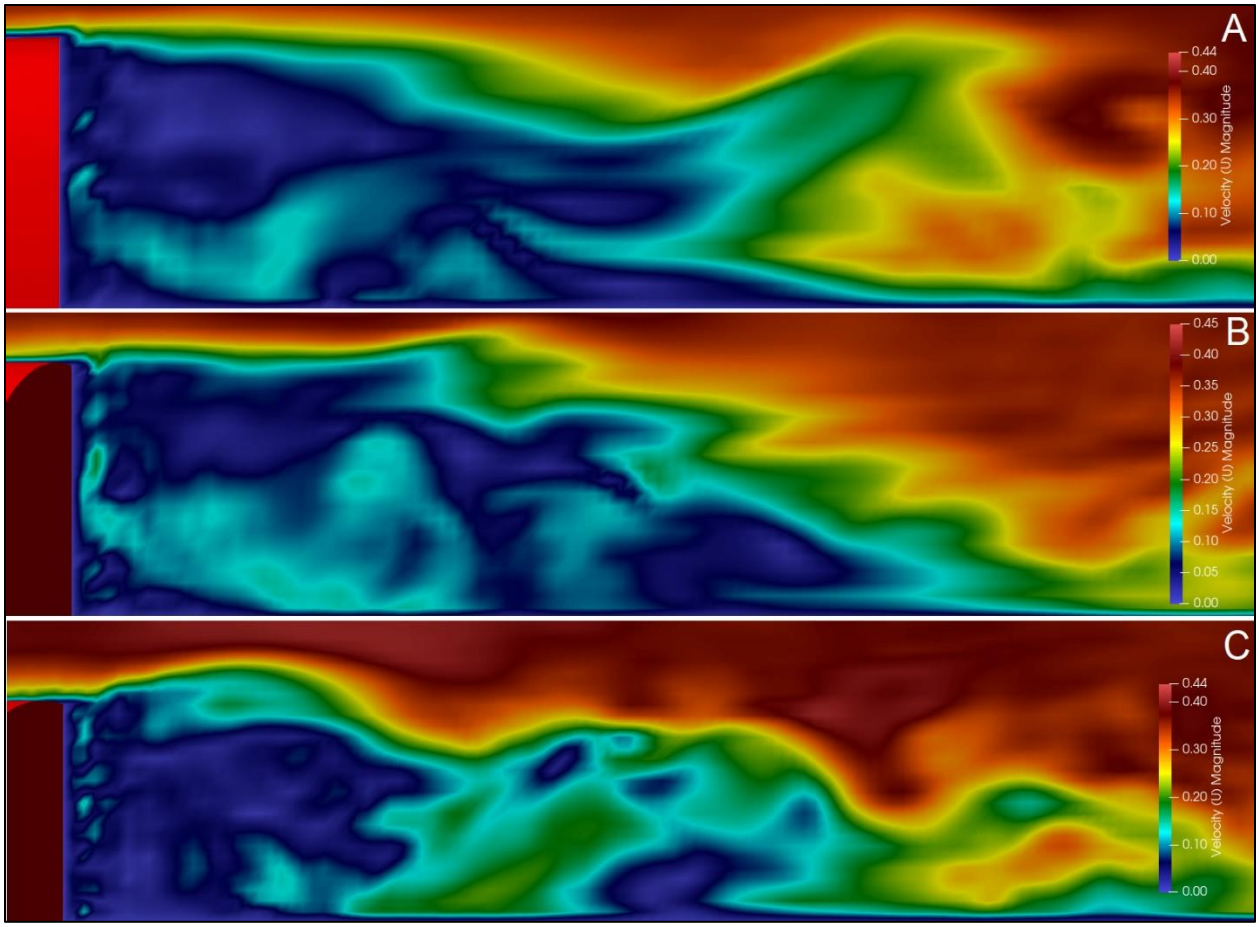

Figure 9.2 : Side view of RVZ (x = 0) generated for (A) h20w20_02 | Low level of fragmentation; (B) h20w30_02 | Moderate level of fragmentation; and (C) h20w40_02 | Moderate level of fragmentation

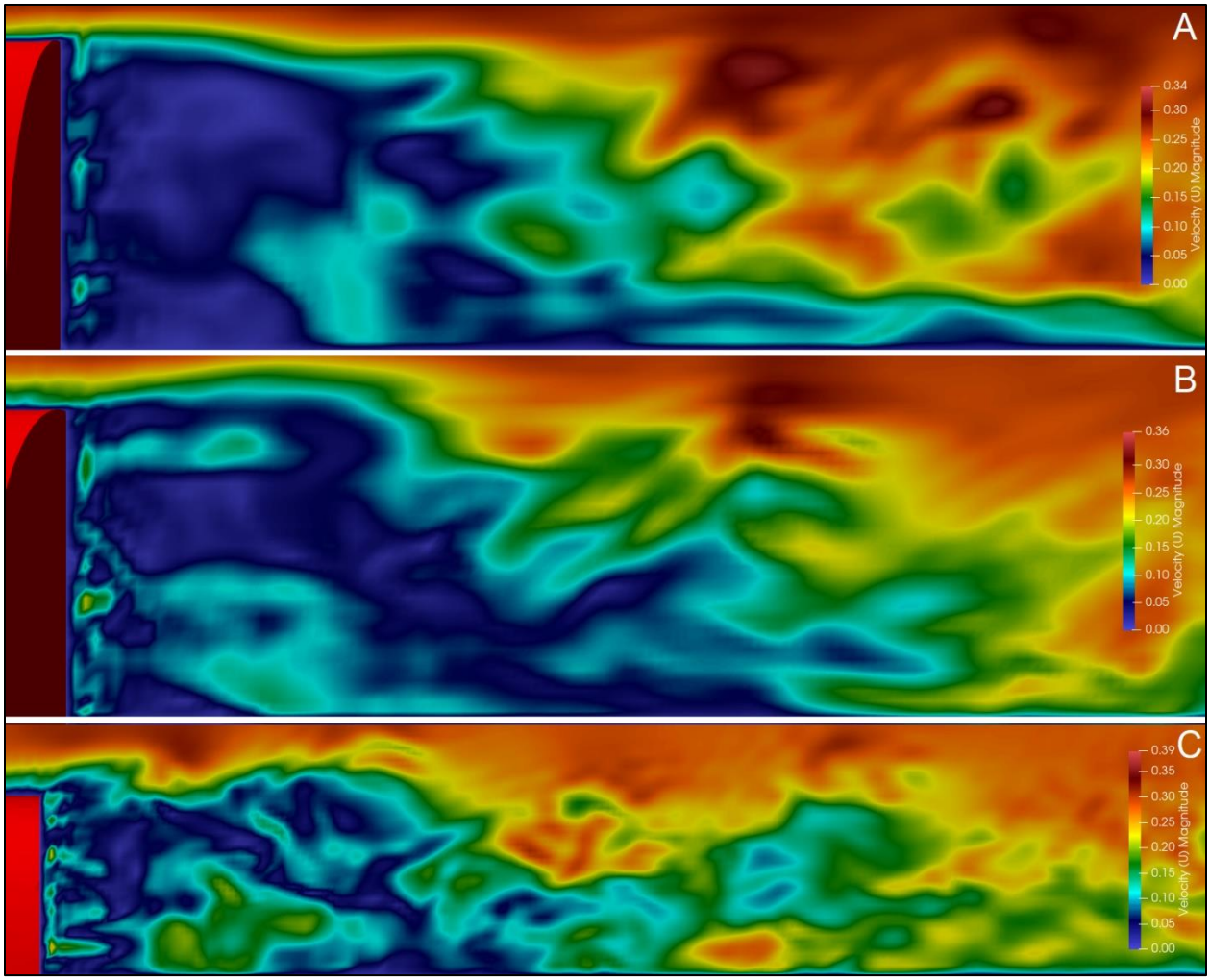

Figure 9.3 : Side view of RVZ (x = 0) generated for (A) h30w20_01 | Moderate level of fragmentation; (B) h30w30_01 | Moderate level of fragmentation; and (C) h30w40_01 | High level of fragmentation

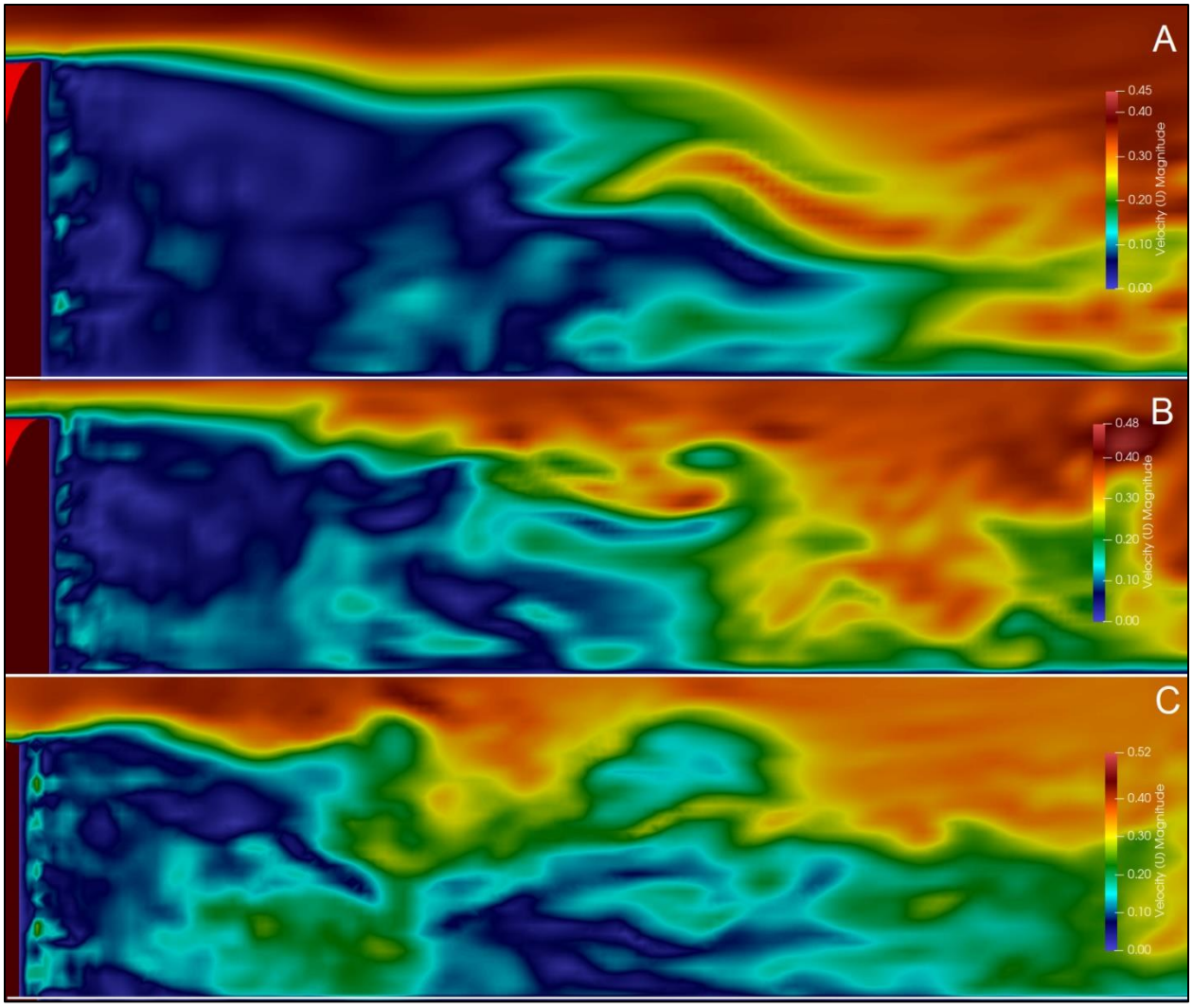

Figure 9.4 : Side view of RVZ (x = 0) generated for (A) h30w20_02 | Low level of fragmentation; (B) h30w30_02 | Moderate level of fragmentation; and (C) h30w40_02 | High level of fragmentation

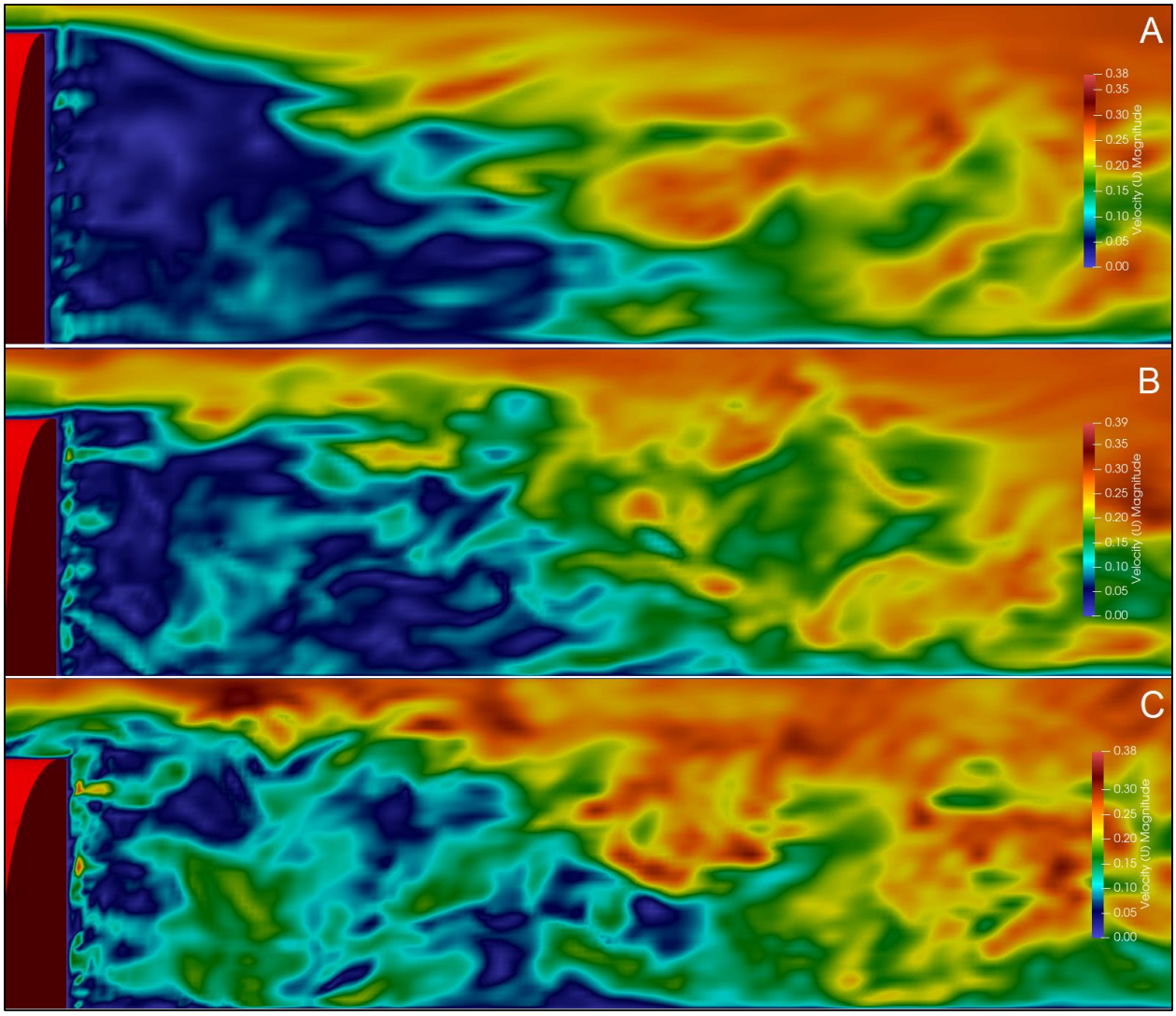

Figure 9.5 : Side view of RVZ (x = 0) generated for (A) h40w20_01 | Low level of fragmentation; (B) h40w30_01 | Moderate level of fragmentation; and (C) h40w40_01 | High level of fragmentation

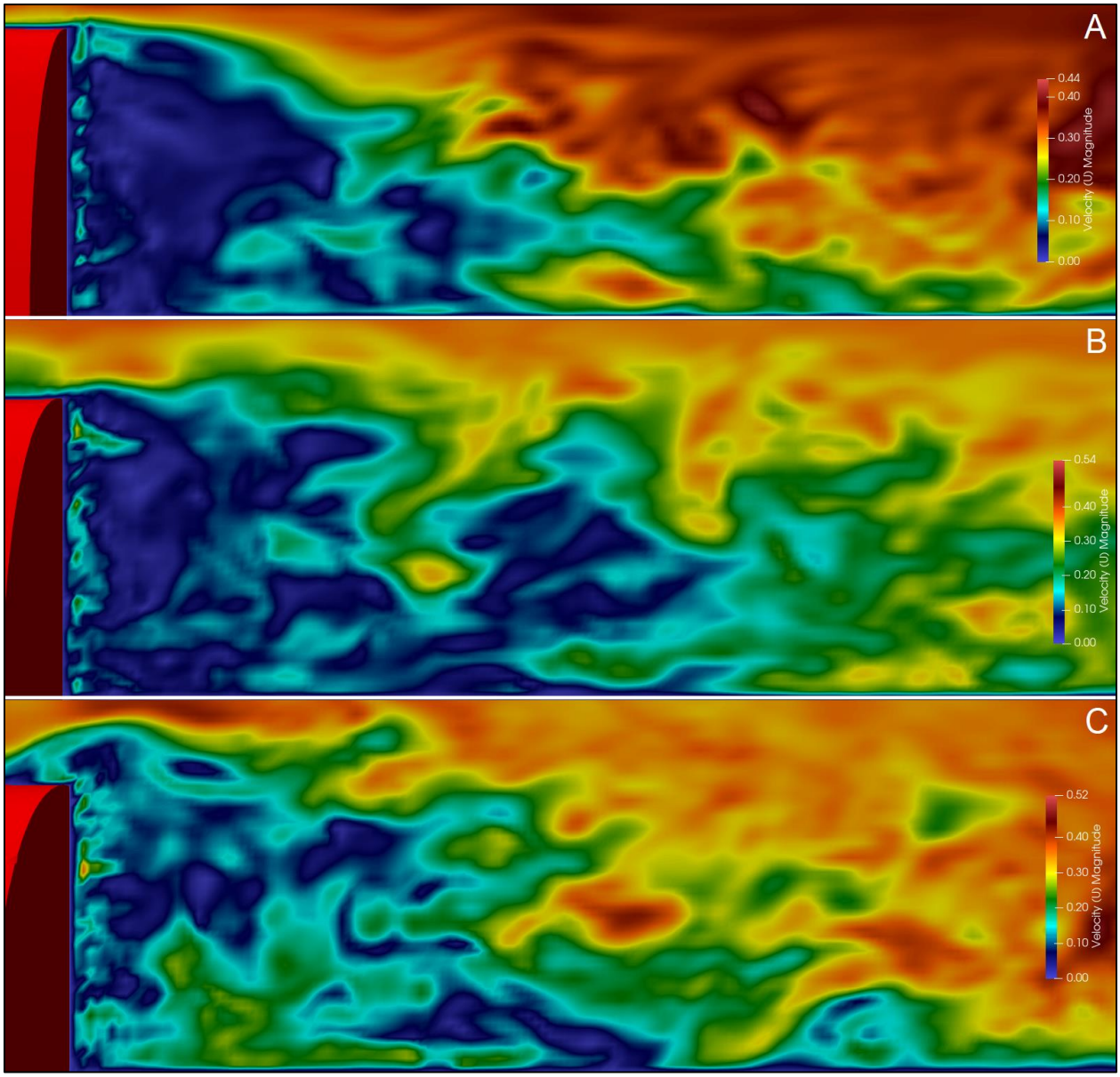

Figure 9.6 : Side view of RVZ (x = 0) generated for (A) h40w20_02 | Moderate level of fragmentation; (B) h40w30_02 | Moderate level of fragmentation; and (C) h40w40_02 | High level of fragmentation